Hydrologic Modeling using Triangulated Irregular Networks: Terrain Representation, Flood Forecasting and Catchment Response

by

Enrique R. Vivoni

S.B. Environmental Engineering Science
M.S. Civil and Environmental Engineering
Massachusetts Institute of Technology, 1996, 1998

Submitted to the Department of Civil and Environmental Engineering
in Partial Fulfillment of the Requirements for the Degree of

DOCTOR OF PHILOSOPHY IN HYDROLOGY
AT THE
MASSACHUSETTS INSTITUTE OF TECHNOLOGY
SEPTEMBER 2003

Signature of Author .....
Department of Civil and Environmental Engineering
June 23, 2003

Certified by .....
Dara Entekhabi
Professor of Civil and Environmental Engineering

Certified by .....
Rafael L. Bras
Professor of Civil and Environmental Engineering

Accepted by .....
Oral Buyukozturk
Chairman, Departmental Committee on Graduate Students

Hydrologic Modeling using Triangulated Irregular Networks: Terrain Representation, Flood Forecasting and Catchment Response

by

Enrique R. Vivoni

Submitted to the Department of Civil and Environmental Engineering
on June 23rd, 2003, in partial fulfillment of the requirements for the degree of
Doctor of Philosophy in Hydrology.

Abstract

Numerical models are modern tools for capturing the spatial and temporal variability in the land-surface hydrologic response to rainfall and understanding the physical relations between internal watershed processes and observed streamflow. This thesis presents the development and application of a distributed hydrologic model distinguished by its representation of topography through a triangulated irregular network (TIN) and its coupling of the surface and subsurface processes leading to the catchment response. As a research tool for hydrologic forecasting and experimentation, the TIN-based Real-time Integrated Basin Simulator (tRIBS) fully incorporates spatial heterogeneities in basin topography, surface descriptors and hydrometeorological forcing to produce dynamic maps of hydrologic states and fluxes. These capabilities allow investigation of theoretical questions and practical problems in hydrologic science and water resources engineering.

Three related themes are developed in this thesis. First, a set of methods are developed for constructing TIN topographic models from raster digital elevation models (DEM) for hydrologic and geomorphic applications. A new approach for representing a steady-state estimate of a particular watershed process within the physical mesh is introduced. Hydrologic comparisons utilizing different terrain models are made to investigate the suitable level of detail required for capturing process dynamics accurately. Second, the TIN-based model is utilized in conjunction with a rainfall forecasting algorithm to assess the space-time flood predictability. For two hydrometeorological case studies, the forecast skill is assessed as a function of rainfall forecast lead time, catchment scale and the spatial variability in the quantitative precipitation forecasts (QPF). Third, the surface and subsurface runoff response in a complex basin is investigated with respect to changes in storm properties and the initial water table position. The partitioning of rainfall into runoff production mechanisms is found to be a causative factor in the nonlinearity and scale-dependence observed in the basin hydrograph response.

The model applications presented in this thesis highlight the advantages of TIN-based modeling for hydrologic forecasting and process-oriented studies over complex terrain. In particular, the multi-resolution and multi-scale capabilities are encouraging for a range of applied and scientific problems in catchment hydrology.

Thesis Supervisors: Dara Entekhabi and Rafael L. Bras
Titles: Professors of Civil and Environmental Engineering

Acknowledgement

I would like to acknowledge the financial support from the National Science Foundation Graduate Fellowship and Ford Foundation Dissertation Fellowship for completion of this thesis. Much of this research was undertaken in fulfillment of a joint MIT-AER project sponsored by the US Army Research Office and an MIT-National Weather Service collaborative agreement. This financial support is greatly appreciated.

Many thanks are due to the members of my thesis committee, Dr. Earle Williams, Dr. Ross Hoffman, Dr. Rafael Bras and Dr. Dara Entekhabi. Both Rafael and Dara have provided guidance, advice and support in the development of this research. In addition, all have become dear friends and mentors. I also wish to thank the many colleagues at MIT, past and present, which have contributed to this thesis. In particular, Valeri Ivanov, Matt Van Horne and Christopher Grassotti have been key collaborators in this effort.

Finally, I must acknowledge the unwavering support from my family in Puerto Rico and my wife, Amapola, who has been my constant companion in this journey.

Table of Contents

List of Figures

List of Tables

Introduction

Rainfall-runoff prediction is one of the fundamental scientific and engineering challenges faced in hydrology. Despite empirical, analytical and numerical modeling studies, the conversion of a highly-variable rainfall field into a spatially-distributed runoff response remains an unanswered, open question. This is primarily due to the fact that the hydrologic processes operating in a watershed are highly heterogeneous, interconnected, depend on the moisture state in the system and exhibit strong nonlinearities and hysteresis. Basin characteristics, such as soils, geology, vegetation and topography, vary in space and time leading to differences in runoff response. In order to realistically capture the rainfall-runoff transformation, the variability in hydrologic processes and the controls exerted by basin descriptors must be accounted for in numerical models.

Many approaches currently exist to model the hydrologic processes occurring in real-world catchments. Traditionally, conceptual and spatially-lumped models have been utilized to represent landscape complexity and basin hydrologic response through a cascade of reservoirs with varying characteristic storages and time scales. In the last two decades, the use of physically-based, distributed hydrologic models has received considerable attention by the scientific community. A distributed model attempts to represent basin variability in landscape properties, rainfall and hydrologic states and fluxes. An effort is made to describe the time-evolution of soil moisture and runoff within a catchment, in addition to traditional metrics such as the basin discharge. The potential of distributed models to improve the predictability and understanding of hydrologic systems is largely due to the increasing availability of remote sensing data products describing the spatial characteristics of the catchment surface.

This research is focused on the development and application of a distributed hydrologic model distinguished by its representation of topography through a triangulated irregular network (TIN) and its coupling of the surface and subsurface processes leading to the catchment response. The TIN-based Real-time Integrated Basin Simulator (tRIBS) model is a research tool for hydrologic forecasting and experimentation. Over the TIN terrain, the model uses rainfall and meteorological forcing to predict the distributed basin response, including infiltration, runoff, evapotranspiration, soil moisture and shallow aquifer flow, occurring in the hillslope system. Runoff is generated via four mechanisms, infiltration-excess runoff, saturation-excess runoff, perched return flow and groundwater exfiltration, and routed via overland and channel pathways. Evaporation from bare soil, vegetation and rain interception are calculated via a surface radiation and energy balance.

As a tool for hydrologic experimentation, the tRIBS model offers the opportunity to understand the control of catchment characteristics on hydrologic response. In particular, the model offers insight into the interrelationship between coupled hydrologic processes occurring within a basin and the observed discharge hydrograph. In this thesis we address several inter-related scientific questions using the distributed model. Three general themes are developed in the following:

(1) Topographic representation in distributed hydrology models.

(2) Coupled rainfall and flood predictability in multiple catchments.

(3) Surface-subsurface runoff response nonlinearity and scale dependence.

These themes represent open topics in catchment hydrology and hydrometeorology that are critical to understanding how rainfall is ultimately transformed into runoff. These challenging topics are examined in this thesis through the lens of the distributed model.

The representation of topography in hydrology has been frequently addressed in the context of raster-grid models. With the availability of high resolution terrain data (e.g., 25-m globally), the computational burden of large data sets limits distributed model applications. As a result, new representations of basin topography, such as triangulated irregular networks (TIN), need to be utilized in distributed modeling. Very few studies have developed consistent methods for capturing topographic and hydrologic variability for real-world catchments using TINs. With the development and application of the TIN-based hydrology model, methods for deriving a TIN terrain representation were required. As a result, a significant focus of this thesis is the development of topographic models using TINs. Chapter 1 introduces a set of sequential methods for constructing multiple resolution TIN models using either topographic slope or hydrologic criteria. Comparisons to raster-DEMs are used to show that TINs retain terrain attributes with significantly smaller number of model nodes, while preserving the basin area, depicting streams accurately and conserving terrain ruggedness. In addition, a new method for constraining a triangulation with an estimate of the steady-state hydrologic response is introduced.

Chapter 2 introduces the Channel-Hillslope Integrated Landscape Development (CHILD) and the TIN-based Real-time Integrated Basin Simulator (tRIBS) models that are utilized in the subsequent chapters. The computational data structure and hydrologic model physics of the TIN-based distributed hydrologic model are the primary focus. A brief description of the relevant hydrologic processes necessary for the model application studies is provided with references made to the primary works describing the model.

Chapter 3 extends the concept of coupling a physical triangulation with a measure of hydrologic variability to three related applications, saturation-excess runoff, transport-

limited sediment erosion and rainfall-triggered shallow landsliding. The development of TIN meshes that resemble the steady state indices of hydrogeomorphic behavior provides a physically-based initialization for distributed models. Comparison between traditional and the index-based triangulations in the context of transient distributed simulations show that the terrain initialization affects model response. In particular, increased resolution in regions contributing to runoff improves the simulation of the variable source area.

In Chapter 4, a detailed analysis is conducted on the effect of terrain resolution on the distributed hydrologic response. While this topic has been addressed with grid-based models, the effect of TIN resolution on basin processes has received little attention. The hydrologic performance of the tRIBS model is directly related to the TIN resolution. The sensitivity of basin-averaged and distributed hydrologic metrics (water balance, runoff, surface saturation, groundwater dynamics) are determined by the aggregation properties of terrain attributes. The insight gained from the spatial sensitivity test is useful for the multi-scale calibration of the tRIBS model in flood forecasting applications.

The second theme in this thesis concerns the predictability of flood events using combined radar nowcasting and distributed flood forecasting. Chapter 5 presents a series of methods for utilizing radar-based short-term rainfall predictions to force the spatially-distributed tRIBS model. Through comparisons to discharge observations at multiple gauging stations, flood predictability is assessed as a function of forecast lead time, basin scale, and spatial rainfall variability in a simulated real-time operation. Comparisons to rainfall persistence demonstrate the advantages of utilizing radar forecasting for flood forecasting applications. The analysis illustrates the sensitivity of the distributed model to

uncertainties in the future rainfall and characterizes the transformation of rainfall to runoff errors with respect to changes in the ratio of catchment size to basin response time.

In Chapter 6, the response of the distributed hydrologic model is investigated in detail with respect to the variability in rainfall forcing and initial wetness conditions. This constitutes the third theme in this thesis concerned with the nonlinearity and basin scale-dependence in the rainfall-runoff transformation. The control of runoff mechanisms on the production of surface and subsurface flow is shown to impart a signature on the nonlinearity in the runoff response at multiple catchment scales. The position of the water table and the storm characteristics, such as rainfall intensity and duration, play key roles in determining flood response. An analysis of the spatial organization of runoff also shows that multiple runoff types occur simultaneously from specific basin locations and that catchment scale determines the predominance of a particular mechanism.

In summary, this thesis seeks to capture the spatial and temporal variability in the rainfall-runoff transformation through a numerical model that combines surface and subsurface processes and explicitly represents catchment and rainfall heterogeneities. The development of the model and its application for terrain representation, flood forecasting and catchment response studies are presented. As a tool for hydrologic experimentation and forecasting, the TIN-based Real-time Integrated Basin Simulator opens new avenues to answering scientific questions concerning a basin's response to rainfall. This thesis contributes to the existing knowledge base by advancing how topographic and hydrologic processes can be represented in distributed models, how rainfall and hydrologic modeling can be combined for multi-scale flood forecasting and how runoff nonlinearity and scale-dependence are related to the coupled surface-subsurface hydrologic processes.

Chapter 1:

Generation of Triangulated Irregular Networks based on Hydrological Similarity

1.1 Introduction

A representation of land-surface topography is required in most earth system models, including general circulation models (GCM), numerical weather prediction models (NWP), land-surface models (LSM), and distributed hydrologic models (DHM). Terrain representation differs among these models since the coupling between model processes and landforms varies considerably. In general, as the model scale increases, the resolution and accuracy in the terrain decrease. For climate, hydrology and weather models operating at large spatial scales (*e.g.*, $O(10^3 - 10^6\ km^2)$), inaccurate representation of terrain and its spatial variability is recognized as an important source of model error (*e.g.*, Wood *et al.*, 1997; Koster *et al.*, 2000; Warrach *et al.*, 2002).

Traditionally, terrain data in hydrologic models has been represented in two ways: (1) aggregating grid-based digital elevation models (DEMs) or (2) introducing a topographic distribution function. Both methods attempt to account for the spatial variability in topography without adding computational burden into large-scale models. Neither approach, however, can incorporate the full information content of high-resolution topographic data available from land surveying, aerial photogrammetry (Gesch *et al.*, 2002) or synthetic aperture radar (Farr and Kobrick, 2000). As a result, hydrologic models typically have terrain inaccuracies that propagate directly to model predictions (*e.g.*, Vieux, 1991; Zhang and Montgomery, 1994; Walker and Willgoose, 1999). A

computationally efficient method for representing high-resolution terrain with minimal information loss is currently lacking in the context of large-scale hydrologic models.

Climate, weather and hydrology models typically incorporate terrain data through the use of raster-grids. The aggregation of high-resolution data, however, can result in information loss and distortion of terrain properties. An alternative approach is utilizing multiple-resolution meshes developed based on criteria that conserve relevant physiographic features. For example, triangulated irregular networks (TINs) are efficient means for constructing DEMs from elevation measurements. To date however, the application of TIN terrains in hydrology has not explicitly considered the preservation of key hydrologic features. This chapter presents a geographic information system (GIS) approach for deriving *hydrologically-significant* TINs. The approach takes into consideration watershed characteristics, while reducing the number of elements as compared to raster-DEMs. A new method for embedding the steady-state hydrologic response into a TIN model is also presented. By constraining the TIN with a topographic distribution function, a terrain model whose resolution reflects a measure of hydrological similarity is developed. A quantitative comparison of TIN and grid models for a set of basins demonstrate the advantages of the multiple-resolution approach.

The approach proposed in this chapter is the use of a multiple-resolution, triangulated irregular network as a representation of terrain. A *hydrologically-significant* TIN terrain model is constructed by taking into account the topographic, hydrographic and hydrologic features characterizing a catchment. Sampling dense DEMs based on either topographic or hydrologic variability results in an adaptive mesh resolution. In addition, the triangulation explicitly represents stream networks, basin boundaries,

riparian or floodplain zones and landscape features. By incorporating hydrologic features into terrain models of large watersheds, the spatial representation is closely tied to the underlying hydrologic processes (Liang and Mackay, 2000).

In this chapter, we present a geographical information system (GIS) methodology for constructing TIN terrains for a range of basin scales. Three sequential approaches are described: (1) *traditional* TINs; (2) *hydrographic* TINs and (3) *hydrological similarity* TINs. Traditional TINs are based exclusively on topography, while hydrographic and hydrological similarity TINs integrate additional criteria. Each approach builds on the previous method and can be tailored to a specific site based on the relevant hydrologic processes. The result is a computationally feasible terrain model that preserves topographic information. Comparisons between TIN and raster-DEM models using an equivalent number of nodes demonstrate the utility of the methodology.

1.2. Triangulated Irregular Networks

Topography can be represented using a number of computational structures, including contour lines, regular grids or triangulated irregular networks. The TIN data structure is a piece-wise linear interpolation of a set of points in x, y, z coordinates, resulting in non-overlapping triangular elements of varying size. Although several methods exist, the Delaunay triangulation is a preferred technique since it provides a nearly unique and optimal triangulation (*e.g.*, Watson and Philip, 1984; Tsai, 1993). For a set of points, the Delaunay criterion ensures that a circle passing through three points on any triangle contains no additional points. The *constrained* Delaunay triangulation permits the inclusion of linear features directly into a terrain model (Tsai, 1993). Using Delaunay triangulation, DEMs can be sampled to construct efficient terrain models.

Various factors motivate the use of triangular elements to represent watershed topography. The primary advantage is the variable resolution offered by the irregular domain (Kumler, 1994), as opposed to the single resolution in raster grids. Regions of high terrain variability can be modeled more precisely as compared to areas of low relief variance. Multiple resolutions translate to computational savings as the number of nodes is reduced in areas of low terrain variability (Goodrich *et al.*, 1991). A second advantage is that TINs permit linear features to be preserved in the model mesh. This allows the terrain to mimic natural terrain breaklines, stream networks or boundaries between heterogeneous regions without introducing the raster artifacts inherent in grid methods.

Despite these advantages, few studies have addressed methods for constructing TIN terrains in hydrologic models. Efforts have focused primarily on watershed delineation using TINs (*e.g.*, Palacios-Vélez and Cuevas-Renaud, 1986; Jones *et al.*, 1990; Nelson *et al.*, 1994) and TIN-based distributed modeling (*e.g.*, Goodrich *et al.*, 1991; Palacios-Vélez and Cuevas-Renaud, 1992; Tucker *et al.*, 2001b). Discussions on how to generate TIN terrains prior to watershed modeling have been largely bypassed, in particular when dealing with real-world basins. Notable exceptions include the works of Tachikawa *et al.* (1994) and Nelson *et al.* (1999). In most applications, however, TIN terrain modeling remains an ad-hoc process based on sampling DEMs at a desired data reduction rate without explicitly considering hydrologic features.

The generation of TIN terrain models is facilitated with a geographic information system that allows manipulation of elevation data in a variety of formats (*e.g.*, points, vectors, grids). Arc/Info GIS, for example, has a set of TIN routines that are popular for three-dimensional surface analysis (ESRI, 1992). Methods for constrained Delaunay

triangulation permit the generation of TIN surfaces while incorporating linear features. In this chapter, we use Arc/Info to develop TINs that preserve key hydrologic characteristics while minimizing the number of computational nodes. Here, we focus on methods for selecting elevation points and incorporating hydrologic information into a TIN model.

1.3. Methodology

The methods for constructing TINs presented here account for topography, hydrography and the hydrologic basin response parameterized by a topographic index. The principal objective is to capture the salient hydrologic features efficiently since feasibility is sought for large-scale applications. A schematic of the methods is presented in Figure 1.1. In the following, we illustrate TIN terrain models that are progressively constrained by additional criteria derived from the raster-DEM.

1.3.1 Topographic approach: Traditional TINs

Topography exercises a major control on the hydrologic response in watersheds (Wood *et al.*, 1990). With the availability of raster-DEMs, the direct use of topographic data in hydrologic models is often sought. For large-scale models, however, utilizing high-resolution grids requires a means for data reduction to obtain reasonable computational performance. For raster-DEMs, data reduction is usually achieved through pixel aggregation at the expense of topographic detail (Vieux, 1991). In *traditional* TIN models, essential topographic information is captured by selectively sampling a DEM. Criteria for selecting elevation points vary widely among different surface simplification algorithms (see Heckbert and Garland, 1997).

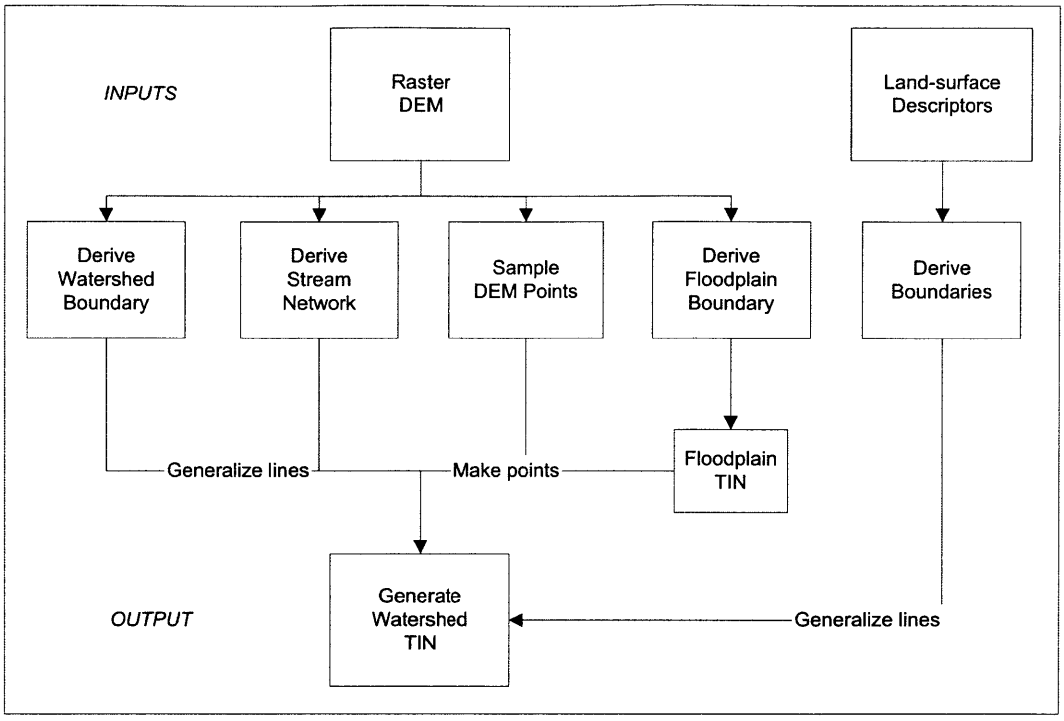

Figure 1.1 Schematic of TIN generation process. Methods for sampling DEM points includes: (1) topographic criteria (VIP or Latticetin) or (2) wetness index. Constrained Delaunay triangulation used to generate the watershed TIN using sampled DEM points, linear features and ancillary land surface descriptors.

Various GIS methods exist for selecting critical elevations from dense DEMs. Lee (1991) compares two approaches implemented in Arc/Info, the very important point (VIP) and the drop heuristic (DH) methods. VIP is a *local* procedure based on determining the "significance" of a point relative to a 3x3 filter. The significance measure is the distance between the actual elevation and the interpolations from its four transects. A percentage (v) of the significant points is retained for triangulation. DH is a *global* procedure guaranteeing that a TIN is within an elevation tolerance (z_r). The approach successively removes DEM points, retaining significant points that result in a TIN surface exceeding the tolerance. A variant on the DH method is implemented in Arc/Info as Latticetin (Lee, 1991; ESRI, 1992).

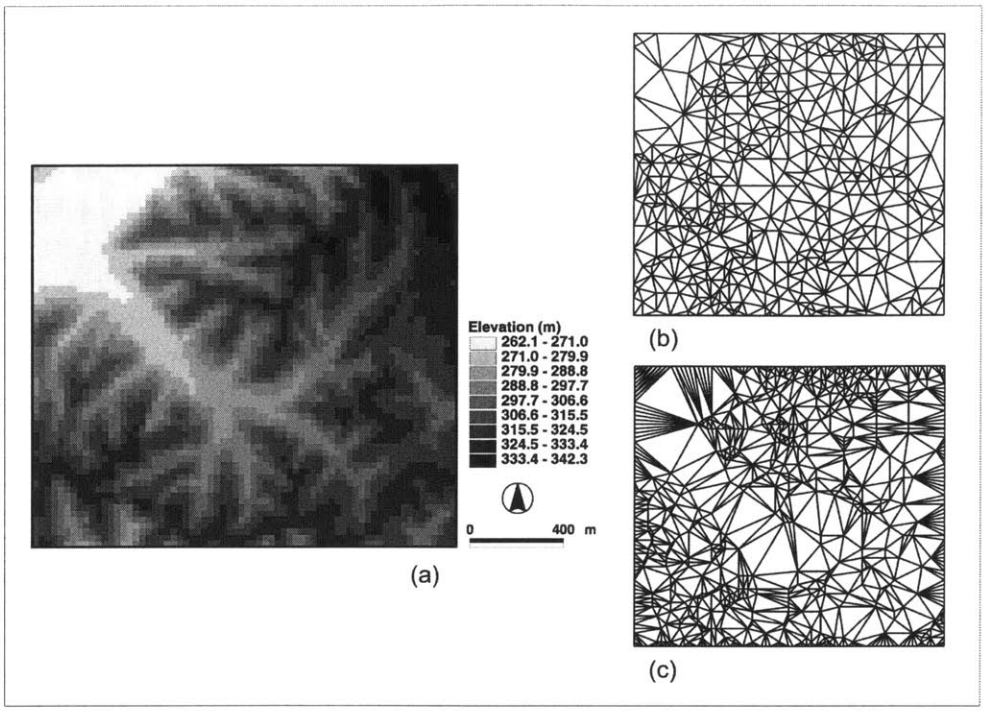

Figure 1.2. Traditional TINs utilizing topographic sampling methods for a given data reduction factor (d = 0.1). (a) USGS 30-m DEM within Peacheater Creek basin, OK (4416 cells); (b) TIN generated using Latticetin method (z_r = 8 m); (c) TIN generated using VIP method (v = 16%).

Lee (1991) evaluated the performance of the two methods, concluding that the DH approach exhibited lower root mean square errors (RMSE) over a range of resolutions. Preliminary parameter tests are usually required to select values of v or z_r given a desired data reduction factor (d). In this chapter, we define d as the number of TIN nodes (n_t) divided by the number of DEM cells (n_g). Figure 1.2 compares the VIP and Latticetin TINs for d = 0.1. By linearly interpolating each TIN onto a regular grid, we compute an RMSE value of 7.22 meters (VIP) and 3.01 meters (Latticetin), relative to the DEM. The RMSE difference between the methods is significant with only the LatticeTIN producing acceptable results. Thus, the accuracy and resolution of traditional TINs

depend on the method and parameters chosen to select DEM points. For this reason, we only consider the Latticetin method for selecting nodes using a topographic criterion.

1.3.2 Incorporating hydrographic and landscape features: Hydrographic TINs

Traditional TIN methods generally do not account for criteria other than conserving critical slopes. As a result, traditional techniques ignore hydrographic and landscape features that are desirable in hydrologic models. The strategy (Figure 1.1) for formulating *hydrographic* TINs combines topographic DEM sampling with stream networks, basin boundaries and floodplains in a constrained Delaunay triangulation.

1.3.2.1 Channel network and watershed boundary

Channel networks can be delineated from topographic data using standard algorithms (O'Callaghan and Mark, 1984; Jenson and Domingue, 1988). In this chapter, a constant-threshold method is used to classify DEM points as stream cells (Figure 1.3a). An iterative procedure ensures that the drainage density of the extracted network is equivalent to available hydrographic data. The stream network is preserved in the hydrographic TIN model by conforming the triangulation to natural breaklines (Tachikawa *et al.*, 1994; Nelson *et al.*, 1999). Curve simplification is typically required to remove raster effects in the network. Nevertheless, the resulting streams are statistically equivalent to the original hydrography (Douglas and Peucker, 1973).

Incorporating basin boundaries permits hydrographic TINs to accurately capture the watershed area (Figure 1.3a). Watershed delineation is based on creating a depressionless DEM, deriving the flow direction along the steepest path and computing the upslope area (O'Callaghan and Mark, 1984; Jenson and Domingue, 1988). As in the

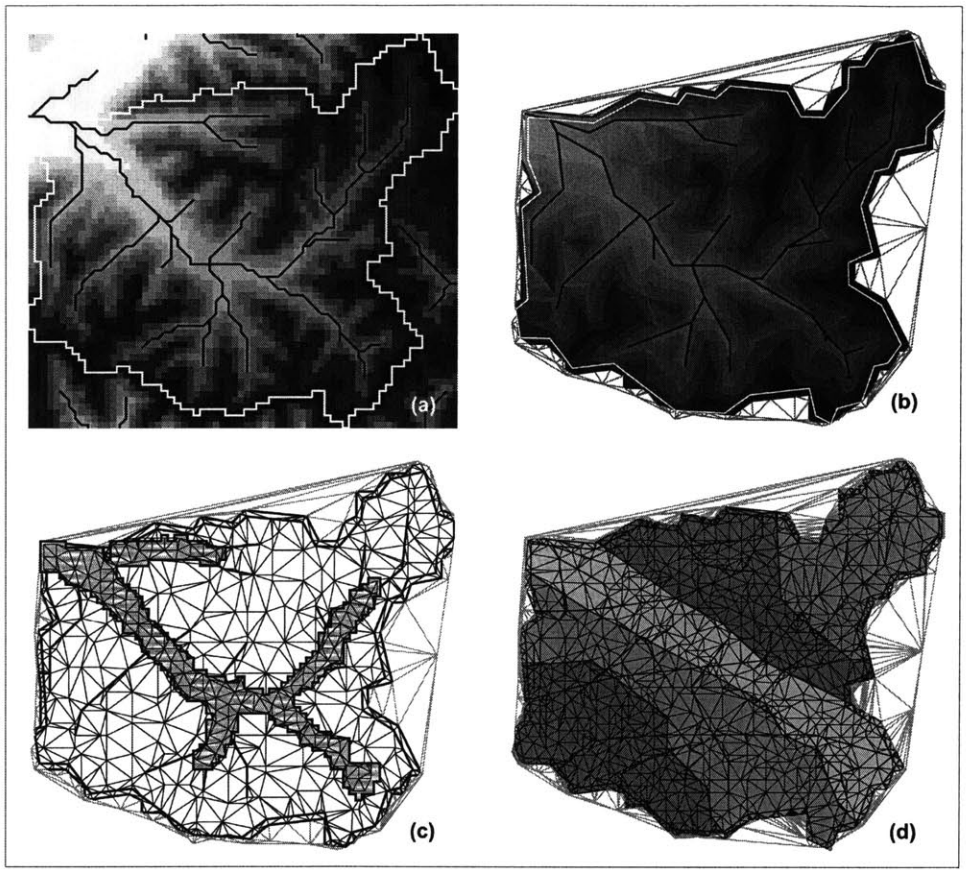

Figure 1.3. Hydrographic TINs. (a) Basin and channel network using threshold (50 pixels); (b) Hillshade view of the TIN model (z_r = 8 m) conforming to the stream network (black line) and buffered catchment boundary (outer lines); (c) Facet view of the floodplain boundary (gray region) and nested floodplain TIN; (d) Facet view of the TIN model conforming to hydrologic response units (shaded regions).

stream network, simplification of the rasterized watershed boundary is required. In addition, buffering the boundary with an inner ring of interpolated elevations is used to maximize the captured basin area. This overcomes problems arising when the TIN model is represented as its dual Voronoi diagram. Figure 1.3b illustrates the stream network and basin boundary incorporated into the hydrographic TIN model.

1.3.2.2 Floodplains and riparian zones

Terrain models may need to resolve floodplains or riparian zones found along high-order stream reaches. Recent work has concentrated on methods for incorporating survey measurements into TIN models (Tate *et al.*, 2002). If available, a detailed river-floodplain model can be integrated within a courser terrain model. Under many circumstances, however, the availability of surveyed cross sections is limited. For these cases, floodplain delineation from raster-DEMs provides a simple method for determining floodplain extent. In this chapter, an elevation-threshold algorithm is used to extract the floodplain boundary (Williams *et al.,* 2000). The floodplain DEM is then sampled to create a *nested* triangulation that conforms to the hydrographic TIN model (Figure 1.3c). High-resolution floodplain representation is a key hydrographic feature in convergent valley bottoms that saturate frequently and produce runoff.

1.3.2.3 Landscape features

Triangulated networks models can also resolve regional landscape features such as vegetation and soil units used in hydrologic models to parameterize land-surface processes. Landscape descriptors, typically available as polygon features, can be directly incorporated into a TIN terrain model ensuring that surface properties do not vary at the sub-element scale (Figure 1.3d). In addition, combinations of land-surface descriptors are used to represent areas of similar hydrologic response (*e.g.*, Kouwen *et al.*, 1993). Hydrologic response units (HRUs) can be included in the TIN model, ensuring the triangulation conforms to the unit boundaries. Alternatively, HRUs can be used to constrain the triangulation by varying the TIN resolution for each unit. Although feasible, this approach lacks a quantifiable hydrologic measure and requires ancillary surface data.

1.3.3 Embedding steady-state hydrologic response: Hydrological similarity TINs

Catchment form has long been recognized as a primary control on surface and subsurface flow. Topographic data is frequently used to characterize the steady-state hydrologic response through a topographic or wetness index (Beven and Kirkby, 1979; O'Loughlin, 1986). Topographic distribution functions serve as an index of local hydrologic similarity, aggregating DEM pixels of similar hydrologic behavior into a few, distinct classes. For example, the Topmodel framework provides a quantifiable hydrological similarity measure for saturation excess runoff, typically represented as:

$$\lambda_i = \ln\left(a_i / \tan\beta_i\right) \tag{1.1}$$

where λ_i is the topographic index at the ith pixel, a_i is the pixel contributing area per unit width and $\tan\beta_i$ is the local pixel slope. The index distinguishes between convergent areas that saturate frequently (large λ_i) and upslope regions lacking runoff production (small λ_i). In principle, a hydrologically-significant terrain model should preferentially resolve areas dominating the hydrologic response.

A method for constraining a TIN model based on a topographic index embeds the steady-state hydrologic behavior into the land surface representation (Figure 1.4). Instead of selecting DEM points based on elevation significance, the topographic index (Figure 1.4a) is used to classify points according to their hydrologic significance. For each topographic distribution class (Figure 1.4b), the method samples the DEM at a different resolution, retaining more points in frequently saturated areas. Although the Topmodel formation (1.1) is utilized, the methodology is amenable to other hydrologic similarity measures (*e.g.*, Ambroise *et al.*, 1996; Woods *et al.*, 1997).

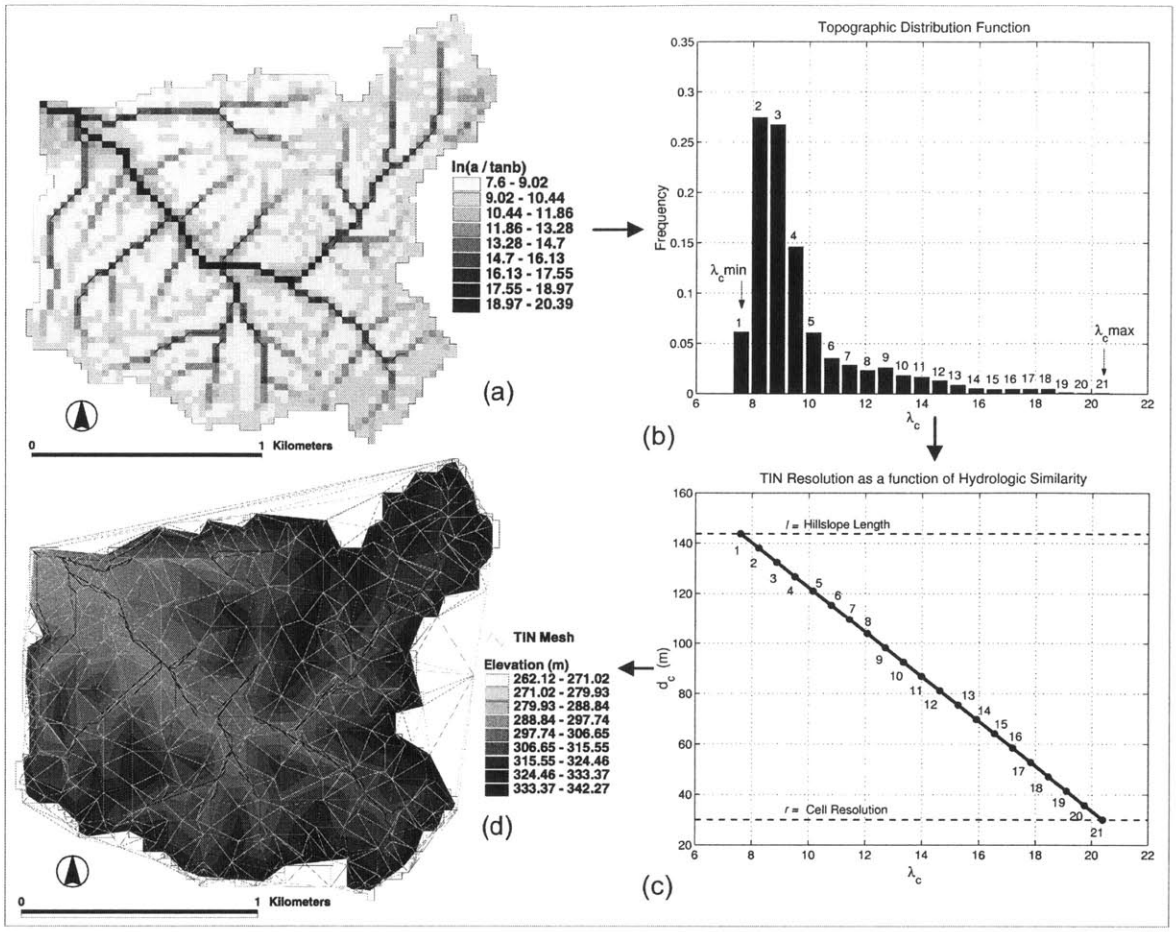

Figure 1.4. Hydrological similarity TINs. (a) Spatial distribution of topographic index; (b) Frequency distribution of λ arranged into 21 classes. (c) Linear relationship between the proximal distance (d_c) and index (λ_c); (d) TIN terrain model incorporating the topographic index, stream network and buffered watershed boundary.

To objectively select DEM points, a functional relationship (Figure 1.4c) is established between the mean index value of each class (λ_c) and the mean distance between points (d_c). The mean distance is used as a proximity criterion to filter the DEM. For simplicity, the relationship is assumed to be linearly decreasing over the λ_c range (although other functions can be accommodated). Minimum and maximum values for d_c are specified as the DEM resolution (r) and the mean hillslope length (l) computed from the total stream length (L_T) and catchment area (A):

$$l = \frac{1}{2D_d} = \frac{A}{2L_T} \tag{1.2}$$

where D_d is the basin drainage density. Drainage density is a key basin descriptor closely related to the long-term hydrologic response (*e.g.*, Tucker *et al.*, 2001a). For the linear relationship, the method depends only on r and l, computed directly from the DEM, without the need to specify an accuracy parameter (such as v or z_r).

In summary, the technique samples a DEM with a variable filter conditioned on the topographic index. Physical limits on the filter size ensure that hillslopes and convergent areas are sampled at low (l) or high resolution (r). Resolving the hillslope length guarantees that this natural landscape scale is preserved (Zhang and Montgomery, 1994; Brasington and Richards, 1998). After point selection, constrained Delaunay triangulation is used to create a TIN that resembles the wetness index distribution (Figure 1.4d). The physical link between the terrain model and two basin descriptors (λ and D_d) provide a consistent means of developing *hydrological similarity* TINs for any basin.

1.4. Elevation Data Products

Methods for generating hydrologically-significant TIN terrain models are tested by utilizing United States Geological Survey (USGS) and Shuttle Radar Topography Mission (SRTM) DEMs. In the following, a brief description of each is presented.

1.4.1 USGS DEMs

The USGS has developed a national topographic coverage containing the best available DEM products at various accuracy levels (Gesch *et al.*, 2002). Comparisons of DEM accuracy to higher resolution data from photogrammetry and surveying suggest the products are reasonable approximations, although localized errors are possible (*e.g.*,

Watershed	x_o [dd]	y_o [dd]	A [km^2]	r [m]	n_g [#]	μ [m]	σ [m]	Δz [m]
Baron Fork, OK*	-94.84	35.92	808.15	30	897,944	346.54	59.02	367.88
Blue River, OK*	-96.24	34.00	1236.38	30	1,373,755	259.48	66.49	245.23
Cheat River, WV*	-79.68	39.12	1857.22	30	2,063,578	1000.56	185.07	1002
Flint River, GA*	-84.43	33.24	697.71	30	775,233	264.79	19.71	105
Illinois River, OK*	-94.57	36.13	1627.60	30	1,808,444	378.06	41.34	324.21
Squannacook River, MA*	-71.65	42.63	172.03	30	191,144	194.42	80.71	387.40
Abo Arroyo, NM+	-106.77	34.52	1000.51	84.473	140,212	1846.86	236.35	1593
Cow Creek, OR+	-123.44	42.92	992.75	26.835	1,378,595	666.43	184.09	1353
Gun River, MI+	-85.64	42.47	268.35	26.839	372,537	217.36	21.69	118
Little Lost Creek, MO+	-91.32	38.71	110.37	27.528	145,647	208.22	31.28	152
Lost Creek, UT+	-111.54	41.06	576.92	27.012	790,682	2158.26	195.50	1018
Picacho Wash, AZ+	-114.62	32.80	96.83	28.462	119,531	183.34	56.98	538
Rapidan River, VA+	-78.03	38.32	1182.79	27.538	1,559,706	226.68	222.68	1135
Smith Canyon, CO+	-103.43	37.76	734.67	27.691	958,109	1536.68	134.11	634

Table 1.1. Characteristics of selected watersheds extracted from USGS (*) and SRTM (+) DEM data. x_o and y_o are the longitude and latitude of the watershed outlet (decimal degrees); A is the basin area (km^2); r is the grid cell resolution (m); n_g is the number of DEM cells; μ is the mean elevation (m); σ is the elevation standard deviation (m); Δz is the elevation range (m).

Kenward *et al.*, 2000). For Level-2 DEMs, the vertical accuracy and discretization is one-half the contour interval and values to the nearest unit (USGS, 1998). Despite potential artifacts, the USGS DEMs provide extensive data for testing the TIN algorithms. A series of six watersheds are utilized in this chapter (Table 1.1).

1.4.2 SRTM DEMs

SRTM DEMs are an emerging source of high-resolution topography data obtained using a radar interferometry onboard the Endevour Shuttle (Farr and Kobrick, 2000). The sampling technique consisted of two radar instrument pairs separated by a 60-m mast. Processing of the C-band data will provide a nominal 30-m product over 80% of the Earth's landmass. A preliminary distribution of 1- and 3-arcsecond (SRTM-1 and SRTM-3) products has been made for evaluation purposes. Vertical accuracy is estimated at 15-

meters with discretization to the nearest meter (Farr and Kobrick, 2000). In this chapter, a series of eight watersheds were chosen for testing the TIN algorithms (Table 1.1).

1.5. Applications

In this chapter, we developed a terrain analysis package in Arc/Info to generate the traditional, hydrographic or hydrological similarity TINs previously described. In the following, several case studies are presented to demonstrate the GIS methodology. In particular, we address five related issues: (1) How do TIN terrain models compare to DEM aggregation products? (2) Can TIN terrain models reveal differences in DEM products? (3) How does terrain variability affect TIN model performance? (4) How do hydrological similarity TINs compare with traditional methods? (5) Is it possible to construct TIN models of continental basins that capture hydrologic behavior?

Comparisons between the aggregated DEM and TIN models are quantitatively assessed using the frequency distribution of primary and secondary terrain descriptors (Moore *et al.*, 1991). The TIN surface is linearly interpolated onto a raster grid of equal dimensions to the DEM prior to deriving the elevation, slope, curvature and topographic index distributions. Slope and curvature are computed using algorithms in Moore *et al.* (1991), while the topographic index is based on the single-flow algorithm in Wolock and McCabe (1995). Finally, a qualitative assessment is obtained by visualizing the terrains.

1.5.1 Comparison of DEM aggregation and TINs

DEM aggregation leads to smoothing of critical slopes and shortening of flow paths which directly impact flow and erosion predictions (*e.g.*, Vieux, 1991; Walker and Willgoose, 1999). This effect is illustrated using the SRTM DEM for the Lost Creek

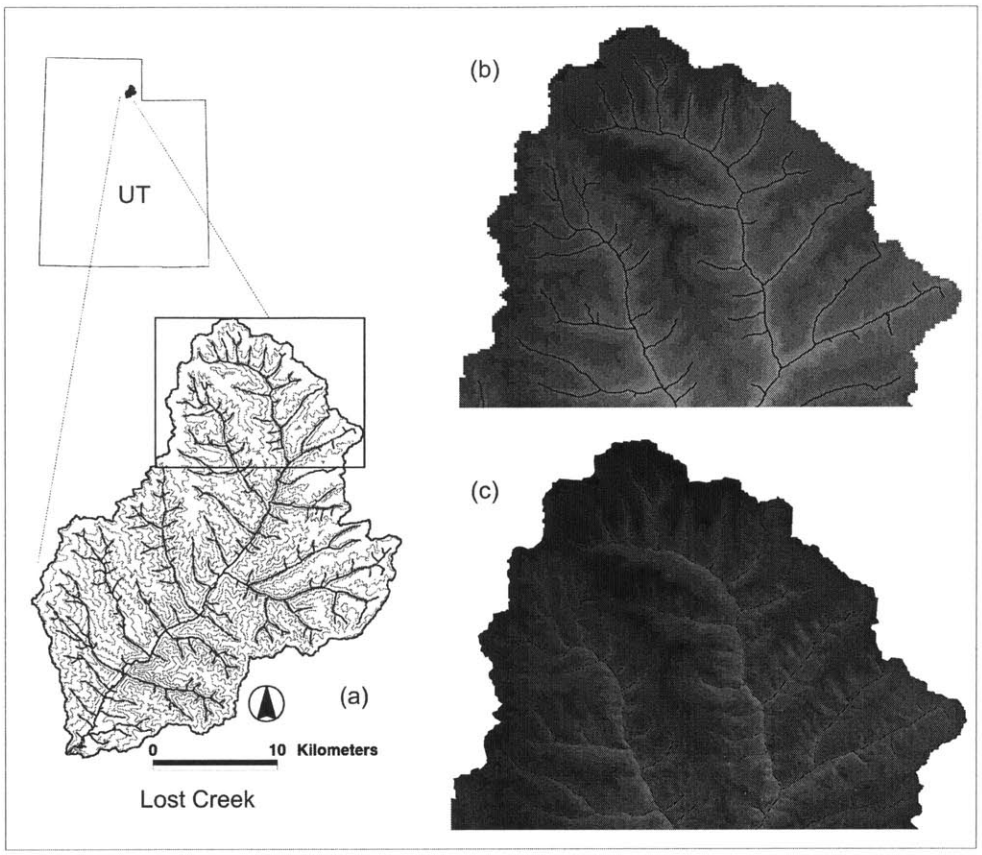

Figure 1.5. Visual comparison of DEM aggregation and hydrographic TIN terrain products for the Lost Creek basin, UT (577 km^2). (a) Contour map of the SRTM-1 watershed and stream networks (100-m interval); (b) Aggregated DEM at 81-m resolution; (c) Hydrographic TIN model at an equivalent data reduction factor (d = 0.12).

basin (Figure 1.5). Due to its high terrain variability, this basin exemplifies the potential errors occurring during aggregation. SRTM-1 data was transformed from its native 27-m resolution to 81-m using bilinear interpolation, a resolution equivalent to the SRTM-3 product (94,880 nodes). Comparisons are made to a *hydrographic* TIN derived using a topographic criteria, stream network and basin boundary. The elevation tolerance (z_r = 4 m) was chosen so the data reduction factor (d = 0.12) matched the aggregation in the 81-m DEM. Despite the low aggregation, the distribution of slope and curvature vary considerably for the aggregated DEM, while the elevation is unaffected (Figure 1.6). The hydrographic TIN model, however, preserves the terrain attributes well considering that

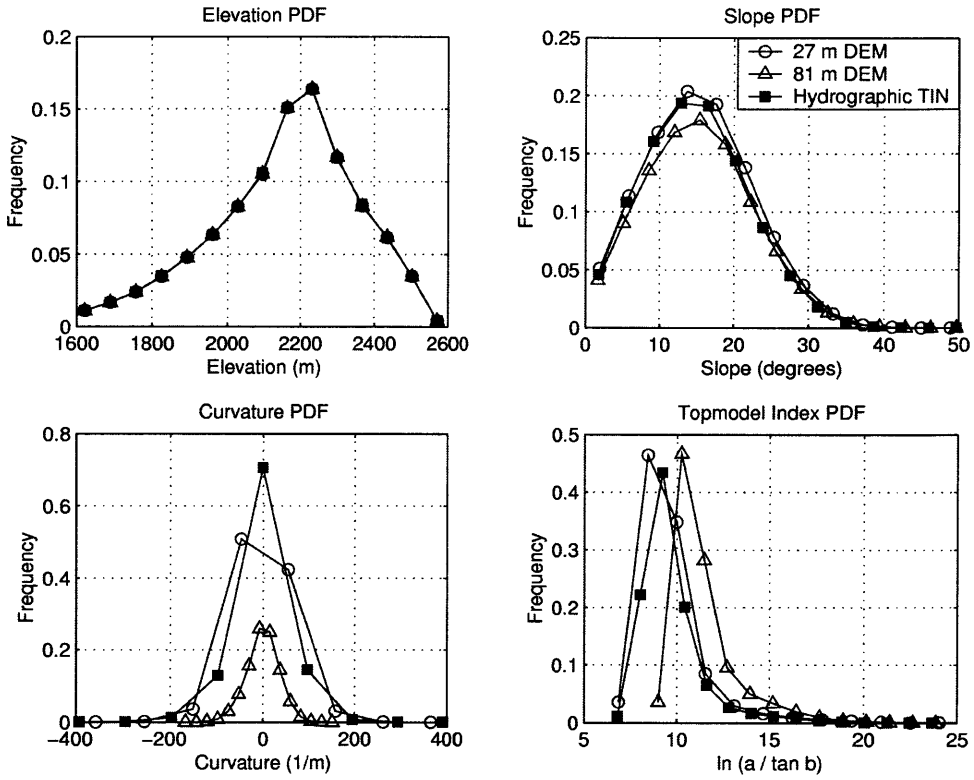

Figure 1.6. Comparison of the effect of DEM aggregation and TIN modeling on topographic attributes in the Lost Creek basin. The probability mass function (PMF) of elevation, slope, curvature and topographic index are shown for the original SRTM-1 DEM (27-m), the aggregated DEM (81-m) and the hydrographic TIN model.

12% of original nodes are retained in the triangulation. Additional test results indicate that as aggregation increases, TINs progressively capture more topographic information as compared to a low resolution DEM of an equivalent reduction factor, *d*.

1.5.2 Comparison of USGS and SRTM DEMs using TINs

Topographic data quality varies with the methods employed for capturing and processing elevation measurements. To illustrate the differences between the USGS and SRTM DEMs, we compare the two derived *hydrographic* TIN models for Smith Canyon (Figure 1.7). The data is sampled using the Latticetin method (z_r = 4 m) to ensure a data reduction factor of $d = 0.10$. DEM differences propagate to variations in the stream

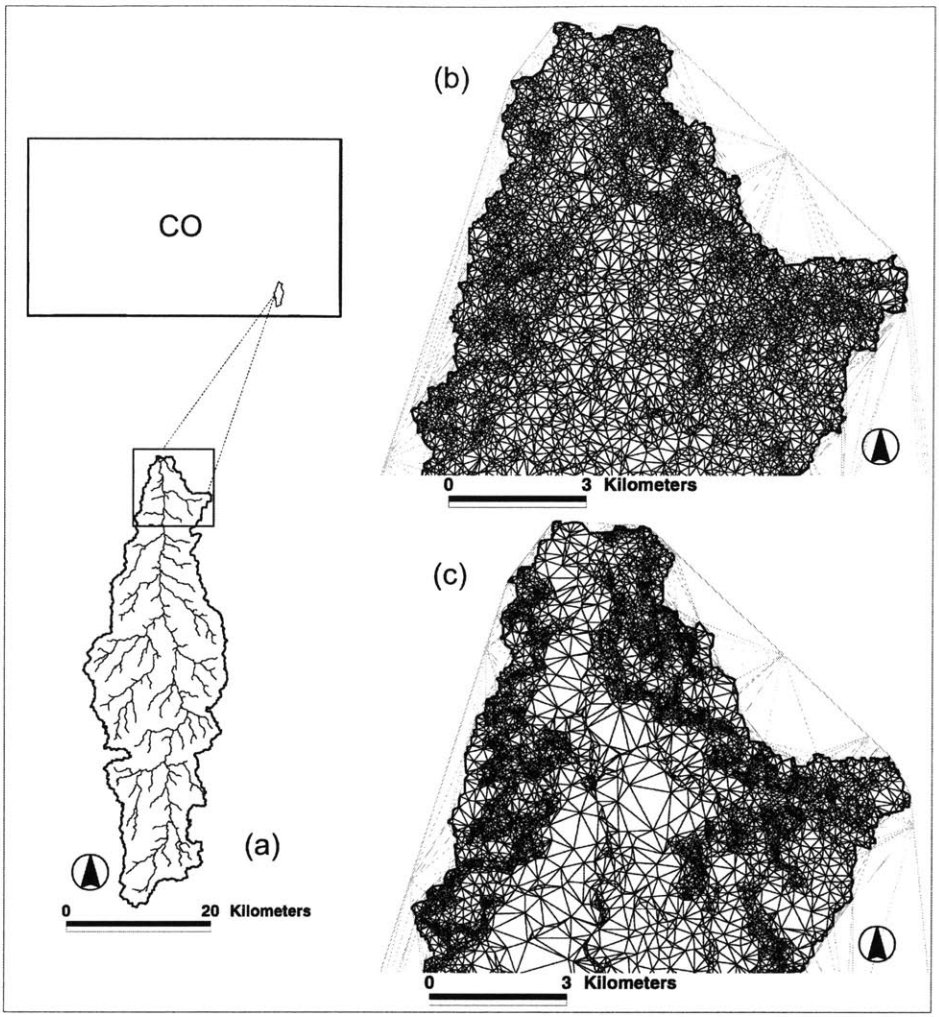

Figure 1.7. Comparison of USGS and SRTM DEMs using hydrographic TIN terrain models for the Smith Canyon, CO (735 km^2). (a) USGS watershed boundary and stream network; (b) Hydrographic TIN model using SRTM-1 DEM; (c) USGS DEM-derived hydrographic TIN model.

network, basin boundary and TIN terrain. Despite identical procedures, the SRTM TIN contains 75,025 nodes as compared to 99,958 in the USGS TIN. In flat regions, the SRTM TIN captures more elevation variability, whereas over rugged terrain the USGS TIN has higher resolution due to larger point-to-point variations. Visual comparison of the two terrain models suggest that TINs are a promising tool for discerning differences in elevation products. In addition, a comparison of the terrain frequency distributions for

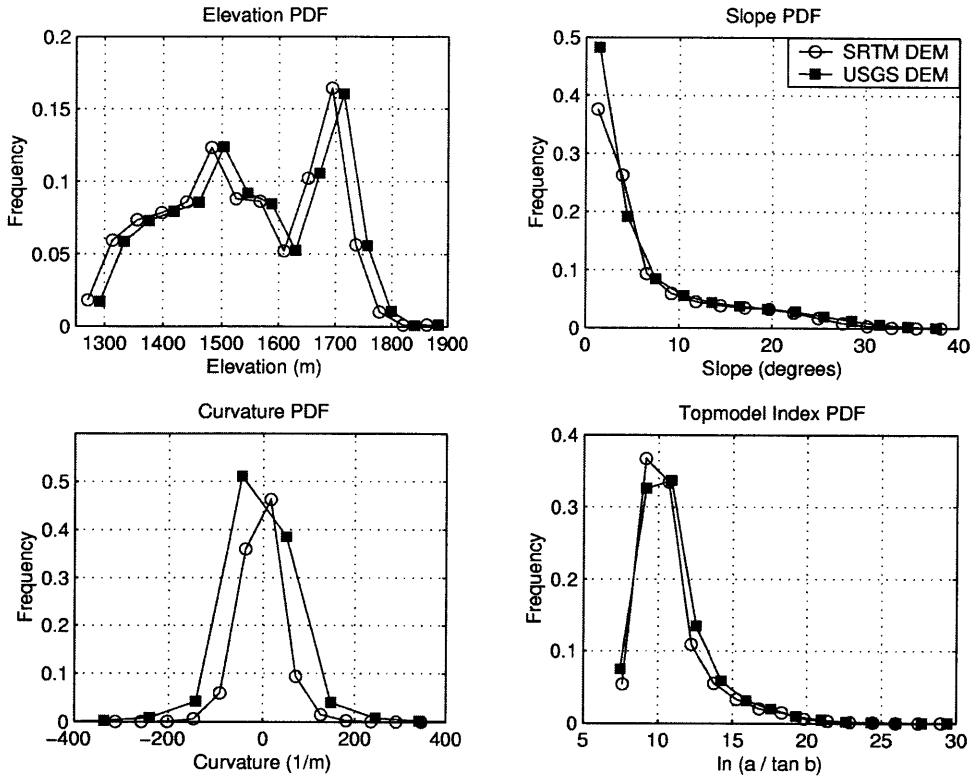

Figure 1.8. Comparison of the frequency distribution (PMF) of terrain attributes (elevation, slope, curvature and topographic index) for the SRTM-1 and USGS DEMs in Smith Canyon basin.

the SRTM and USGS DEMs show an elevation bias between the data sets and a higher proportion of low slopes for the USGS DEM (Figure 1.8). This agrees well with the observation of larger triangles in the canyon bottom for the USGS TIN. Results from comparisons in seven other USGS-SRTM basin pairs (Table 1.1) further suggest that TIN characterizations concisely capture differences in DEM products.

1.5.3 Comparison of TINs over varying terrain

The performance of the *hydrographic* TIN models over various basins is evaluated to investigate the dependency on terrain roughness. Model performance is measured by the RMSE between the original DEM and TIN model, while roughness is

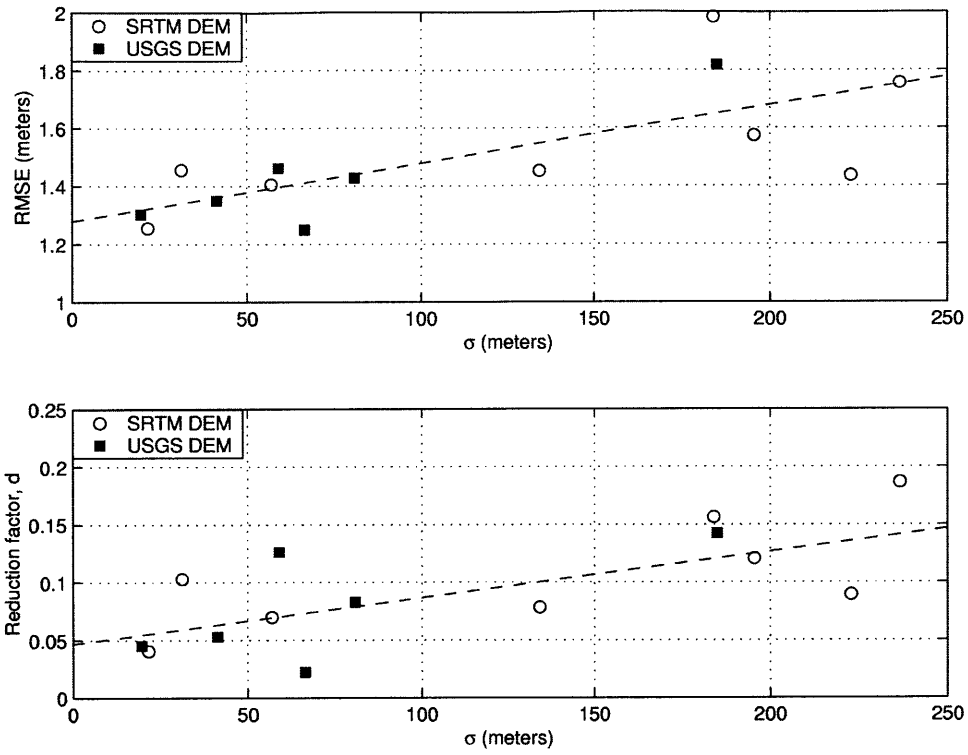

Figure 1.9. Performance of the hydrographic TIN method for a series of 6 USGS and 8 SRTM DEMs. (top) The root mean square error (RMSE) between TIN and DEM models increases with terrain variability (σ). (bottom) The data reduction factor ($d = n_t/n_g$) increases with σ. Dashed lines represent a linear regression in each relationship.

represented by the standard deviation in elevation (σ). A series of watersheds were selected to ensure topographic heterogeneity with σ ranging from 20 to 220 meters (Table 1.1). Hydrographic TINs were generated for each basin using an identical elevation tolerance (z_r = 4 m). Figure 1.9 illustrates how an increase in terrain variability (σ) leads to a higher RMSE. Terrain roughness also impacts the data reduction factor (d) achievable with a TIN model. Watersheds with low terrain variability can be represented with fewer TIN nodes (low d) and improved accuracy (low RMSE) for a given tolerance level (z_r). Despite a dependency on roughness, hydrographic TIN models have a RMSE

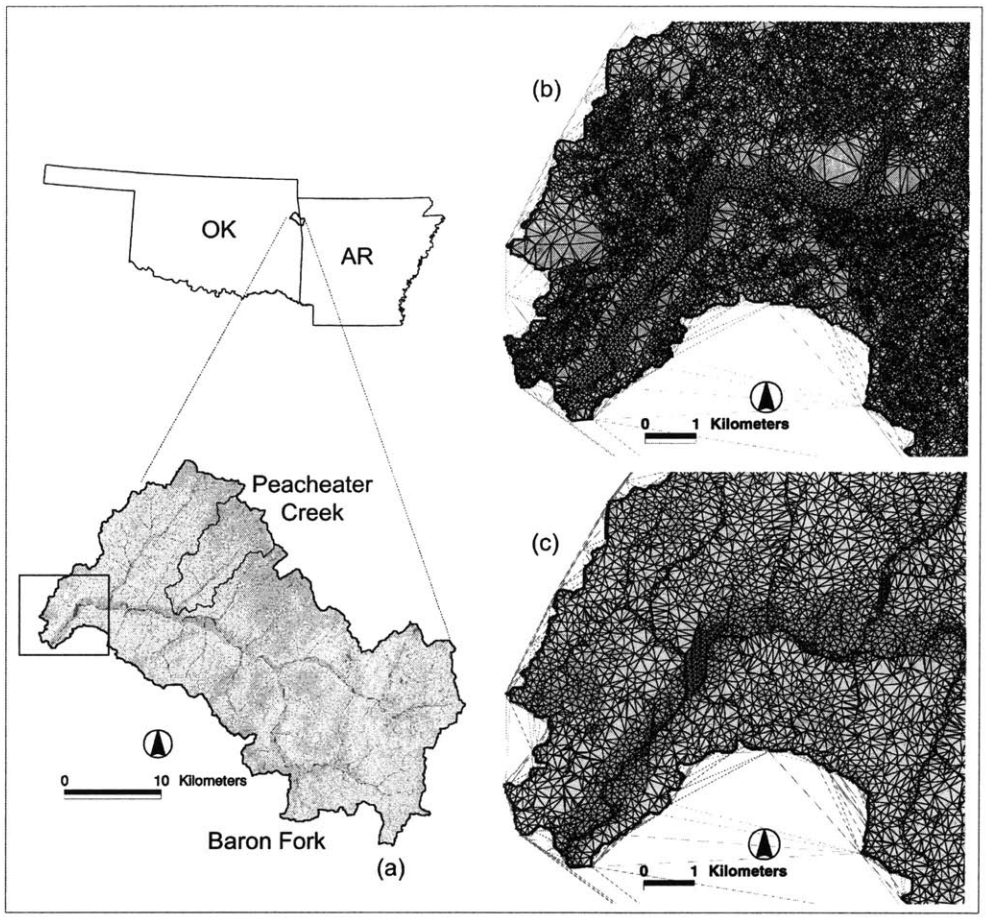

Figure 1.10. Visual comparison of the TIN methods for the Baron Fork (808 km^2) and Peacheater Creek (64 km^2) basins, OK, from a 30-m USGS DEM. (a) Spatial distribution of topographic index; (b) Hydrographic TIN generated using the Latticetin method (z_r = 6.8 m), stream network and floodplain; (c) Hydrological similarity TIN with the proximity criterion (d_c) varying from r = 30 m to l = 579 m.

of less than 2 meters while using 20% or fewer of the original DEM points. Additional tests suggest that TIN performance is largely independent of catchment size (A).

1.5.4 Comparison of hydrologically-significant TINs at two scales

The *hydrological similarity* TIN method resolves terrain based on the wetness index, rather than using a topographic criterion. In order to assess its performance, comparisons are made to a 30-m USGS DEM, an aggregated DEM and a hydrographic TIN model for the Baron Fork basin (808 km^2). The same data reduction factor (d = 0.07;

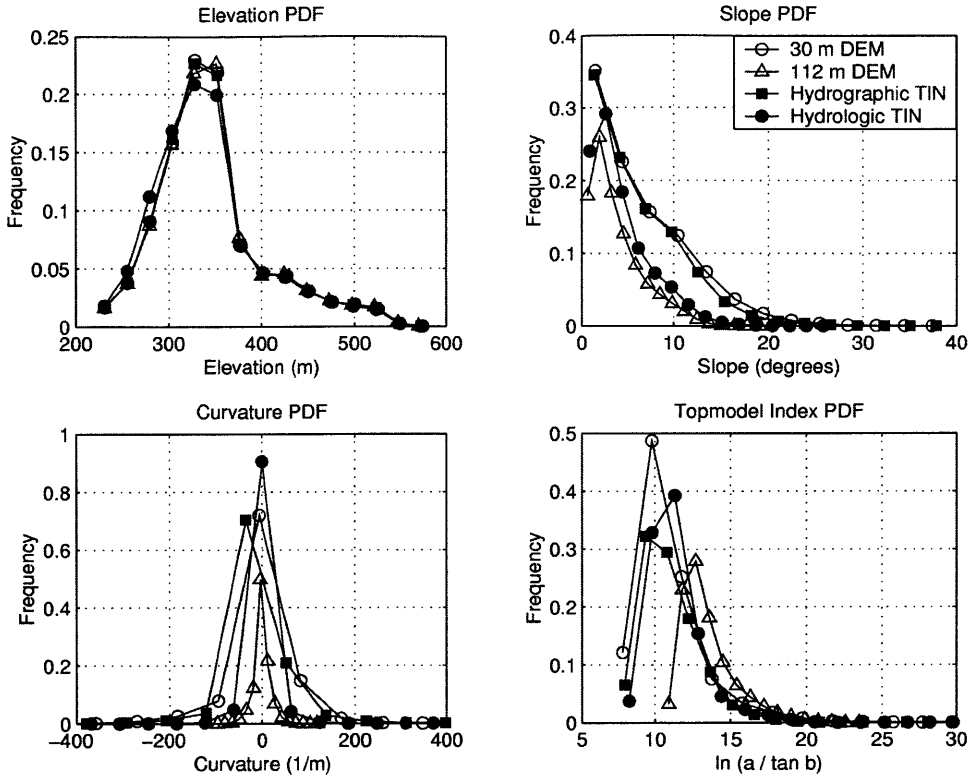

Figure 1.11. Comparison of frequency distributions (PMF) of elevation, slope, curvature and topographic index for the Baron Fork watershed. Included are the original USGS 30-m DEM, a DEM aggregation at 112-m resolution, a hydrographic TIN model and a hydrological similarity TIN model.

n_t = 64,000 nodes) is used for the hydrographic TIN (z_r = 6.8 m), hydrological similarity TIN and the DEM aggregation (r = 112 m). Visual comparison of the TIN models reveals differences in features and resolution (Figure 1.10). The performance of the hydrological similarity TIN is adequate in terms of the terrain attribute distributions as compared to DEM aggregation (Figure 1.11). While the slope distribution is not preserved well, the topographic index distribution is improved for areas that saturate frequently (large λ_i).

The nested Peacheater Creek basin (64 km^2) is used to evaluate the performance of the TIN methods across scales. We extracted the 30-m DEM, 112-m DEM, hydrographic TIN and hydrological similarity TIN for Peacheater Creek directly from the

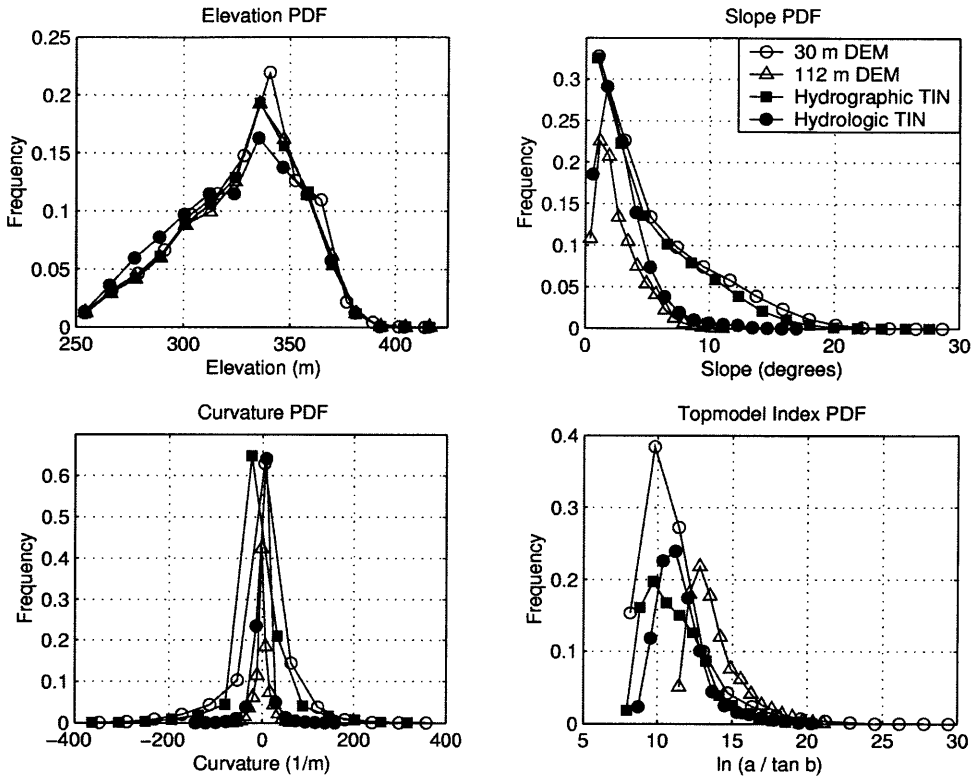

Figure 1.12. Comparison of frequency distributions (PMF) of terrain attributes for the Peacheater Creek watershed sampled directly from the Baron Fork models.

Baron Fork terrain models. The terrain attribute distributions reveal that the TIN methods performed equally well at the sub-basin scale as compared to the larger scale (Figure 1.12). As observed for Baron Fork, the similarity TIN was better than the hydrographic TIN at capturing the wetness index distribution but worse for the slope distribution. Notably, the performance of the aggregated DEM worsened when evaluated in the sub-basin. This suggests that TIN terrain models may be less susceptible to scale variations.

1.5.5 Continental-scale hydrological similarity TINs

The multiple resolutions afforded by TIN models capture the topographic detail in large-scale watersheds with a reduced set of elevation points. Here, we demonstrate the performance of the *hydrological similarity* TIN method for the Mississippi River basin,

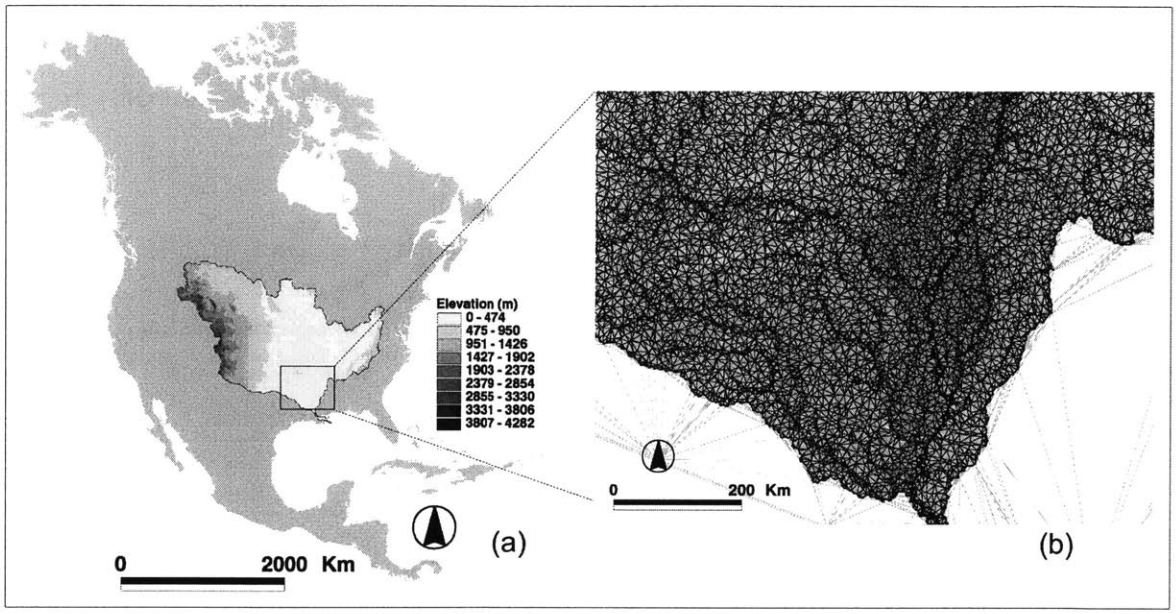

Figure 1.13. Continental-scale Mississippi River basin (3,196,675 km^2) (a) HYDRO1K DEM at 1 km grid resolution. (b) Hydrological similarity TIN terrain model.

approximately 3,196,675 km^2 in extent (Figure 1.13). Digital terrain data for the region is obtained from the North American HYDRO1K database (1 km), derived from the USGS 3-arcsecond DEMs. A low-resolution TIN commensurate with the computational capabilities of an existing TIN-based hydrology model is developed (Ivanov *et al.*, 2001). The TIN model (n_t = 101,756, d = 0.03) is compared with an aggregated DEM (5.65 km) corresponding to the same data reduction factor. Comparisons of the terrain frequency distributions demonstrate the superiority of the TIN model in capturing the hydrologic signature of the high-resolution data despite having 3% of the nodes (Figure 1.14).

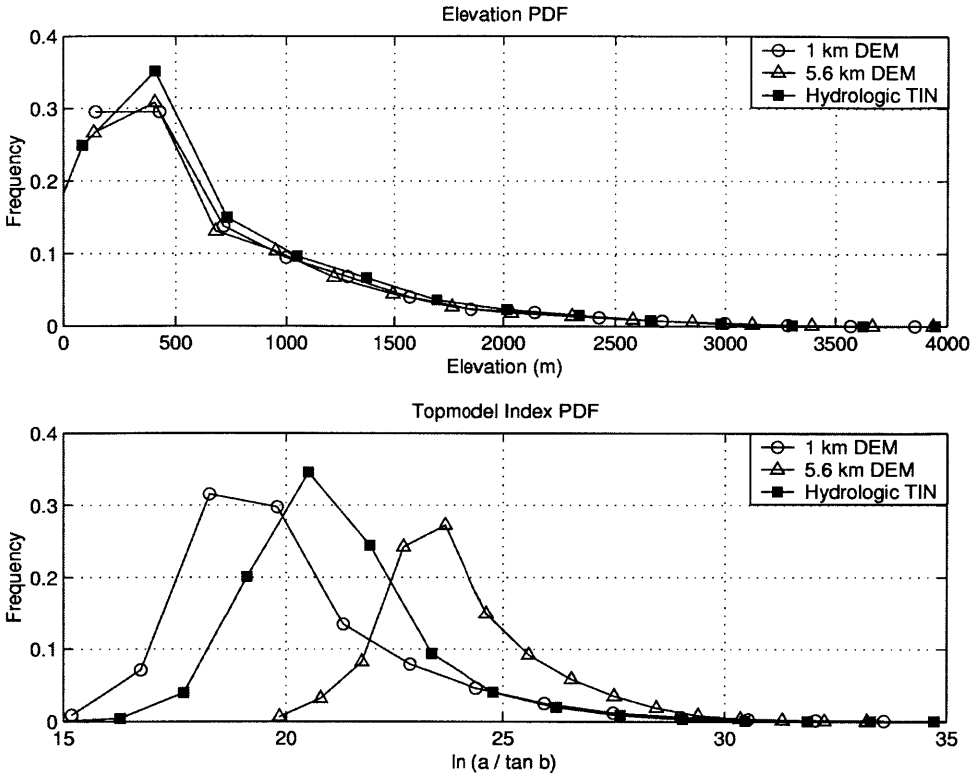

Figure 1.14. Comparison of the elevation (top) and topographic index (bottom) frequency distributions (PMF) for the Mississippi River using the HYDRO1K DEM (1 km), DEM aggregation (5.65 km) and the hydrologic similarity TIN model (d = 0.03).

1.6. Discussion

The case studies presented in this work demonstrate the advantages of utilizing multiple-resolution TINs for describing terrain. In the following, several key issues regarding the suitability of TIN terrains for hydrologic modeling are discussed.

1.6.1 Aggregation and hydrologic predictions

Extensive research has been performed in the hydrologic community on the effect of grid aggregation on model simulations. In general, it is well documented that aggregating DEMs from high to low resolution has primary, secondary and tertiary effects (*e.g.*, Zhang and Montgomery, 1994; Wolock and Price, 1994). Since raster and

topographic distribution hydrologic models are typically based on aggregated DEM data, the resolution dependency of model predictions is unavoidable. Most applications require a tradeoff between aggregation errors and computational demands when selecting the model resolution. For example, Vázquez *et al.* (2002) describe an exponential increase in computational time when linearly reducing the grid size of the MIKE SHE model.

Minimizing the tradeoff between model errors and execution time is desirable. TIN terrain models provide a way forward in this regard, retaining the statistical signature of the best available topographic data with at least an order of magnitude less number of elevation points. This degree of data reduction permits applications in large-scale watersheds without significant loss of topographic information. Nevertheless, triangulated irregular networks may also introduce aggregation errors. Both the methodology and the acceptable error level in TINs can potentially impact hydrologic simulations. Given the potential uses of TINs for hydrologic and geomorphic modeling, the propagation of TIN resolution error into model predictions needs to be addressed.

1.6.2 Hydrologic modeling using TINs

As compared to raster grids and contour methods, TIN models have received little attention in the hydrology community. Notable exceptions include the works of Palacios-Velez and Cuevas-Renaud (1992), Tachikawa *et al.* (1994), Nelson *et al.* (1999), Mita *et al.* (2001) and Tucker *et al.* (2001b). Despite clear advantages in representing terrain, the proliferation of TIN hydrologic models has been hindered by the complexity of data structures and algorithms on the irregular mesh (Tucker *et al.*, 2001b). In addition, few studies have clearly demonstrated the advantages of TIN-based hydrologic models.

A necessary step in the application of TIN-based models is the development of real-world TIN watersheds. This chapter provides the methodology for generating TIN terrain models using high-resolution raster DEMs and land-surface data. The hydrologically-significant TINs introduced here address many of the deficiencies identified in previous works, including conforming to boundaries and stream networks (Mita *et al.,* 2001), resolution dependence on both elevation and proximity to channels (Nelson *et al.*, 1999) and incorporation of landscape features such as floodplains, soil units or land cover. In addition, the use of topographic distribution function for constraining TIN models is a promising development for large-scale applications.

1.6.3 Multiple resolutions, scale and nesting

The capability of resolving terrain at multiple resolutions using hydrologic criteria creates opportunities to enhance the formulation of distributed hydrologic models. A low resolution, continental basin scale TIN model can host a higher resolution embedded triangulation for a specified sub-watershed. Triangulated irregular networks permit a smooth transition between the continental basin and its nested watersheds. The level of detail used to represent each basin can vary according to hydrologic process representation, availability of topographic data or hydrologic model construction. Furthermore, the hydrologic signature at each scale can be preserved through a physical link to the characteristics (drainage density and topographic index) of the nested basins. As a result, hydrological similarity TINs that properly resolve both the large and small scale domains provide a means for enhancing distributed hydrogeomorphic models.

1.7. Conclusions

In this chapter, we present a variety of approaches for developing TIN models for hydrologic applications. The methodology accounts for catchment topographic, hydrographic and landscape features. Used in conjunction, these methods lead to hydrologically-significant TIN models of real-world terrain. Advantages include a reduction in computational elements without significant information loss. In addition, a new method for sampling dense DEMs with a topographic index is presented as means for constraining TIN generation. Conceptually, hydrologic similarity optimally represents the steady-state runoff response within the TIN mesh structure.

Through a series of applications utilizing both USGS and SRTM DEMs, we illustrate and quantify the performance of the TIN methods. Hydrographic TIN methods using an elevation criterion are successful in capturing the statistical distribution of primary and secondary terrain attributes. The hydrological similarity TIN methods outperform traditional methods when capturing the hydrologic signature in terrain. Most importantly, both methods minimize the significant negative effects introduced by DEM aggregation at equivalent reduction factors.

In large-scale hydrology models, TINs may improve land-surface simulations without increasing computational demands. While aggregation schemes introduce artifacts, hydrological similarity TINs capture the topographic signature with few nodes. In addition, the new method bridges two existing modeling approaches: topographic distribution functions and finite-element meshes. By deriving the TIN using a similarity measure, the proposed method resolves critical hydrologic features (*e.g.*, variable source area) within a basin.

References

Ambroise, B., Beven, K. and Freer, J. 1996. Toward a generalization of the Topmodel concepts: topographic indices of hydrological similarity. *Water Resources Research.* 32(7), 2135-2145.

Barling, R.D., Moore, I.D. and Grayson, R.B. 1994. A quasi-dynamic wetness index for characterizing the spatial distribution of zones of saturation and soil water content. *Water Resources Research.* 30(4), 1029-1044.

Beven, K.J. and Kirkby, M.J. 1979. A physically-based variable contributing area model of basin hydrology. *Hydrological Sciences Bulletin.* 24, 43-69.

Brasington, J. and Richards, K. 1998. Interaction between model predictions, parameters and DTM scales for Topmodel. *Computers & Geosciences.* 24(4), 299-314.

Douglas, D.H. and Peucker, T.K. 1973. Algorithms for the reduction of the number of points required to represent a digitized line or its caricature. *Canadian Cartographer.* 10(2), 112-122.

Environmental Research Systems Institute. 1992. *Understanding GIS: the Arc/Info method.* ESRI Press. Redlands, CA. 400 pgs.

Gesch, D., Oimoen, M., Greenlee, S., Nelson, C., Steuck, M. and Tyler, D. 2002. The national elevation dataset. *Photogrammetric Engineering and Remote Sensing.* 68(1), 5-15.

Goodrich, D.C., Woolhiser, D.A. and Keefer, T.O. 1991. Kinematic routing using finite elements on a triangular irregular network. *Water Resources Research.* 27(6), 995-1003.

Farr, T.G. and Kobrick, M. 2000. Shuttle Radar Topography Mission produces a wealth of data. *American Geophysical Union. EOS*, 81, 583-585.

Heckbert, P.S. and Garland, M. 1997. Survey of polygonal surface simplification algorithms. *Carnegie Mellon University Technical Report.* Pittsburgh, PA.

Ivanov, V.Y., Vivoni, E.R., Bras, R.L. and Entekhabi, D. 2001. Development of a distributed hydrologic model using triangulated irregular networks for continuous, real-time flood forecasting. *EOS Transactions AGU.* 82(46), H31D-02.

Jenson, S.K. and Domingue, J.O. 1988. Extracting topographic structure form digital elevation data for geographic information system analysis. *Photogrammetric Engineering and Remote Sensing.* 54(11): 1593-1600.

Jones, N.L., Wright, S.G. and Maidment, D.R. 1990. Watershed delineation with triangle-based terrain models. *Journal of Hydraulic Engineering.* 116(10), 1232-1251.

Kenward, T., Lettenmaier, D.P., Wood, E.F. and Fielding, E. 2000. Effect of digital elevation model accuracy on hydrologic predictions. *Remote Sensing of the Environment.* 74, 432-444.

Koster, R.D., Suarez, M.J., Ducharne, A., Stieglitz, M. and Kumar, P. 2000. A catchment-based approach to modeling land surface processes in a general circulation model. *Journal of Geophysical Research.* 105(D20), 24809-24822.

Kouwen, N., Soulis, E.D., Pietroniro, A., Donald, J. and Harrington, R.A. 1993. Grouped response units for distributed hydrologic modeling. *Journal of Water Resources and Management.* 119(3), 289-305.

Kumler, M.P. 1994. An intensive comparison of triangulated irregular networks (TINs) and digital elevation models (DEMs). *Cartographica.* 31(2), Monograph 45, 48 pgs.

Lee, J. 1991. Comparison of existing methods for building triangular irregular network models of terrain from grid digital elevation models. *International Journal of Geographical Information Systems*. 5(3), 267-285.

Liang, C. and Mackay, D.S. 2000. A general model of watershed extraction and representation using globally optimal flow paths and up-slope contributing areas. *International Journal of Geographic Information Science*. 14(4), 337-358.

Mita, C., Catsaros, N. and Gounaris, N. 2001. Runoff cascades, channel network and computation hierarchy determination on a structured semi-irregular triangular grid. *Journal of Hydrology*. 244, 105-118.

Moore, I.D., Grayson, R.B. and Landson, A.R. 1991. Digital terrain modeling: a review of hydrological, geomorphological and biological applications. *Hydrological Processes*. 5, 3-30.

Nelson, E.J., Jones, N.L. and Miller A.W. 1994. Algorithm for precise drainage-basin delineation. *Journal of Hydraulic Engineering*. 120(3), 298-312.

Nelson, E.J., Jones, N.L. and Berrett, R.J. 1999. Adaptive tessellation method for creating TINs from GIS data. *Journal of Hydrologic Engineering*. 4(1), 2-9.

O'Callaghan, J.F. and Mark, D.M. 1984. The extraction of drainage networks from digital elevation data. *Computer Vision, Graphics and Image Processing*. 28, 323-344.

O'Loughlin, E.M. 1986. Prediction of surface saturation zones in natural catchments by topographic analysis. *Water Resources Research*. 22(5), 794-804.

Palacios-Velez, O.L. and Cuevas-Renaud, B. 1986. Automated river-course, ridge and basin delineation from digital elevation data. *Journal of Hydrology*. 86, 299-314.

Palacios-Velez, O.L. and Cuevas-Renaud, B. 1992. SHIFT: A distributed runoff model using irregular triangular facets. *Journal of Hydrology*. 134, 32-55.

Tachikawa, Y., Shiiba, M. and Takasao, T. 1994. Development of a basin geomorphic information system using TIN-DEM data structure. *Water Resources Bulletin*. 30(1), 9-17.

Tate, E.C., Maidment, D.R., Olivera, F. and Anderson, D.J. 2002. Creating a terrain model for floodplain mapping. *Journal of Hydrologic Engineering*. 7(2), 100-108.

Tsai, V.J.D. 1993. Delaunay triangulations in TIN creation: an overview and a linear-time algorithm. *Int. Journal of Geographical Information Systems*. 7(6), 501-524.

Tucker, G.E., Catani, F., Rinaldo, A. and Bras, R.L. 2001a. Statistical analysis of drainage density from digital terrain data. *Geomorphology*. 36, 187-202.

Tucker, G.E., Lancaster, S.T., Gasparini, N.M., Bras, R.L. and Rybarczyk, S.M. 2001b. An object-oriented framework for distributed hydrologic and geomorphologic modeling using triangulated irregular networks. *Computers & Geosciences*. 27(8), 959-973.

USGS 1998. *Standards for Digital Elevation Models. National Mapping Technical Instructions*. Department of the Interior, USGS, Reston, VA.

Vázquez, R.F., Feyen, L., Feyen, J. and Refsgaard, J.C. 2002. Effect of grid size on effective parameters and model performance of the MIKE-SHE code. *Hydrological Processes*. 16, 355-372.

Vieux, B.E. 1991. DEM aggregation and smoothing effects on surface runoff modeling. *Journal of Computing in Civil Engineering*. 7(3), 310-338.

Walker, J.P. and Willgoose, G.R. 1999. On the effect of digital elevation model accuracy on hydrology and geomorphology. *Water Resources Research*. 35(7), 2259-2268.

Warrach, K., Stieglitz, M., Mengelkamp, H-T. and Raschke, E. 2002. Advantages of a topographically controlled runoff simulation in a soil-vegetation-atmosphere transfer model. *Journal of Hydrometeorology*. 3(2), 131-148.

Watson, D.F. and Philip, G.M. 1984. Systematic triangulations. *Computer Vision, Graphics, and Image Processing*. 26, 217-223.

Williams, W.A., Jensen, M.E., Winne, J.C. and Redmond, R.L. 2000. An automated technique for delineating and characterizing valley-bottoms settings. *Environmental Monitoring and Assessment*. 64, 105-114.

Wood, E.F., Sivapalan, M. and Beven, K. 1990. Similarity and scale in catchment storm response. *Reviews of Geophysics*. 28(1), 1-18.

Wood, E.F., Lettenmaeir, D., Liang, X., Nijssen, B. and Wetzel, S.W. 1997. Hydrologic modeling of continental-scale basins. *Annual Reviews of Earth and Planetary Sciences*. 25, 279-300.

Woods, R.A., Sivapalan, M. and Robinson, J. S. 1997. Modeling the spatial variability of subsurface runoff using a topographic index. *Water Resources Research*. 33(5), 1061-1073.

Wolock, D.M. and McCabe, G.J. 1995. Comparison of single and multiple flow direction algorithms for computing topographic parameters in TOPMODEL. *Water Resources Research*. 31(5), 1315-1324.

Wolock, D.M. and Price, C.V. 1994. Effects of digital elevation model map scale and data resolution on a topography-based watershed model. *Water Resources Research*. 30(11), 3041-3052.

Zhang, W. and Montgomery, D.R. 1994. Digital elevation model grid size, landscape resolution, and hydrologic simulations. *Water Resources Research*. 30(4), 1019-1028.

Chapter 2:

Distributed Hydrologic Modeling using Triangulated Terrain

2.1 Introduction

Numerical models of landscape processes are powerful tools for simulating the transient hydrogeomorphology of real-world systems. Given a set of process descriptions, distributed models provide both the integrated system and internal catchment response. By representing a domain with numerous sub-elements, these models incorporate heterogeneities in surface descriptors, forcings and initial or boundary conditions explicitly into the simulation. Topography is particularly important due to its control on hydrogeomorphic processes and the demonstrated model sensitivity to terrain resolution (*e.g.*, Walker and Willgoose, 1999). Here, we outline two distributed models employed in later chapters, the Channel Hillslope Integrated Landscape Development (CHILD) and TIN-based Real-time Integrated Basin Simulator (tRIBS) models. Attention is primarily focused on the description of the tRIBS model including the model parameterizations for coupled unsaturated-saturated dynamics, runoff generation, flow routing, and surface energy balance. The reader is referred to Ivanov *et al.* (2003a,b) for further details.

2.1.1 Channel-Hillslope Integrated Landscape Development (CHILD)

The CHILD model simulates watershed-scale changes in landscape morphology resulting from channel and hillslope processes. The model incorporates climatic forcing, runoff production, sediment transport, soil creep, floodplain deposition and meander evolution, among others (Tucker *et al.*, 2001a,b; Lancaster and Bras, 2002). Although CHILD is formulated to represent erosion dynamics over years to epochs, recent work

has focused on short-term sediment transport (Teles and Bras, 2002). For these applications, the initial topography is specified by developing a TIN from high-resolution DEMs. During a simulation, the effect of erosion and deposition on topography is captured by dynamically remeshing the domain after vertical node displacement. Another recent development is a shallow landslide component within CHILD (Teles *et al.*, 2002).

2.1.2 TIN-based Real-time Integrated Basin Simulator (tRIBS)

The tRIBS model is a distributed hydrologic forecasting tool for real-time, continuous operation (Ivanov *et al.*, 2003). The model utilizes hydrometeorological forcing to predict the surface and subsurface hydrologic basin response. Currently, model verifications have been limited to the streamflow at outlet and interior gauges. Nevertheless, the spatial distribution of hydrologic fluxes and states can be simulated for periods of up to several years. As in short-term CHILD applications, topography is represented using a variable TIN derived from DEM data (Vivoni *et al.*, 2002). Contrary to CHILD, the mesh is held constant during simulations, underlining the importance of the initial terrain representation. Model resolution is particularly important in convergent areas that saturate frequently and produce runoff.

Hydrologic processes are computed on a TIN composed of nodes, edges and triangles. Tucker *et al.* (2001b) describes the geometry and data structure of the irregular mesh. Figure 2.1 illustrates the hydrologic and energy processes represented in the model for a complex catchment, as summarized in Table 2.1. Over the TIN terrain, the model uses rainfall and meteorological forcing from rain gauges or weather radar to predict the distributed basin response, including infiltration, runoff, evapotranspiration, soil moisture and aquifer recharge. Ivanov *et al.* (2003a,b) provide detailed descriptions of the model

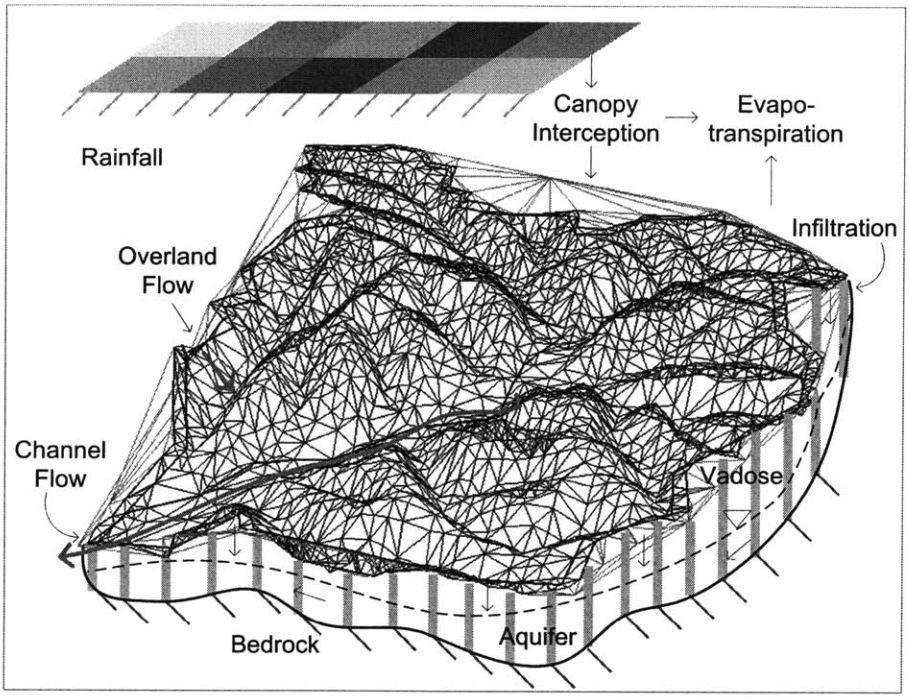

Figure 2.1. Coupled hydrologic processes represented in the tRIBS model simulated over a complex triangulated terrain.

components, including the parameterizations for coupled unsaturated-saturated dynamics, runoff production and routing, and moisture redistribution through the hillslope system.

tRIBS is designed to simulate both the surface and subsurface response to rainfall by tracking infiltration fronts, water table fluctuations and lateral moisture exchanges. Runoff is generated via four mechanisms: infiltration-excess runoff, saturation-excess runoff, perched return flow and groundwater exfiltration. Routing of surface flow is achieved via overland and channel pathways. Evaporation from bare soil, vegetation and rain interception are calculated via a surface radiation and energy balance. Hydrologic states and fluxes are computed using the Voronoi polygon associated with each node. A unique set of Voronoi polygons is created for a TIN by intersecting the perpendicular bisectors of each triangle edge (Tucker *et al.*, 2001b). These irregular polygons surround a TIN node and form the basis for finite-volume computations within the model.

2.2 A Coupled Surface-Subsurface Model: tRIBS

tRIBS is a continuous, physically-based, distributed-parameter model designed for hydrologic research and forecasting (Ivanov *et al.*, 2003a). The model provides spatially-explicit treatment of heterogeneities in topography, soils and aquifer properties, vegetation and land-use, and rainfall and atmospheric forcing. As with grid-based models (*e.g.*, Abbott *et al.*, 1986, Wigmosta *et al.*, 1994), continuous runoff production and routing are tracked over terrain represented at individual nodes. Hydrologic dynamics are available as time series and spatial maps representing the integrated and distributed response to hydrometeorological forcing.

2.2.1 Model domain representation

A catchment is represented in tRIBS through a three-dimensional TIN consisting of elevation, channel network, and watershed boundary nodes (Vivoni *et al.*, 2002). Triangulated irregular networks are a piece-wise linear interpolation of a set of points, sampled from DEMs, resulting in triangular facets of varying size. The triangulation represents topographically complex surfaces that include hillslopes and valleys, floodplains and riparian zones, and mountain ridges. The stream network is composed of a set of channels ranging from headwater tributaries to large, meandering rivers. The channel profile is captured from the topographic surface while the cross section is established through geomorphic relations or field measurements (Ivanov *et al.*, 2003b). The soil profile and shallow aquifer are bounded by a spatially-distributed bedrock topography assumed to be an impermeable surface. The shallow aquifer interacts with the stream network and land surface to produce surface saturated areas that expand and contract with respect to the level of catchment recharge (*e.g.*, de Vries, 1995).

Model Process	*Description*
Rainfall Interception	Canopy water balance model
Surface Energy Balance	Combination equation (λE), Gradient method (H) and Force-restore equation (G)
Surface Radiation Model	Short-wave and long-wave components accounting for terrain variability
Evapotranspiration	Bare soil evaporation, transpiration and evaporation from wet canopy
Infiltration	Kinematic approximation with capillarity effects; unsaturated, saturated and perched conditions; top and wetting infiltration fronts
Lateral Vadose Flow	Topography-driven lateral unsaturated and saturated vadose flow
Runoff Production	Infiltration-excess, saturation-excess, perched return flow and groundwater exfiltration
Groundwater Flow	Two dimensional flow in multiple directions, dynamic water table
Overland Flow	Nonlinear hydrologic routing
Channel Flow	Kinematic wave hydraulic routing

Table 2.1. Hydrologic components of the tRIBS distributed hydrologic model.

2.2.2 Coupled unsaturated and saturated dynamics

Hydrological response requires an appropriate depiction of the two-way interaction between surface and subsurface processes. On the TIN domain, tRIBS models the relationship between the vadose and saturated zones by accounting for dynamic infiltration fronts and water table depths (Ivanov *et al.*, 2003a). The continuous model can deal with multiple storm events and handle losses due to evapotranspiration and groundwater drainage. Each element consists of a sloped column of heterogeneous, anisotropic soil characterized by an exponential decrease in saturated hydraulic conductivity (*e.g.*, Beven and Kirkby, 1979, Beven, 1982):

$$K_{Si}(z) = K_{oi}\exp(-fz), \tag{2.1}$$

where K_{Si} is the saturated hydraulic conductivity at depth z, with $z = 0$ at terrain surface, in the normal or parallel directions ($i = n$ or p), K_{oi} is the surface conductivity, and f is a

decay parameter. A kinematic approximation for unsaturated flow developed by Cabral *et al.* (1992), Garrote and Bras (1995) and Ivanov (2000) is used to compute infiltration and propagate moisture fronts in the soil column. The unsaturated moisture profile is determined from hydrostatic equilibrium using the Brook and Corey (1964) parameterization and Miller and Miller (1956) scaling (Ivanov *et al.,* 2003a):

$$\theta(z) = \theta_r + (\theta_s - \theta_r)\left[\frac{\psi_b}{z - N_{wt}}\right]^{\lambda_o}, \tag{2.2}$$

where θ is the soil moisture at depth z, θ_r and θ_s are the residual and saturation moisture contents, N_{wt} is the depth to water table, Ψ_b is the air entry bubbling pressure and λ_o is the pore-size distribution index. Ivanov *et al.* (2003a) have recently documented the unsaturated zone dynamics and its interaction with a time-varying water table position.

Coupled to the vertical dynamics is the lateral moisture redistribution through fluxes in the vadose zone and aquifer. Moisture fluxes driven by gradients in the surface and groundwater topography are essential for determining locations of surface saturation (*e.g.*, O'Loughlin, 1986, Western *et al.,* 1999). In the unsaturated zone, the horizontal flow component between contiguous elements is computed over the saturated wedge and along the steepest direction (Ivanov *et al.*, 2003). In the shallow aquifer, a quasi-three dimensional model based on the Dupuit-Forchheimer approximation to porous media flow (Freeze and Cherry, 1979) distributes moisture from recharge areas in the basin to discharge locations along drainage lines. Lateral exchanges between elements are controlled by the hydraulic gradient as (Ivanov *et al.*, 2003):

$$Q_S = -Tw \tan \beta_w, \tag{2.3}$$

where Q_S is the groundwater outflux, w is the flow width, tan β_w is the local water table slope and T is the depth averaged aquifer transmissivity:

$$T = \frac{a_r K_{on}}{f}\left(\exp(-fN_{wt}) - \exp(-fD)\right), \tag{2.4}$$

obtained from the position of the water table (N_{wt}), depth to the bedrock layer (D), surface normal conductivity (K_{on}), conductivity decay (f), and anisotropy ratio ($a_r = K_{op} / K_{on}$). Water table dynamics are computed from the groundwater influx and outflux, as well as the vertical recharge from the unsaturated moisture fronts. Ivanov *et al.* (2003a) details the groundwater dynamics and its role in redistributing moisture. Overall, the position of the water table anchors the soil moisture profile throughout the watershed and effectively determines the regions of saturation prior to a storm event (*e.g.*, Garrote and Bras, 1995).

2.2.3 Runoff generation

The coupled nature of the unsaturated and saturated processes in tRIBS results in a robust set of mechanisms for the generation of runoff at each element. Four basic runoff types are distinguished through interactions of rainfall with the dynamic moisture waves and water table position: infiltration-excess runoff (R_I) (Horton, 1933), saturation-excess runoff (R_S) (Dunne and Black, 1970), groundwater exfiltration or baseflow (R_G) (Hursh and Brater, 1941), and perched return flow (R_P) (Weyman, 1970). Total runoff (R) is composed of the four production mechanisms:

$$R = R_I + R_S + R_P + R_G, \tag{2.5}$$

where R_I+R_S and R_P+R_G are the surface and subsurface flow components, respectively. Ivanov *et al.* (2003a) details the dynamic states in the coupled system leading to the production of each mechanism. Over complex terrain, runoff occurrence and frequency

depends on the spatio-temporal characteristics of catchment topography, soils, climate, rainfall and antecedent wetness (*e.g.*, Beven, 2000). Given this variability, it is recognized that basin response can correspond to runoff production from multiple mechanisms arranged in spatially distinct areas or possibly to a single dominant type over the entire basin. The conditions leading to simultaneous or preferred runoff will vary considerably with the factors influencing the coupled unsaturated-saturated dynamics.

2.2.4 Surface energy balance and evapotranspiration

At the land surface, the soil moisture state resulting from the interaction of infiltration, runoff and lateral subsurface flows is coupled to the vertical moisture loss from atmospheric demand. The surface energy balance, $R_n - G = \lambda E + H$, is solved at the soil surface as function of surface temperature using parameterizations for net radiation (R_n), latent heat flux (λE), sensible heat flux (H), and ground heat flux (G) fully described in Ivanov *et al.* (2003a). The actual evaporation (E_a) computed from the latent heat flux is subsequently utilized to determine evaporation from moist bare soil (E_s), a wet plant canopy due to rain interception (E_{wc}), and plant transpiration from a dry canopy (E_{dc}) (*e.g.*, Wigmosta *et al.*, 1994). Total evapotranspiration (ET) is determined by soils and vegetation parameters that include vegetative cover (v), surface albedo (a), canopy height (h), stomatal resistance (r_s) and optical coefficient (K_t), in addition to meteorological conditions and solar radiation forcing. Moisture in the top surface layer, root zone and canopy storage play a key role in limiting ET when the atmospheric demand is high. Conversely, surface moisture extraction due to evapotranspiration can impact the unsaturated-saturated dynamics and lead to differences in runoff production.

2.2.5 Hillslope and channel flow routing

Runoff generated from the multiple mechanisms at each element within the complex domain is routed across an individual hillslope overland flow path and subsequently through the channel network. The hillslope drainage network is defined over the edges of the triangular facets that connect a TIN node to the closest downstream stream node (Tucker *et al.,* 2001a, Ivanov *et al.*, 2003a). A nonlinear velocity-discharge relation is used to determine the velocity over a hillslope path (Garrote and Bras, 1995):

$$v_h = c_v \left(\frac{Q}{A_h} \right)^r , \tag{2.6}$$

where v_h is the time-varying hillslope velocity, A_h is the hillslope contributing area, Q is the discharge at the downstream channel node, and r and c_v are uniform parameters of the non-linear relation. Thus, overland travel time is a function of stream discharge and hillslope path length. Overland flow from multiple hillslope nodes serves as lateral inflow into a kinematic wave, one-dimensional channel routing scheme solved over the drainage network. Channel travel time depends on the discharge (Q) which for a wide, rectangular channel can be expressed for each network link as (*e.g.*, Chaudry, 1993):

$$Q = \frac{1}{n} S^{1/2} H^{5/3} b , \tag{2.7}$$

where n is the Manning roughness coefficient, S is the channel slope, b is the channel width, and H is the time-varying water depth. As travel time is faster through streams than groundwater flow paths, the runoff partitioning into overland flow and subsurface flow is critical for determining the degree of basin retardation of rainfall forcing.

2.3 Hydrologic model calibration and verification

Model calibration was accomplished through a manual procedure that adjusts soil, vegetation and routing parameters to match the observed hydrograph at the basin outlet for a sequence of storm and interstorm periods. The multi-step calibration procedure, fully described in Ivanov *et al.* (2003b), ensures that the model performance is reliable at the element, hillslope and catchment scales. Initial parameter estimates were based on established physical relationships to soils and vegetation types (*e.g.*, Rawls *et al.*, 1982, Bras, 1990). The calibration is focused by tuning a limited number of parameters to which the model is most sensitive within narrow, physically plausible ranges (Ivanov *et al.*, 2003b). In addition, the spatial variability of parameter values is taken into account through a limited set of soil and vegetation classes. The calibration is further constrained by not permitting within-class parameter variability. In this manner, the potential for over-parameterization of the model is reduced and the overall strengths of the distributed approach, capturing spatial variability in catchment characteristics, are highlighted.

Calibration parameters utilized in this study were derived from a modeling effort in the Baron Fork reported by Ivanov *et al.* (2003b). Several flood events over the 1993 to 1999 period were selected to adjust flow volume and baseflow recession using the soil hydraulic parameters (K_{on}, f, a_r) controlling infiltration and subsurface flow. Hydrograph peak and timing were modified through the overland and channel parameters (c_v, r, n, b). Interstorm periods were simulated to fine-tune the surface energy and evapotranspiration parameters (K_t, r_s, v) leading to losses from the soil moisture profile and saturated areas. Finally, a number of storm events with different runoff responses were used to compare the relative magnitudes of the runoff types. Runoff production was related to antecedent

Parameter	Units	Soil and Land Cover Classification		
		Forest	*Grassland*	*Urban*
Soils Properties				
K_s	[mm/hr]	35	2.8	0.5
θ_s	[–]	0.4	0.3	0.3
θ_r	[–]	0.05	0.05	0.05
λ_o	[–]	0.3	0.25	0.2
ψ_b	[mm]	-100	-200	-400
f	[mm^{-1}]	0.0009	0.0004	0.0007
a_r	[–]	400	400	200
Vegetation Properties				
a	[–]	0.16	0.2	0.13
h	[m]	12	0.7	0.1
K_t	[–]	0.8	0.9	0.8
r_s	[s/m]	60	40	100
v	[–]	0.6	0.65	0.1
Channel Properties				
c_v	[–]	Spatially-uniform, 70		
r	[–]	Spatially-uniform, 0.4		
n	[–]	Spatially-uniform, 0.2		
b	[m]	Spatially-variable, 35 m at outlet		

Table 2.2. Model parameters obtained from multiple year calibration and verification procedure detailed in Ivanov *et al.* (2003b).

conditions, rain variability and seasonality to ensure model consistency. Table 2.2 presents the set of calibrated model parameters for the Baron Fork used in this study.

Ivanov *et al.* (2003a, 2003b) present a detailed analysis of the model performance in the Baron Fork during a continuous simulation (1993 to 2000) in terms of discharge at the gauging stations and the distribution of hydrologic states over the basins. NEXRAD rainfall data and weather data from Maurer *et al.* (2002) were utilized to force the model over separate calibration and verification periods (Smith *et al.*, 2003). Results indicate that model simulations capture the nested flood response and the observed nonlinearities in the rainfall-runoff transformation through multiple runoff generation mechanisms. Spatial distributions of runoff production also demonstrated the topographic, soils and

vegetation control on basin response. Overall confidence in the model for this basin is high given the multi-year application with complex radar rainfall forcing.

References

Abbott, M. B., J. C. Bathurst, J. A. Cunge, P. E. O'Connell, and J. Rasmussen. 1986. An introduction to the European Hydrological System - *Systeme Hydrologique European*, 'SHE', 1: History and philosophy of a physically-based distributed modelling system. *Journal of Hydrology*. 87, 45-59.

Beven, K. J. 1982. On subsurface stormflow: An analysis of response times. *Hydrological Sciences Journal*. 27, 505-521.

Beven, K.J., and M. J. Kirkby. 1979. A physically-based variable contributing area model of basin hydrology. *Hydrological Sciences Bulletin*. 24, 43-69.

Beven, K. J. 2000. *Rainfall-runoff Modelling: the Primer*. Wiley, Chichister, UK.

Bras, R. L. 1990. *Hydrology: An Introduction to Hydrologic Science*. Addison-Wesley Longman, Reading, MA.

Brooks, R. H., and A. T. Corey. 1964. Hydraulic properties of porous media. *Hydrology Paper 3*, Colorado State. Univ., Fort Collins.

Cabral, M. C., L. Garrote, R. L. Bras, and D. Entekhabi. 1992. A kinematic model of infiltration and runoff generation in layered and sloped soils. *Advances in Water Resources*. 15, 311-324.

Chaudry, M. H., 1993. *Open channel flow*. Prentice Hall, New Jersey.

de Vries, J. J. 1995. Seasonal expansion and contraction of stream networks in shallow groundwater systems. *Journal of Hydrology*. 170, 15-26.

Dunne, T., and R. D. Black. 1970. An experimental investigation of runoff production in permeable soils. *Water Resources Research*. 6(2), 478-490.

Freeze, R. A., and J. A. Cherry. 1979. *Groundwater*. Prentice Hall, Englwood Cliffs, NJ.

Garrote, L., and R. L. Bras. 1995. A distributed model for real-time flood forecasting using digital elevation models. *Journal of Hydrology*. 167, 279-306.

Horton, R. E. 1933. The role of infiltration in the hydrological cycle. *Trans. AGU*. 14, 446-460.

Hursh, C. R., and E. F. Brater. 1941. Separating storm-hydrographs form small drainage-areas into surface and subsurface flow. *Trans. AGU*. 22, 863-870.

Ivanov, V. Y. 2002. *A continuous Real-time Interactive Basin Simulator (RIBS)*. M.S. thesis, MIT, Cambridge, MA.

Ivanov, V.Y., Vivoni, E.R., Bras, R.L. and Entekhabi, D. 2003a. Development of a TIN-based distributed hydrologic model for real-time, continuous forecasting. Submitted to *Water Resources Research*.

Ivanov, V.Y., Vivoni, E.R., Bras, R.L. and Entekhabi, D. 2003b. Preserving high-resolution surface and rainfall data in operational-scale basin hydrology: A fully-distributed, physically-based approach. Submitted to *Journal of Hydrology*.

Lancaster, S.T. and Bras, R.L. 2002. A simple model of river meandering and its comparison to natural channels. *Hydrological Processes*. 16(1), 1-26.

Maurer, E. P., A. W. Wood, J. C. Adam, D. P. Lettenmaier, and B. Nijssen. 2002. A long-term hydrologically-based data set of land surface fluxes and states for the conterminous United States. *Journal of Climate*. 15, 3237-3251.

Miller, E. E., and R. D. Miller. 1956. Physical theory for capillary flow phenomena. *Journal of Applied Physics*. 27(4).

O'Loughlin, E. M. 1986. Prediction of surface saturated zones in natural catchments by topographic analysis. *Water Resources Research*. 22(5), 794-804.

Rawls, W.J., D. L. Brakensiek, and K. E. Saxton. 1982. Estimation of soil water properties. *Trans. ASAE*. 25(5), 1316-1330.

Smith, M., Seo, D.-J., Koren, V., Reed, S., Zhang, Z., and F. Moreda. 2003. The Distributed Model Intercomparison Project (DMIP): An overview. Submitted to *Journal of Hydrology*.

Teles, V., Capolongo, D. and Bras, R.L. 2002. A physically-based model for rainfall-triggered landslides at a regional scale. *Geophysical Research abstracts, European Geophysical Society annual congress, Nice 2002*. EGS02-A-03808.

Teles, V. and Bras, R.L. 2002. *Comparative soil erosion model protocol: CHILD model preliminary results*. USACERL unpublished report. Ralph M. Parsons Laboratory, Massachusetts Institute of Technology, Cambridge, MA.

Tucker, G.E., Lancaster, S.T., Gasparini, N.M., Bras, R.L. and Rybarczyk, S.M. 2001a. An object-oriented framework for distributed hydrologic and geomorphologic modeling using triangulated irregular networks. *Computers & Geosciences*. 27(8), 959-973.

Tucker, G.E., Lancaster, S.T., Gasparini, N.M. and Bras, R.L. 2001b. The Channel-Hillslope Integrated Landscape Development (CHILD) model. In *Landscape Erosion and Evolution Modelling*, ed. R.S. Harmon and W. Doe. Kluwer Academic/Plenum Publishers. Dordrecht. 349-388.

Vivoni, E.R., Ivanov, V.Y., Bras, R.L. and Entekhabi, D. 2002. Topography, triangular irregular networks and hydrological similarity. Submitted to *Journal of Hydrologic Engineering*.

Western, A. W., R. B. Grayson, G. Blöschl, G. R. Willgoose, and T. A. McMahon,. 1999. Observed spatial organization of soil moisture and its relation to terrain indices. *Water Resources Research*. 35(3), 797- 810.

Weyman, D. R. 1970. Throughflow on hillslopes and its relation to the stream hydrograph. *Hydrological Sciences Bulletin*. 15, 25-33.

Wigmosta, M. S., L.W. Vail, and D. P. Lettenmaeir. 1994. A distributed hydrology-vegetation model for complex terrain. *Water Resources Research*. 30(6), 1665-1679.

Willgoose, G., Bras, R.L., Rodríguez-Iturbe, I. 1991. A physical explanation of an observed link area-slope relationship. *Water Resources Research*. 27(7): 1697-1702.

Chapter 3:

Embedding Landscape Processes into Triangulated Terrain Models: Impacts on Dynamic Model Responses

3.1 Introduction

Geographic information systems (GIS) provide a framework for analyzing the spatial and temporal variability of surface processes. In most hydrogeomorphic or 'landscape' models, digital terrain forms the basis of the computational domain due to the topographic control on system behavior. Thus, advances in three-dimensional terrain representation are directly applicable and significant to the formulation of process-based, distributed models. Although raster-grids are the most common approach, triangulated irregular networks (TINs) are an attractive alternative for deriving multiple-resolution terrain (*e.g.*, Vivoni *et al.*, 2002). Among other advantages, TINs provide a flexible data structure that permits an adaptive model representation with variable node density.

Distributed landscape models capture the transient behavior in runoff production and sediment transport by solving equations describing hydrogeomorphic processes over a computational domain (*e.g.*, Montgomery and Dietrich, 1994; Wilson and Gallant, 1996; Tucker *et al.*, 2001b). Terrain surface representation is a function of the data structure and varies with the prescribed resolution. The selection of terrain resolution is typically the result of a tradeoff between available computational resources and the acceptable errors in model predictions (*e.g.*, Zhang and Montgomery, 1994; Walker and Willgoose, 1999). For a given data structure, the features of the model dynamics are rarely taken into account when selecting an appropriate model resolution.

In this chapter, we present a new approach that uses a multiple resolution TIN to resolve critical domain areas that are believed to have the highest potential impact on the transient model behavior. The new method also provides a consistent means for initializing distributed models by embedding process behavior directly into the computational domain. We demonstrate the advantages of the new model initialization using the Channel-Hillslope Integrated Landscape Development (CHILD) (Tucker *et al.*, 2001b) and the TIN-based Real-time Integrated Basin Simulator (tRIBS) (Ivanov *et al.*, 2003) models. The GIS methodology is illustrated in three applications: (1) saturation-excess runoff, (2) transport-limited erosion and (3) rainfall-triggered shallow landsliding.

This chapter is organized as follows. Section 3.2 describes the use of steady-state indices for hydrogeomorphic modeling. In section 3.3, the method for process-constrained triangulation is described. Finally, section 3.4 highlights the performance of the new method in transient simulations relative to traditional mesh representations. In the following, we illustrate the advantages of index-based triangulation through model simulation comparisons as a first step to addressing the topic through field measurements of distributed hydrogeomorphic response.

3.2 Steady-state landscape indices

Recognizing the importance of terrain attributes on the prediction of hydrogeomorphic processes has led to the development and testing of various landscape indices. A landscape index is intended to compactly represent the spatial variation of process behavior by isolating the dominant terrain factors. Steady-state indices also permit a distribution function approach to modeling complex phenomena. Typically, a combination of topographic and landscape attributes is used to define a single metric

capable of classifying the entire domain into distinct response classes. A complex landscape is subsequently divided into regions with similar *a priori* process behavior.

3.2.1 Saturation-excess runoff

Terrain analysis from digital elevation models (DEMs) forms the basis for developing steady-state landscape indices. Beven and Kirkby (1979) and O'Loughlin (1986) introduced the topographic or wetness index as a means for describing runoff produced in saturated areas. The index combines the effect of specific basin area (a) and slope angle (β) in a log-transformed metric (λ):

$$\lambda = \ln(a/\tan\beta), \tag{3.1}$$

capable of discerning between convergent and divergent flow regions. The index is intended to represent the topographic control on soil wetness during steady-state conditions. The assumptions used to derive (3.1) are discussed in Beven and Kirkby (1979) and reviewed in Beven *et al.* (1995). Expansion of the index to include non-steady state conditions through a time-variable contributing area has been proposed by Barling *et al.* (1994). For DEMs, the specific catchment area is computed using a recursive equation (*e.g.*, Rodríguez-Iturbe and Rinaldo, 1997; Tucker *et al.*, 2001c):

$$a = \frac{A_i}{b} = \frac{1}{b}\left(\sum_j w_{i,j} A_j + A_c\right), \tag{3.2}$$

where A_i is the contributing area at the ith cell, b is the DEM cell length, $w_{i,j}$ specifies the element connectivity ($w_{i,j} = 1$, if i, j connected, $w_{i,j} = 0$ otherwise) and A_c is the cell area. The slope angle is computed by fitting a nine-term polynomial to a 3x3 neighborhood for each cell, as described in Moore *et al.* (1991).

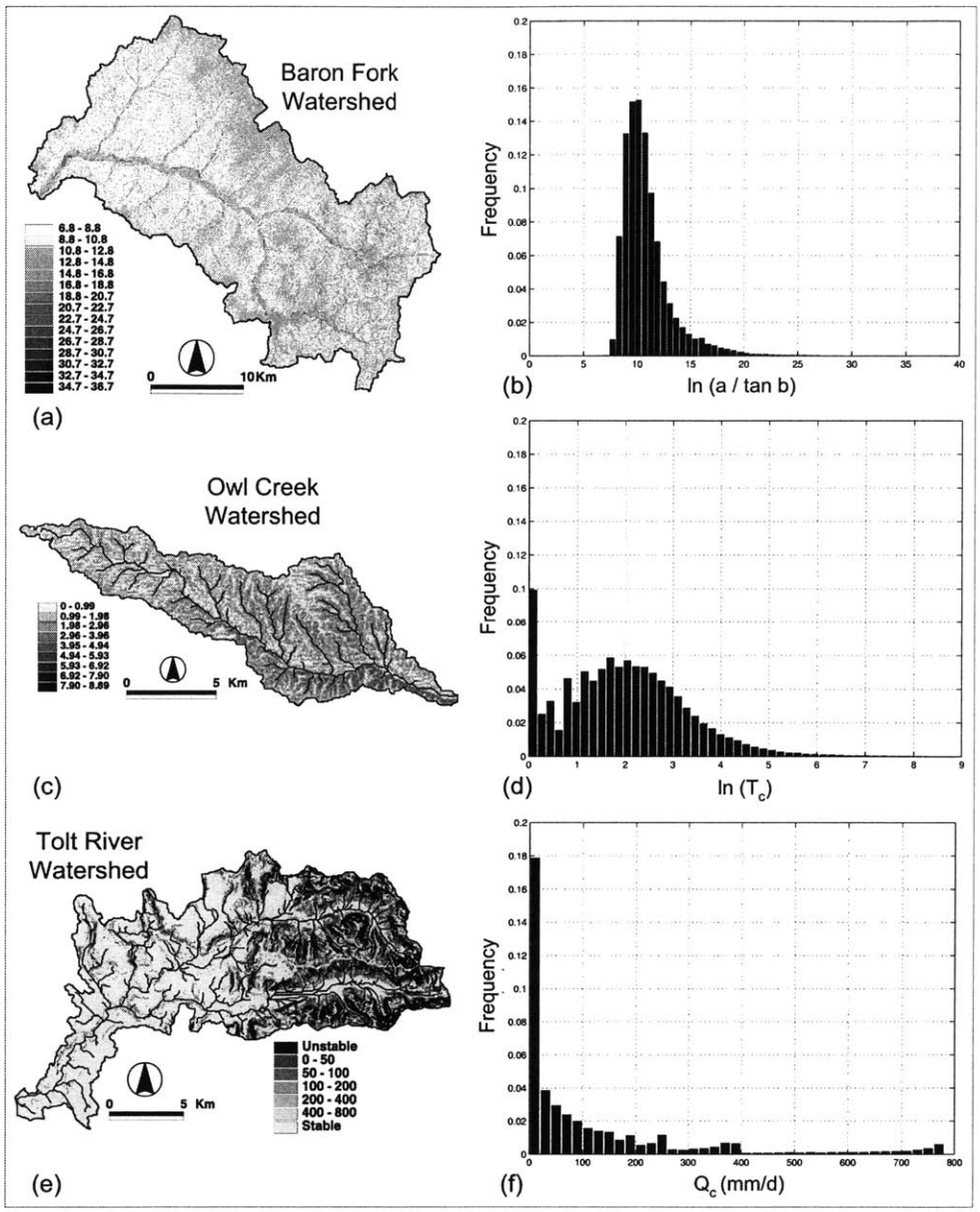

Figure 3.1. Steady-state landscape indices. (a) Spatial distribution of λ for the Baron Fork watershed (808 km^2) from 30-m USGS DEM. (b) Probability density function of λ. (c) Spatial distribution of ln(T_c) for the Owl Creek basin (100 km^2) from 30-m USGS DEM. (d) Probability density function of ln(T_c). (e) Spatial distribution of Q_c for the Tolt River basin (250 km^2) from 26-m SRTM DEM. (f) Probability density function of Q_c.

In Figure 3.1a, the spatially distributed wetness index is presented for the Baron Fork basin in northeastern Oklahoma. The index has high values in convergent areas with high contributing area and low slope, while low values are depicted in high slope, upland

regions. Given a range of possible λ values over a landscape, the distribution function of the wetness index is used to classify regions with similar hydrologic response. Landscape elements within each λ class will respond similarly to incident rainfall, producing runoff according to the steady-state element wetness (Figure 3.1b, Beven and Kirkby, 1979).

3.2.2 Transport-limited sediment erosion

Specific catchment area and slope are also used to characterize landscape geomorphology, where the slope-area relationship provides a fundamental measure of fluvial processes (*e.g.*, Tarboton *et al.*, 1989; Willgoose *et al.*, 1991; Rodríguez-Iturbe and Rinaldo, 1997). Overland erosion and sediment transport can be parameterized by a landscape index using either a stream power or shear stress approach (*e.g.*, Moore and Burch, 1986; Tucker *et al.*, 2001a,b). One measure for erosion utilizes slope angle (β) and area (a) to predict transport-limited rill or sheet flow as (Moore and Wilson, 1992):

$$T_c = \left(\frac{a}{22.13}\right)^m \left(\frac{\sin\beta}{0.0896}\right)^n, \tag{3.3}$$

where T_c is the dimensionless transport index, m = 0.56 or 0.9, n = 1.22 or 1.05 for rill and sheet erosion, respectively. This index is analogous to the length-slope (LS) factor in the RUSLE model (Renard *et al.*, 1991) adapted to three-dimensional terrain (Moore and Wilson, 1992). Though limited to net erosion, (3.3) can be used to classify landscapes according to a steady-state erosive hazard. Similar indices incorporating erosion and deposition have recently been implemented in a GIS by Mitasova *et al.* (1996).

Figure 3.1c illustrates the sediment transport capacity index for the Owl Creek basin in central Texas. Catchment areas with similar T_c values are considered to have equal erosion potential under equilibrium conditions. Due to the large range of a values

in mid-to-large basins, the log-transform of T_c is a useful operation on the distribution function (Figure 3.1d). Similarity in the erosion process is assumed within areas of high $\ln(T_c)$ values near large topographic gradients (large β) or within areas of low T_c values in flatter terrain (small β). Given that $n > m$ in (3.3), sediment erosion potential depends strongly on terrain slope. A distributed landscape model predicting sheet or rill erosion due to overland flow should preferentially resolve areas with high erosion potential.

3.2.3 Rainfall-triggered shallow landslides

Topographic control on geomorphological processes has also been used for the prediction of landslide hazards. Montgomery and Dietrich (1994) proposed a shallow landsliding model that incorporates the wetness index and an infinite slope stability model. For cohensionless soil, the critical steady-state rainfall (Q_c) required to trigger shallow landslides is expressed as:

$$Q_c = \frac{T \sin\beta}{a}\left[\frac{\rho_s}{\rho_w}\left(1-\frac{\tan\beta}{\tan\phi}\right)\right], \tag{3.4}$$

where T is saturated transmissivity, ρ_s is the soil bulk density, ρ_w is density of water and ϕ is the soil friction angle. The critical rainfall predicted to cause instability can be used as a measure of landslide hazard. Similarity in landscape response to Q_c classifies elements with equal landslide initiation potential given a steady rainfall rate. Montgomery *et al.* (1998) also provide criteria for unconditional stability and instability given a cohesive or cohensionless soil. For transient climatic conditions, Borga *et al.* (2002) has recently used the quasi-steady state wetness index of Barling *et al.* (1994) for predicting rainfall-triggered landslide potential.

In Figure 3.1e, the shallow landslide distribution is shown for the Tolt River basin in central Washington. Landscape elements with low Q_c are prone to landslide triggering at low rainfall rates. Unconditionally stable and unstable elements are also predicted by (3.4) using the regional soil parameters (T, ρ_s, ϕ) in Montgomery *et al.* (1998). For transient landslide modeling, resolving only the critical, landslide-prone areas within a distributed domain could potentially lead to improved model accuracy and computational efficiency as compared to current methods (*e.g.*, Burton and Bathurst, 1998).

3.3 Process-constrained triangulation

Triangulated irregular networks offer several advantages over grid structures for distributed landscape modeling (Tucker *et al.*, 2001a). The primary advantage is the multiple resolutions offered by the irregularity of the mesh. Traditional TIN methods resolve regions with high terrain variability (*e.g.*, slope criterion), while reducing the number of elements in areas of low ruggedness (Lee, 1991). While this is appropriate for many GIS applications (*e.g.*, 3D analysis, visualization), distributed landscape models can benefit from a method that adapts TIN resolution to the landscape process of interest.

The proposed method for constraining a TIN model using a landscape index embeds the steady-state system behavior into the model representation. Instead of using a slope-preserving criterion, a landscape index classifies points according to their significance in describing a landscape process. For each distribution class, the method samples the DEM at a different resolution, retaining the highest detail in critical domain areas contributing to the steady-state behavior. Although only a few indices are presented here, the methodology is amenable to other similarity measures in hydrogeomorphic applications (*e.g.*, Moore *et al.*, 1993; Ambroise *et al.*, 1996; Woods *et al.*, 1997).

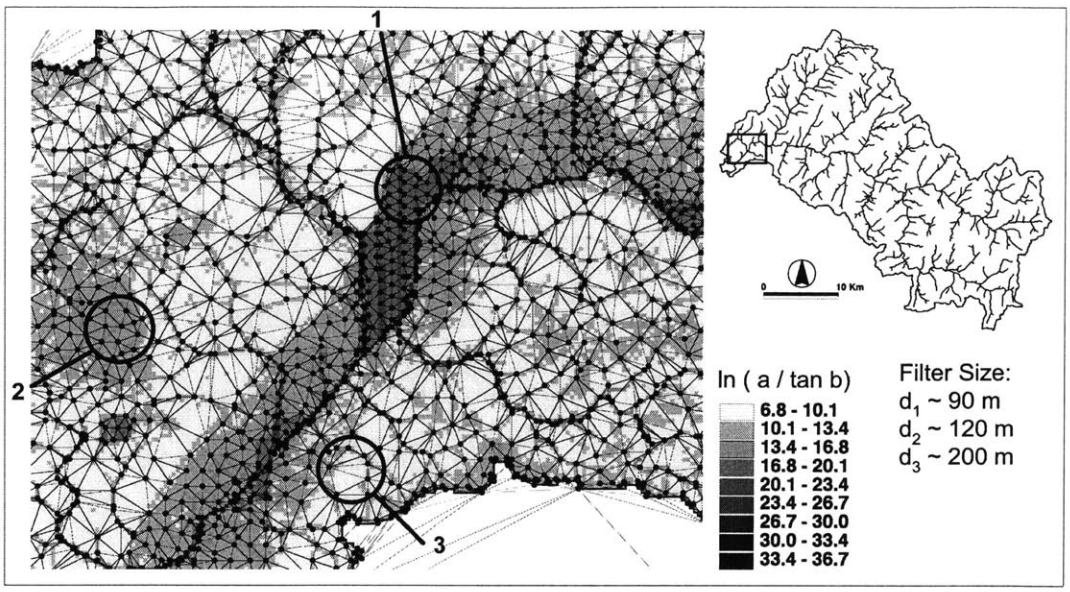

Figure 3.2. Example of a landscape process-constrained triangulation. The spatial distribution of λ is shown in gray-scale for the highlighted region in the Baron Fork. DEM point selection is based on a variable size filter (d_c). In the three circled areas, the filter varies in size from 90 to 200-meters (high to low λ).

To objectively select elevation nodes in index-based triangulation, a functional relationship is postulated between the mean index value (i_c) and mean point spacing (d_c):

$$d_c = f(i_c) \qquad r \le d_c \le l \qquad (3.5)$$

where f is a generic function relating the TIN resolution to the landscape index, l is the mean hillslope length and r is the DEM cell resolution. The mean point spacing is used as a proximity criterion to filter a high-resolution DEM (Figure 3.2). Physical limits on the filter size ensure that critical domain areas are sampled at a resolution proportional to r. Resolving the hillslope length for regions with low index value guarantees this natural landscape scale is preserved. The mean hillslope length is computed from the total stream length (L_T) and basin area (A):

$$l = \frac{1}{2D_d} = \frac{A}{2L_T}, \qquad (3.6)$$

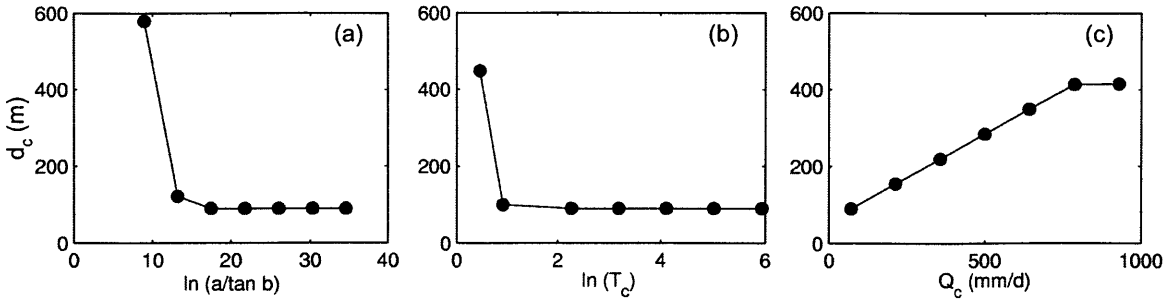

Figure 3.3. Functional relations between the mean index value and the mean point spacing (d_c) developed for the three hydrogeomorphic applications. (a) Hydrologic wetness index. (b) Sediment transport index. (c) Shallow landslide index.

where D_d is the drainage density, a key basin descriptor closely related to the long-term hydrogeomorphic response (*e.g.*, Tucker *et al.*, 2001c).

The functional relationship between the landscape index and the proximity filter can vary based on the index frequency distribution. For the wetness index, a *decreasing* filter size is appropriate such that higher resolution is retained in regions that saturate frequently. For simulating overland erosion, a *decreasing* relation is also appropriate for erosive regions ($\ln(T_c) > 0$). Where erosion is low, a filter size equal to the hillslope length is adequate. For landslide initiation, high resolution is desired for unstable regions under low rainfall, thus prompting an *increasing* filter size over the Q_c range. For unconditionally stable areas, the hillslope length is preserved. Figure 3.3 illustrates the proposed functional relations for the basins considered in Figure 3.1 and Table 3.1.

It is possible to generalize the methodology to derive (3.5) given the distribution function of a similarity index. Note the sharp change in the functional relation between the point spacing (d_c) and the index value (i_c) is prescribed to coincide with the peak in the distribution function (Figures 3.1, 3.3). In addition to the peak value, (3.5) also depends on which portions of the distribution are retained at high resolution. Classes to

Watershed	DEM	x_o [dd]	y_o [dd]	A [km^2]	n_g [#]	r [m]	l [m]
Baron Fork, OK	USGS	-94.84	35.92	808.15	897,944	30	579.22
Owl Creek, TX	USGS	-97.52	31.23	100.25	111,387	30	448.48
Tolt River, WA	SRTM	-121.92	47.64	249.55	372,012	25.9	414.52

Table 3.1. Study basin data. x_o and y_o are the outlet longitude and latitude, A is the basin area; n_g is the number of cells; r is the grid resolution and l is the mean hillslope length.

the right of the wetness index peak (ln (a/tan b) > 10), for example, should be represented at high resolution and are assigned decreasing values of d_c until a lower limit proportional to r is reached. A similar rule applies to the erosion index relation, where d_c sharply decreases for classes with values greater than the broad peak (ln (T_c) > 1-2). For the landslide index, however, lower values are retained such that classes to the right of the peak (Q_c = 0) are progressively filtered to a lower resolution (higher d_c) until a limit equal to l is reached. The absolute value of d_c in each class is chosen with respect to the DEM cell size, the hillslope length, and the number of frequency bins in the distribution.

After point selection, a tessellation is constructed enforcing the *constrained* Delaunay criterion (*e.g.*, Tsai, 1993). For a set of points, this criterion ensures that a circle passing through three points on any triangle contains no additional points. It also permits the inclusion of linear features such as stream networks and basin boundaries into a terrain model. During the triangulation procedure, the proximal filter is sequentially used to retain points as a function of the similarity index value. For index-based sampling, the variable-resolution TIN resembles the spatial distribution of the landscape process (Figure 3.2). The physical link between the multiple-resolution terrain model and the landscape parameters (*e.g.*, λ, T_c or Q_c and D_d) provides a consistent means for developing process-based TINs for any basin.

3.4 Illustrative Examples

We illustrate the use of steady-state landscape indices to construct process-based triangulations with three case studies. Table 3.1 lists the characteristics used to develop the landscape TINs for the Baron Fork, Owl Creek and Tolt River basins. The tRIBS and CHILD distributed models are used to evaluate the impact of terrain representation on hydrogeomorphic response. Both models explicitly represent the governing landscape processes by using a finite-volume approach on the TIN mesh (Tucker *et al.*, 2001b). The finite-volume or Voronoi polygon network is used to compute fluxes between elements, calculate mass balances and represent variability within a basin.

3.4.1 Basin runoff response and saturation

Distributed hydrologic models simulate the internal basin response to rainfall including the interstorm processes that evolve pre-storm soil moisture conditions. The delineation of surface-saturated zones is critical since these areas can produce high runoff intensities during storm events (*e.g.*, Beven and Kirkby, 1979). Accurate estimation of surface saturation depends on terrain resolution, particularly in near channel areas. The coarsening of model resolution in floodplains and riparian zones may have various effects on (1) stream and groundwater interactions, (2) lateral exchanges between model elements and (3) surface saturation and runoff production.

We test the impact of terrain representation by comparing the hydrologic response of the Baron Fork for the traditional and similarity-based (hydrologic) triangulations. Figure 3.4 highlights the differences in TIN resolution, each with the same number of nodes, such that 6.7% of the raster-DEM cells are retained. Differences in the TINs are dramatic in areas of low variability such as floodplains and the upper basin plateau. In

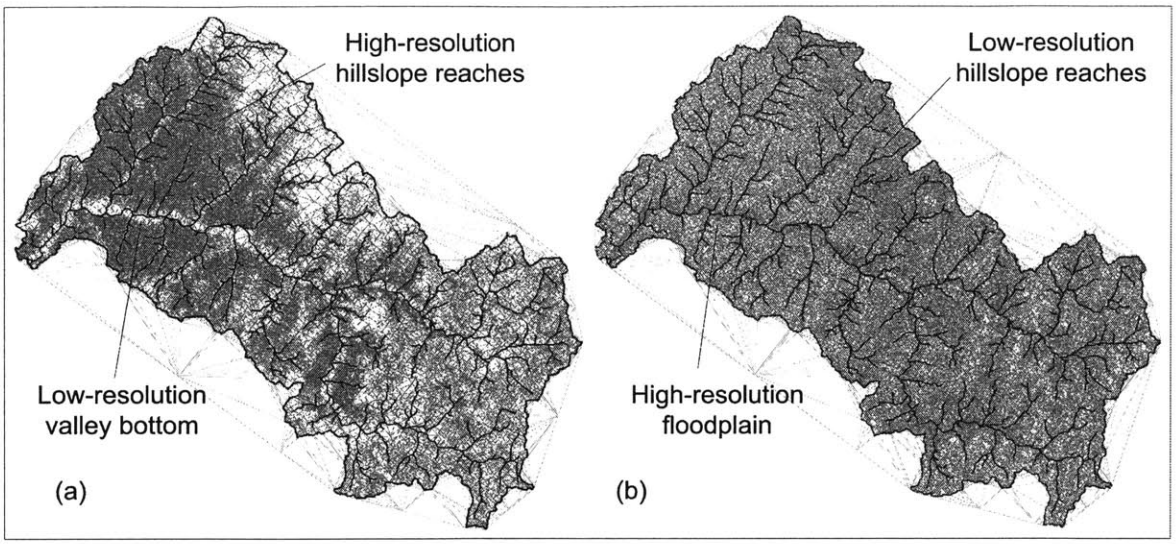

Figure 3.4. Triangulated irregular network representation of terrain for the Baron Fork watershed. (a) Traditional slope criteria method. (b) Hydrologic wetness index method.

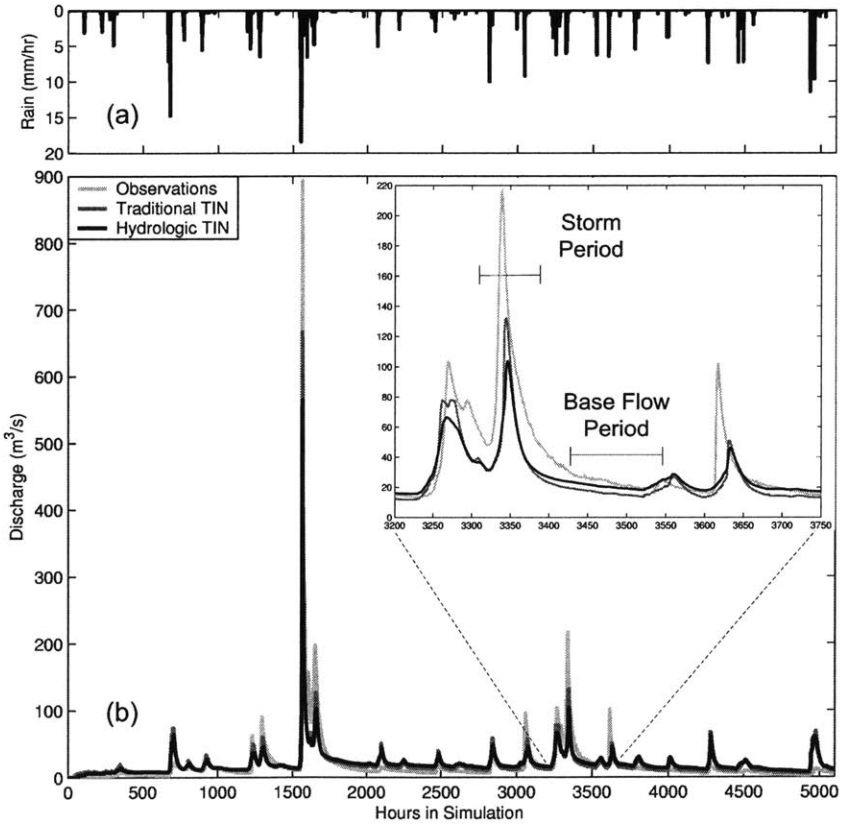

Figure 3.5. tRIBS hydrologic simulations over the seven month period (11/01/1997 to 05/31/1998) (a) Mean areal precipitation (mm/hr) from NEXRAD radar rainfall over the Baron Fork (b) Discharge observations (light gray) and model simulations for the traditional (dark gray) and hydrologic (black) TIN terrain representations.

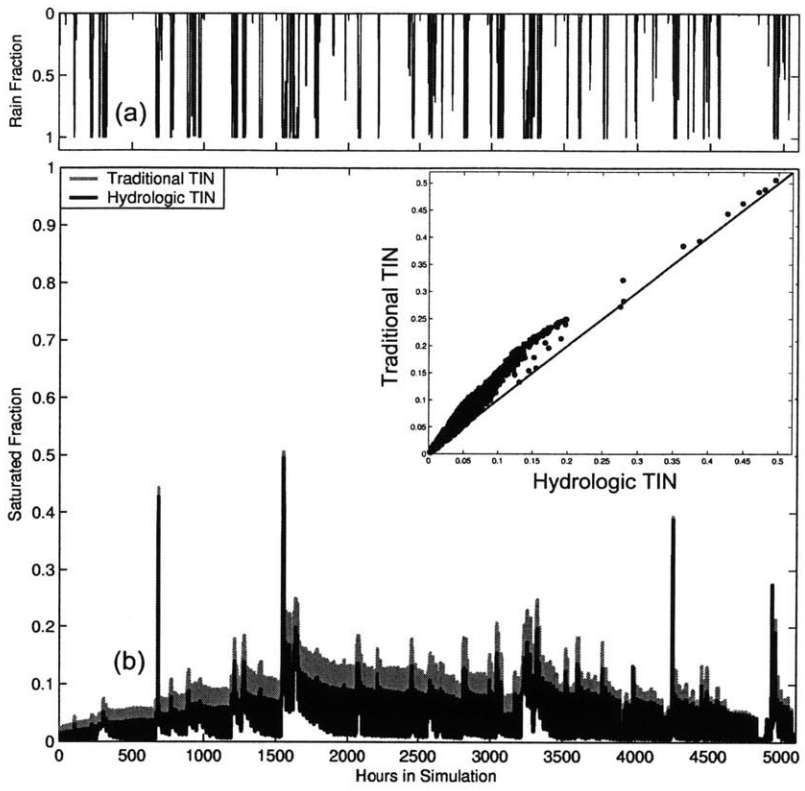

Figure 3.6. tRIBS distributed response for the Baron Fork simulations. (a) Fractional rainfall coverage in watershed over simulation period. (b) Saturated area fraction for the traditional (dark gray) and hydrologic (black) triangulated terrains. The inserted figure directly compares the saturated fraction for each method relative to a 1:1 line.

hillslopes where elevation variability is high, the traditional TIN captures changes in slope while the hydrologic TIN samples the region more evenly. Finally, the TIN element size distribution is quite different as quantified by the coefficient of variation of triangle area, $CV_A = 0.88$ and 2.06 for the hydrologic and traditional TINs, respectively.

The tRIBS model is applied for each TIN mesh for a seven month period during 1997-1998. Hourly rainfall observations from the NEXRAD radar network and surface weather data are used to force the model continuously. Model calibration was achieved using discharge observations at the Baron Fork (1996-2000) for a traditional TIN mesh (Ivanov *et al.*, 2003). In these simulations, a sequence of storms arrives at the basin,

producing hourly discharge ranging from 10 m^3/s (baseflow) to 900 m^3/s (peak storm). Figure 3.5 illustrates the observed basin-averaged rainfall, as well as the observed and simulated discharge for the triangulations. Model calibration was carried out for the traditional TIN which explains its closer agreement to discharge observations.

In Figure 3.5, the hydrologic TIN run exhibits higher baseflow and reduced peak flow as compared to the traditional TIN. These results are consistent with a higher proportion of groundwater exfiltration and a lower fraction of saturation-excess runoff for the hydrologic TIN (Table 3.2). This suggests that TIN representation can significantly influence the partitioning of incident rainfall into the possible runoff mechanisms in the tRIBS model. The spatial distribution of saturated areas and water table depth should reflect these marked differences in runoff production, as the unsaturated and saturated zones are strongly coupled within the model (see Ivanov *et al.*, 2003).

Figure 3.6 shows the surface-saturation dynamics during the simulation. Despite high fractional rainfall coverage (Figure 3.6a), the fraction of basin at saturation in the upper 10 cm (A_s) is dependent on large rainfall events and evaporation (Figure 3.6b). For low rainfall (A_s~0) and large storm events (A_s~0.5), the two triangulations produce similar results. For intermediate events ($0.05 \leq A_s \leq 0.25$) where saturation excess runoff is more important, the traditional TIN overestimates the saturated fraction relative to the predicted variable source area from the steady-state wetness index. This is consistent with a higher proportion of saturation-excess runoff during storm events for the traditional TIN (Table 3.2). Overestimation of the saturated areas results from poor resolution in regions where saturation dynamics are critical. Hydrologic TINs use the wetness index to address this issue by adding nodes where the dynamics are expected to be important.

Runoff Type	Traditional TIN	Hydrologic TIN
Infiltration-excess runoff	5.88	5.96
Saturation-excess runoff	27.00	18.94
Perched return flow	6.71	3.51
Groundwater exfiltration	60.41	71.58

Table 3.2. Percentage of total outlet discharge due to each runoff mechanism simulated in the tRIBS model for the Baron Fork runs.

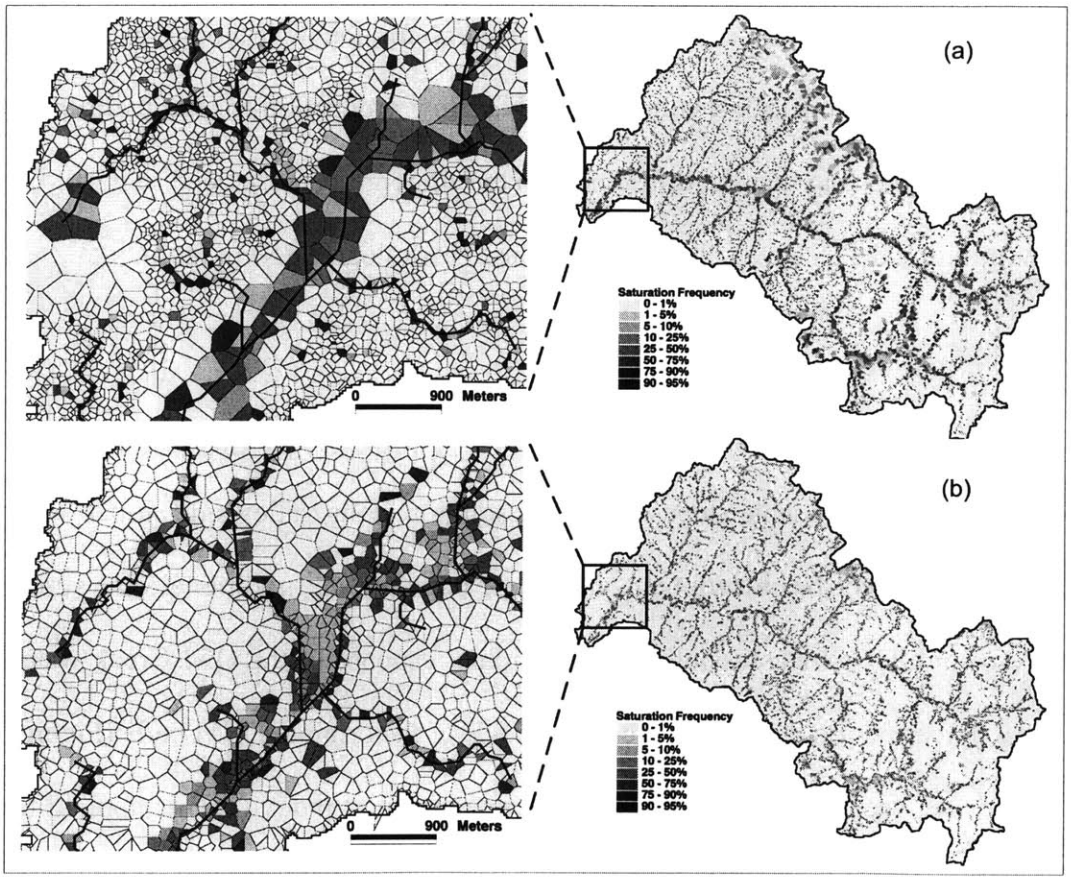

Figure 3.7. Spatial distribution of surface saturation frequency for the seven month simulation period represented as Voronoi polygons. Saturation frequency defined as the percentage of simulation time with surface saturated conditions. (a) Traditional slope criteria method. (b) Hydrologic wetness index method. The highlighted area shows the differences in surface saturation near the river confluence and along stream channels.

Differences in saturated area are further investigated by comparing the spatial distribution of saturation frequency. Figure 3.7 shows that the traditional TIN has a wetter watershed surface. Near channels, model coarseness leads to large elements that saturate frequently. Rainfall on these areas produces saturation-excess runoff leading to a rapid response and increased peak flow (Figure 3.5). The higher resolution provided by the hydrologic TIN reduces the saturated area. The water table position, however, is closer to the surface for the hydrologic TIN (not shown). At the end of the simulation, the mean water table depth is 3.38 and 4.19 meters for the hydrologic and traditional simulations. This is consistent with a higher baseflow production for the hydrologic TIN (Figure 3.5), suggesting that the differences in terrain representation lead to a shift from a surface (traditional TIN) to a subsurface response (hydrologic TIN) in the model.

3.4.2 Basin sediment yield

The simulation of sediment transport depends to a large extent on terrain resolution in highly erodable slopes. Coarse resolution along valley side slopes and steep hillslopes may affect basin sediment yield. We compare the traditional and similarity-based (erosion) TINs by assessing the geomorphic response of the Owl Creek watershed over a 14.5-year period. Each TIN mesh has 6.8% of the original DEM cells (Figure 3.8). Differences between the TINs are small since the transport index (3.3) is applied for rill erosion where slope is heavily weighted (n = 1.22, m = 0.56) and the criteria is shifted toward the traditional (slope-preserving) method. Nevertheless, the erosion TIN has a higher resolution along the fluvial network and a more even sampling in reaches with high erosion hazard. A comparison of element size confirms the similarity in the two TINs with CV_A = 1.17 for both triangulated models.

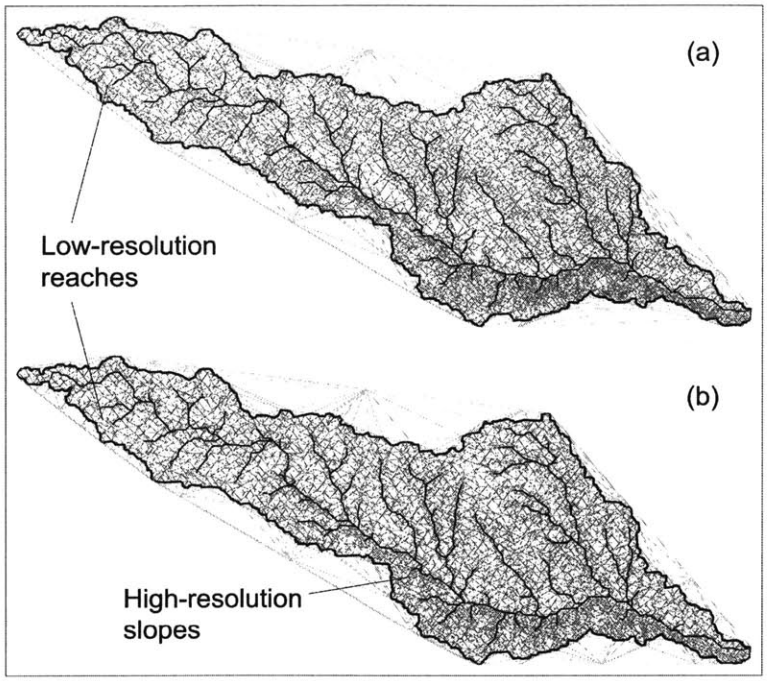

Figure 3.8. Triangulated irregular network representation of terrain for the Owl Creek basin. (a) Traditional slope criteria method. (b) Sediment transport index method.

Peak Erosion Volume (m^3)	Traditional TIN	Erosion TIN
≤ 0	77.17	81.94
0 – 25	14.05	9.57
25 – 50	6.60	5.79
50 – 100	1.91	2.36
100 – 150	0.17	0.31
150 – 200	0.07	0.03
>200	0.02	0.01

Table 3.3. Percentage of catchment area experiencing erosion (m^3) in a particular interval during the peak event for the Owl Creek CHILD simulations.

The CHILD model is applied for each TIN from 1986-2000 by using spatially-uniform rainfall from an hourly rain gauge located 40 km east of Owl Creek (Figure 3.9a). In these simulations, storms arriving at the basin produce sediment yields ranging from 5 to 6700 m^3 per 3 months for the erosion TIN and slightly higher values for traditional TIN (Figure 3.9b). Differences in erosion are more pronounced during peak

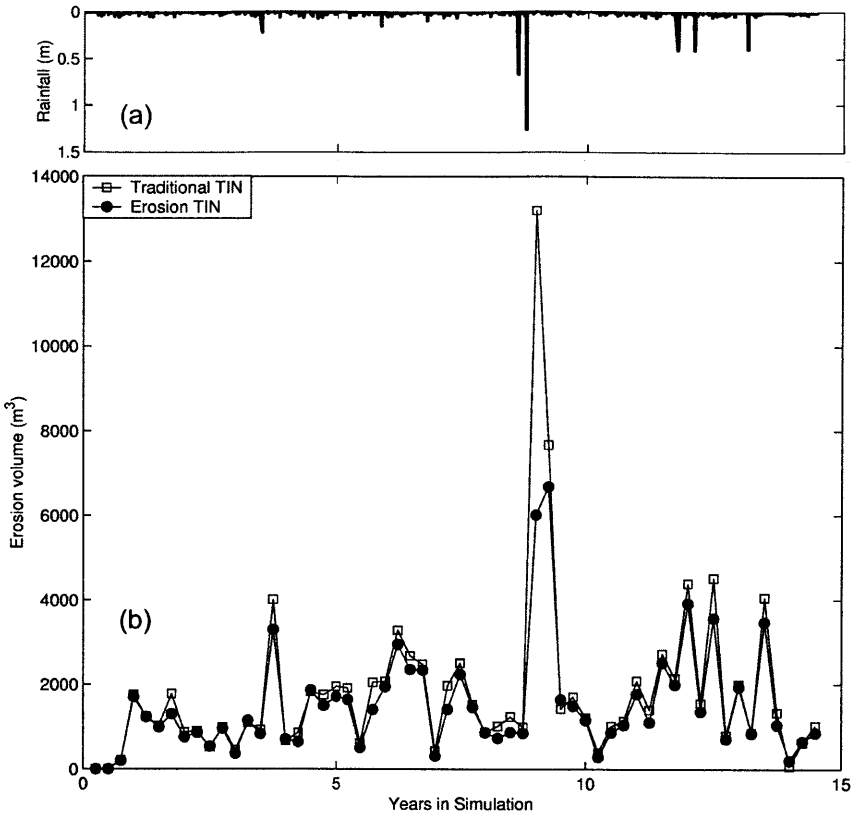

Figure 3.9. CHILD sediment transport over period 2/1/1986 to 6/30/2000. (a) Rain gauge forcing represented as a uniform depth for each storm (mm). (b) Erosion volume (m^3) per 3 months for the traditional (open square) and erosion (filled circle) triangulations.

events, due to a larger difference in eroded area for larger climatic events. In Table 3.3, we illustrate the basin fraction undergoing erosion at a particular rate during the major event in the simulation (11/1994 - 5/1995). While the erosion TIN has less total accreting area, there is a larger basin fraction contributing to moderate erosion rates in the range of 50–150 m^3 per 3 months. The larger percentage of area producing high erosion (>150 m^3) in the traditional TIN is consistent with higher sediment discharge (Figure 3.9).

Differences in erosion are further illustrated by comparing the spatial distribution of total erosion. Figure 3.10 shows that the traditional TIN experiences higher erosion along flat upslope areas whereas the erosion TIN is primarily eroded in the steep region

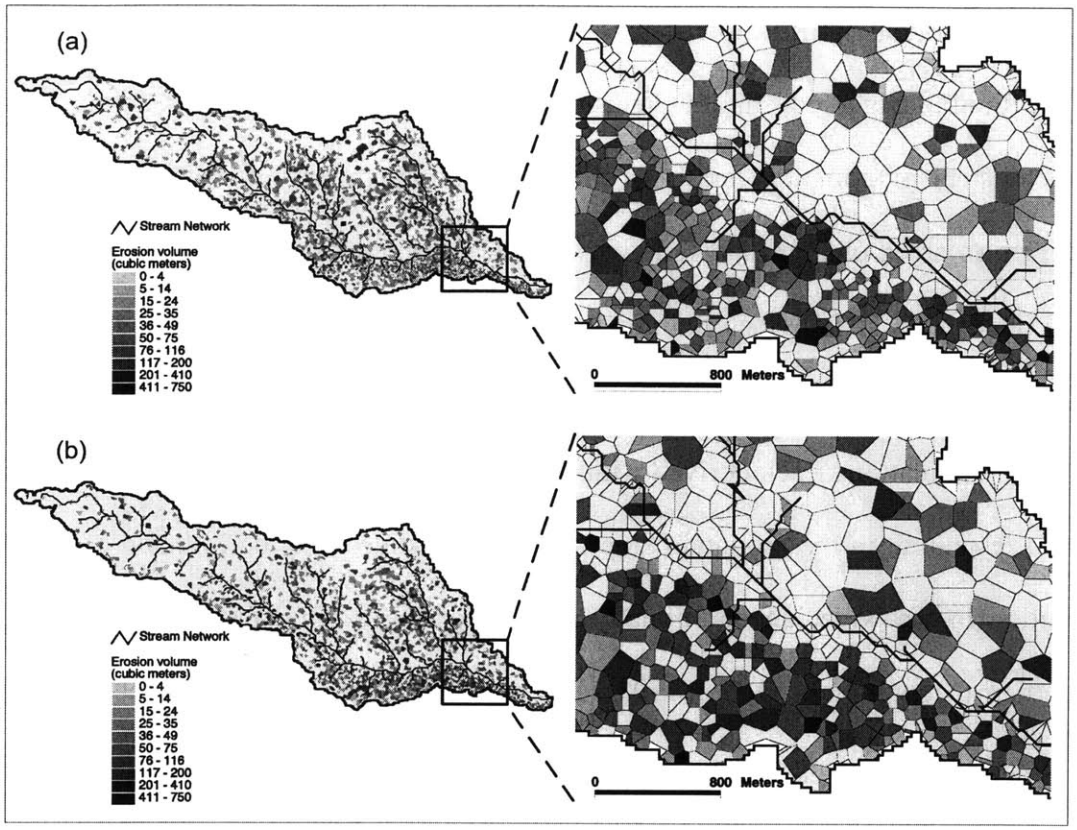

Figure 3.10. Spatial distribution of total erosion volume (m^3) over the simulation period. (a) Traditional slope criteria method. (b) Erosion or sediment transport index. The highlighted area shows the differences in erosion near areas of high (rugged slopes near bottom) and low (flat upland area near top) erosion hazard and along the stream network.

along the canyon wall. Near channels, the erosion TIN can differentiate between the valley slopes and bottom, thus producing more realistic erosion patterns. While the traditional TIN has higher peak erosion (Figure 3.9), the spatial distribution confirms that this is due to flat, upslope elements with a small basin area fraction (Table 3.3). In areas of high erosion hazard, the erosion TIN predicts increased erosion rates (Figure 3.10), suggesting that the similarity-based initialization shifts model behavior towards the prediction of the sediment transport index (Figure 3.1c).

3.4.3 Basin landslide initiation

Rainfall-triggered, shallow landslides are strongly controlled by the slope stability characteristics of complex terrain. Terrain resolution impacts the slope gradient and curvature in areas of high landslide hazard. We compare the traditional and similarity-based (landslide) TINs by determining the unstable regions in the Tolt River basin using a new landslide routine in the tRIBS model. Figure 3.11 presents the differences between the two triangulations, each derived with 6.1% of the DEM cells. The landslide TIN has a refined resolution in the mountain slopes where landslides may be initiated and a lower resolution in the wide, unconditionally stable, floodplain. Given spatially-uniform soil properties (Montgomery *et al.*, 1998) and rainfall forcing, tRIBS predicts regions of landslide initiation using a factor of safety (FS) approach with FS<1 implying instability (*e.g.*, Dietrich *et al.*, 1995, Selby, 1993).

Table 3.4 presents the percentage of unstable basin area for an applied rainfall ranging from 0 to 25 mm/hr. For low rainfall, the landslide TIN exhibits a smaller total unstable area than the traditional TIN. This is due to the better definition of the landslide prone areas along the steep mountain slopes. As rainfall is increased, however, the poor floodplain resolution leads to increased unstable areas on flat terrain, relative to the traditional TIN. For a steady-state rainfall of 1 mm/hr, the two triangulations have a nearly equal percentage of unstable areas, suggesting this value minimizes the tradeoff in resolution between hillslope and valley regions. This is corroborated in Figure 3.12, where the spatial distribution of the factor of safety is shown for the 1 mm/hr rainfall threshold. Along the landslide-prone slopes, the landslide TIN differentiates between stable and unstable model elements due to its higher resolution.

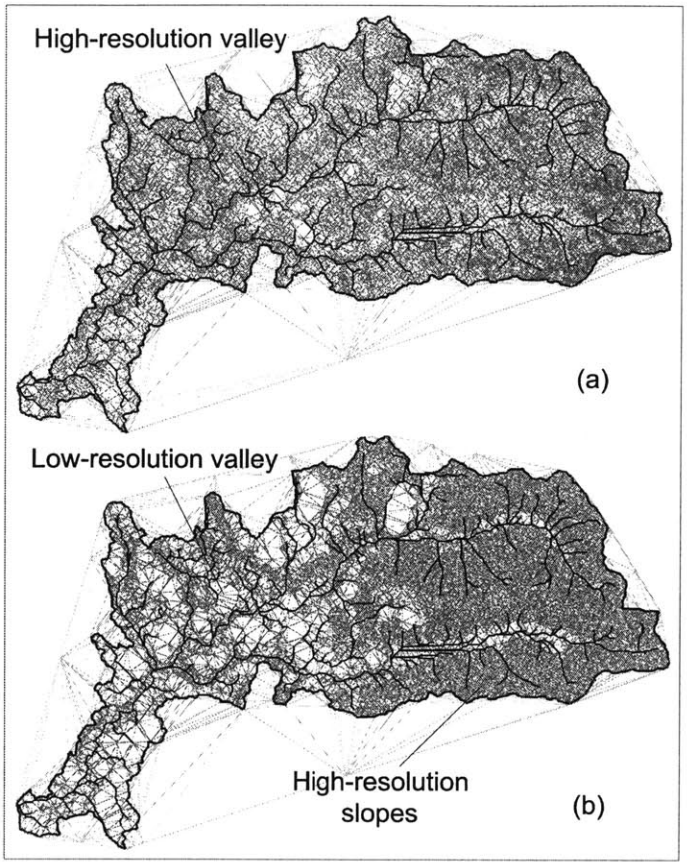

Figure 3.11. Triangulated irregular network representation of terrain for the Tolt River watershed. (a) Traditional slope criteria method. (b) Shallow landslide index method.

Rainfall threshold (mm/hr)	Traditional TIN	Landslide TIN
0	7.19	5.94
0.5	13.52	12.72
1	17.95	17.74
2.5	25.37	25.96
5	30.18	31.59
10	33.36	35.18
25	34.16	36.74

Table 3.4. Percentage of unstable catchment area for a particular rainfall threshold (mm/hr) in the Tolt River tRIBS simulations.

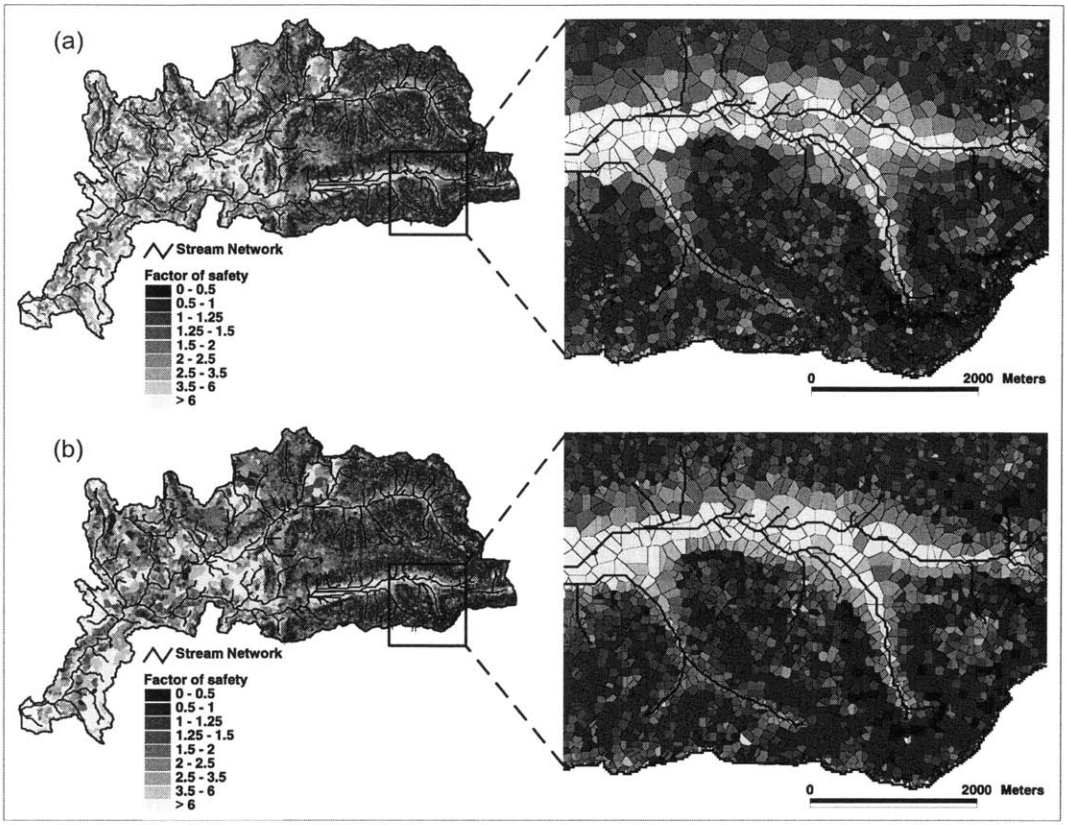

Figure 3.12. Spatial distribution of landslide instability for a rainfall threshold of 1 mm/hr. (a) Traditional slope criteria method. (b) Shallow landslide index method. The highlighted area shows the differences in the unstable regions near the mountain slopes and valley bottoms.

3.5 Discussion

The case studies presented in this work demonstrate the differences between the traditional method and proposed approach for embedding landscape processes into triangulated models. The spatial discretization improves upon traditional techniques by providing high resolution in regions anticipated to impact basin response, as predicted by a steady-state index. Utilizing the new methodology for the initialization of two physically-based, distributed models also leads to differences in the model response, shifting the transient behavior towards the process captured by the initialization index. In addition, the proposed triangulation selects model resolution objectively through a

physically-based constraint that can be tied to the distribution of model response. In the following, several issues regarding the potential for the similarity-based TIN methodology in the context of geographical information systems are discussed.

3.5.1 Physically-based terrain initialization

Landscape discretization is a topic of particular interest to models of land-surface processes. In general, determining the appropriate structural representation and resolution is often an arbitrary exercise. Most studies balance the tradeoff between the errors introduced through aggregation and the computational demands of a simulation (*e.g.*, Vazquez *et al.*, 2002). With regard to TIN-based models, studies have yet to develop objective techniques for selecting model resolution, relying solely on geometric criteria, such as abrupt slope changes, distance to boundaries and streams or fixed triangle area (*e.g.*, Palacios-Vélez *et al.*, 1998; Nelson *et al.*, 1999; Mita *et al.*, 2001).

The similarity approach provides a physically-based TIN terrain model tailored by the selection of a landscape index. Landscape indices are shown here to be objective criteria for embedding knowledge of process behavior into a terrain model. The method does not depend on specifying an arbitrary accuracy parameter (*e.g.*, Lee, 1991) but does rely on an appropriate relation between the index value and TIN resolution that is directly related to the index distribution function (Figure 3.3). Since landscape indices can be derived from topographic data at any resolution, these provide a consistent means for developing TINs across basin scales. More importantly, the model representation can be customized for the hydrogeomorphic application of interest. As shown in this chapter, the new approach can also lead to a shift in the transient model response towards the physical process represented by the landscape index.

3.5.2 Dynamic remeshing with transient indices

The similarity-based approach has focused on deriving an initial terrain surface for use within distributed hydrogeomorphic models. The steady-state index provides an approximation of the surface response to forcing given a particular process. The simulations built on the initial terrain then provide the transient model response which includes dynamic areas of saturation, erosion or landsliding. These, in turn, provide a mechanism for reevaluating the landscape index during a simulation. Barling *et al.* (1994) and Borga *et al.* (2002), for example, derived transient indices to account for the temporal variability of contributing area. In the context of similarity TINs, dynamic remeshing of the terrain model as a function of a transient index is an attractive possibility. CHILD, for example, has similar capabilities to deal with river meandering (Tucker *et al.*, 2001b). Dynamic remeshing could provide a physically-based, time-adaptive discretization.

3.5.3 Generalizing landscape indices for multi-purpose modeling

The concise representation of a landscape process afforded by an index is a means for approximating behavior directly from topography and related surface characteristics (*e.g.*, soils, vegetation). An important question is whether various landscape indices can be generalized by taking advantage of the common denominators in each relationship, primarily the contributing area (a) and surface slope (β) (see 3.1, 3.3 and 3.4). Given appropriate manipulation of the exponents (m and n), a single index could be derived to embed landscape behavior into TINs for multi-purpose modeling. The CHILD and tRIBS models could then be initialized with a generalized index conditioned on the dominant process. For a combined runoff and erosion model, an intermediate parameter set may be used to capture both processes in the initial representation of the deformable TIN mesh.

This may lead to a tradeoff between resolving each particular process and the overall goal of capturing multiple-process knowledge into the terrain model.

3.6 Conclusions

Distributed models constructed using TINs are yet to be ubiquitous tools in geographic information systems. Yet, the potential exists for constructing computationally efficient landscape models using GIS techniques developed for terrain visualization (*e.g.*, Cignoni *et al.*, 1997; Wu and Amaratunga, 2002). TINs provide a flexible framework in which multi-scale simulations can adapt to a level of detail or granularity commensurate with available data. In GIS, adding landscape processes to triangulated surfaces could transform current static models into dynamic three-dimensional surfaces responding to hydrogeomorphic behavior (*e.g.*, temporal GIS).

In this chapter, we present the topological initialization of two distributed models for hydrologic and geomorphologic prediction in real watersheds. The new approach for constructing TIN models depends on the derivation of an index that represents the steady-state process response to hydrometeorological forcing. Conceptually, the similarity approach embeds *a priori* process knowledge in the TIN structure. The new method also bridges two existing approaches, topographic distribution functions and finite-element meshes, to provide an objective, physically-based terrain representation.

We test the new algorithm in applications of hydrologic, erosion and landslide modeling using the tRIBS and CHILD models. Comparisons of the integrated and distributed model behavior reveal the advantages in the proposed approach including: (1) an improved resolution in catchment areas undergoing basin saturation, erosion or landsliding; (2) a shift in the distributed model response towards the hydrogeomorphic

process captured by the landscape index; and (3) an objective means for determining terrain resolution based on process knowledge. Determining whether the process-based triangulation method is strictly better than the traditional method involves spatially-distributed field tests where the extent of saturation, erosion and landsliding is compared to both methods. Currently, these field data are not available in the study basins for this purpose. Nevertheless, we believe that the new method is promising and can be used to objectively construct terrain models that embed process knowledge.

References

Ambroise, B., Beven, K. and Freer, J. 1996. Toward a generalization of the Topmodel concepts: topographic indices of hydrological similarity. *Water Resources Research.* 32(7), 2135-2145.

Barling, R.D., Moore, I.D. and Grayson, R.B. 1994. A quasi-dynamic wetness index for characterizing the spatial distribution of zones of saturation and soil water content. *Water Resources Research.* 30(4), 1029-1044.

Beven, K.J. and Kirkby, M.J. 1979. A physically-based variable contributing area model of basin hydrology. *Hydrological Sciences Bulletin.* 24, 43-69.

Beven, K., Lamb, R., Quinn, P., Romanowicz, R. and Freer, J. 1995. Topmodel. In *Computer Models of Watershed Hydrology*, ed. V.P. Singh. Water Resources Publications, Boulder CO. 627-668.

Borga, M., Fontana, G.D. and Cazorzi, F. 2002. Analysis of topographic and climatic controls on rainfall-triggered shallow landsliding using a quasi-dynamic wetness index. *Journal of Hydrology.* 268(1-4), 56-71.

Burton, A. and Bathurst, J. 1998. Physically based modeling of shallow landslide sediment yield at the catchment scale. *Environmental Geology.* 35(2-3), 89-99

Cignoni, P., Puppo, E. and Scopigno, R. 1997. Representation and visualization of terrain surfaces at variable resolution. *Visual Computer.* 13, 199-217.

Dietrich, W.E., Reiss, R., Hsu, M.-L. and Montgomery, D.R. 1995. A process-based model for colluvial soil depth and shallow landsliding using digital elevation data. In: *Scale issues in hydrological modelling,* ed. J.D. Kalma and M. Sivaplan. John Wiley & Sons. New York, 141-158.

Ivanov, V.Y., Vivoni, E.R., Bras, R.L. and Entekhabi, D. 2003. Development of a triangulated irregular network mdoe for real-time, continuous hydrologic forecasting. Submitted to *Water Resources Research.*

Lee, J. 1991. Comparison of existing methods for building triangular irregular network models of terrain from grid digital elevation models. *International Journal of Geographical Information Systems.* 5(3), 267-285.

Mita, C., Catsaros, N. and Gounaris, N. 2001. Runoff cascades, channel network and computation hierarchy determination on a structured semi-irregular triangular grid. *Journal of Hydrology*. 244, 105-118.

Mitasova, H., Hofierka, J., Zlocha, M. and Iverson, L.R. 1996. Modelling topographic potential for erosion and deposition using GIS. *International Journal of Geographical Information Systems*. 10(5), 629-641.

Montgomery, D.R. and Dietrich, W.E. 1994, A physically based model for the topographic control on shallow landsliding. *Water Resources Research*. 30(4), 1153-1171.

Montgomery, D.R., Sullivan, K. and Greenberg, H.M. 1998. Regional test of a model for shallow landsliding. *Hydrological Processes*. 12, 943-955.

Moore, I.D. and Burch, G.J. 1986. Sediment transport capacity of sheet and rill flow: Application of unit stream power theory. *Water Resources Research*. 22(8): 1350-1360.

Moore, I.D., Grayson, R.B. and Landson, A.R. 1991. Digital terrain modeling: a review of hydrological, geomorphological and biological applications. *Hydrological Processes*. 5, 3-30.

Moore, I.D., Norton, T.W. and Williams, J.E., 1993. Modelling environmental heterogeneity in forested landscapes. *Journal of Hydrology*. 150, 717-747.

Moore, I.D. and Wilson, J.P. 1992. Length-slope factors for the Revised Universal Soil Loss Equation: Simplified method of estimation. *Journal of Soil and Water Conservation*. 47(5), 423-428.

Nelson, E.J., Jones, N.L. and Berrett, R.J. 1999. Adaptive tessellation method for creating TINs from GIS data. *Journal of Hydrologic Engineering*. 4(1), 2-9.

O'Loughlin, E.M. 1986. Prediction of surface saturation zones in natural catchments by topographic analysis. *Water Resources Research*. 22(5), 794-804.

Palacios-Velez, O.L., Gandoy-Bernasconi, W. Cuevas-Renuad, B. 1992. Geometric analysis of surface runoff and the computational order of unit elements in distributed hydrologic models. *Journal of Hydrology*. 211, 266-274.

Renard, K.G., Foster, G.R., Weesies, G.A. and Porter, J.P. 1991. Revised universal soil loss equation. *Journal of Soil and Water Conservation*. 41(1), 30-33.

Rodriguez-Iturbe, I. and Rinaldo, A. 1997. *Fractal River Basins: Change and Self-Organization*. Cambridge University Press. Cambridge, UK.

Selby, M.J. 1993. *Hillslope Materials and Processes*. Oxford University Press. New York.

Tarboton, D.G., Bras, R.L. and Rodriguez-Iturbe, I. 1989. Scaling and elevation in river networks. *Water Resources Research*. 25(9), 2037-2051.

Tsai, V.J.D. 1993. Delaunay triangulations in TIN creation: an overview and a linear-time algorithm. *International Journal of Geographical Information Systems*. 7(6), 501-524.

Tucker, G.E., Lancaster, S.T., Gasparini, N.M., Bras, R.L. and Rybarczyk, S.M. 2001a. An object-oriented framework for distributed hydrologic and geomorphologic modeling using triangulated irregular networks. *Computers & Geosciences*. 27(8), 959-973.

Tucker, G.E., Lancaster, S.T., Gasparini, N.M. and Bras, R.L. 2001b. The Channel-Hillslope Integrated Landscape Development (CHILD) model. In *Landscape Erosion and Evolution Modelling*, ed. R.S. Harmon and W. Doe. Kluwer Academic/Plenum Publishers. Dordrecht. 349-388.

Tucker, G.E., Catani, F., Rinaldo, A. and Bras, R.L. 2001c. Statistical analysis of drainage density from digital terrain data. *Geomorphology*. 36, 187-202.

Vázquez, R.F., Feyen, L., Feyen, J. and Refsgaard, J.C. 2002. Effect of grid size on effective parameters and model performance of the MIKE-SHE code. *Hydrological Processes*. 16, 355-372.

Vivoni, E.R., Ivanov, V.Y., Bras, R.L. and Entekhabi, D. 2002. Topography, triangular irregular networks and hydrological similarity. Submitted to *Journal of Hydrologic Engineering*.

Walker, J.P. and Willgoose, G.R. 1999. On the effect of digital elevation model accuracy on hydrology and geomorphology. *Water Resources Research*. 35(7), 2259-2268.

Willgoose, G., Bras, R.L., Rodríguez-Iturbe, I. 1991. A physical explanation of an observed link area-slope relationship. *Water Resources Research*. 27(7): 1697-1702.

Wilson, J.P. and Gallant, J.C. 1996. EROS: A grid-based program for estimating spatially-distributed erosion indices. *Computers & Geosciences*. 22(7), 707-712.

Woods, R.A., Sivapalan, M. and Robinson, J. S. 1997. Modeling the spatial variability of subsurface runoff using a topographic index. *Water Resources Research*. 33(5), 1061-1073.

Wu, J. and Amaratunga, K. 2002. Wavelet triangular irregular networks. *International Journal of Geographic Information Science*, In press.

Zhang, W. and Montgomery, D.R. 1994. Digital elevation model grid size, landscape resolution, and hydrologic simulations. *Water Resources Research*. 30(4), 1019-1028.

Chapter 4:

Effects of Triangulated Terrain Resolution on Distributed Hydrologic Model Response

4.1 Introduction

Topography exerts a primary control on the distribution of hydrologic processes occurring across a range of scales from individual hillslopes to continental basins (*e.g.*, Beven and Kirkby, 1979, Wood *et al.,* 1990, Wood *et al.,* 1997). The importance of accurate topography in hydrological studies underlies recent efforts to improve elevation measurements using remote sensing (*e.g.*, Farr and Kobrick, 2000, Gesch *et al.,* 2002, Schmugge *et al.*, 2002). As a result, topographic products are currently available at various levels of accuracy for large extents of the Earth's surface. Increased volumes of terrain data create the challenge of how to best utilize digital elevation models (DEM) in hydrologic simulations (*e.g.*, Bates *et al.,* 2003). Essential terrain variability must be captured while maintaining a level of detail commensurate with the model. In distributed hydrologic modeling, the full integration of high-resolution DEMs (1-50 meters) is not currently feasible without introducing errors associated with terrain aggregation (Zhang and Montgomery, 1994, Walker and Willgoose, 1999).

Understanding topographic aggregation and its influence on hydrologic models is crucial for predicting catchment response (*e.g.*, Famiglietti and Wood, 1994). The effect of model resolution on grid-based hydrological simulations has been frequently explored (*e.g.*, Vieux, 1993, Xevi *et al.*, 1997, Kuo *et al.*, 1999, Molnár and Julien, 2000, Horritt and Bates, 2001, Vázquez *et al.,* 2002, Haddeland *et al.,* 2002). In addition, the impact of

DEM resolution on TOPMODEL predictions has been a subject of considerable research (*e.g.*, Zhang and Montgomery, 1994, Wolock and Price, 1994, Bruneau *et al.*, 1995, Brasington and Richards, 1998, Higy and Musy, 2000, Valeo and Moin, 2000, Wolock and McCabe, 2000). In both cases, the availability of high-resolution DEMs motivated the search for an 'optimal' grid size. For most applications, a tradeoff is required between the errors introduced by terrain coarsening and computational model demands. As a result, it is common practice to use hydrologic model resolutions various times greater than the original DEM size, especially for large watershed applications (*e.g.*, Wigmosta *et al.*, 1994, Vázquez *et al.*, 2002, Downer *et al.*, 2002). In such cases, a spatial sensitivity analysis addressing the tradeoffs between domain resolution, hydrologic variability and computational performance should be a fundamental part of the model verification process. Similarly, terrain aggregation needs to be considered during model calibration in order to identify scale variations and compensation in parameter values (*e.g.*, Saulnier *et al.*, 1997, Brasington and Richards, 1998, Vázquez *et al.*, 2002).

A promising approach for incorporating large quantities of high-resolution terrain data into hydrology models is the use of triangulated irregular networks (TIN). As an alternative to raster-DEMs, TINs adaptively sample topography according to a point selection criterion (*e.g.*, Lee, 1991, Kumler, 1994). Furthermore, TINs provide multiple resolutions in two forms: (1) intra-model variability in element sizes (variable resolution within a basin), and (2) inter-model variability of point density (basin representations at different resolutions). Both features permit the construction of adaptive, multiscale TIN models from a single resolution DEM. Given the potential uses of TINs for hydrologic modeling, the effect of TIN resolution on hydrologic predictions is a critical question.

In this chapter, we analyze the impact of model resolution on the predictions of the TIN-based Real-time Integrated Basin Simulator (tRIBS) (Ivanov *et al.*, 2003a). First, the spatial aggregation of the triangulated terrain over a series of basins is illustrated to highlight the relationship between TIN horizontal density and vertical accuracy. A multiple resolution validation is then conducted with the tRIBS model applied to a 64 km^2, gauged basin in Oklahoma. For a set of calibrated parameters obtained from long-term simulations, the multi-scale validation test is used to assess the variation in hydrologic response over a wide range of resolutions. Both basin-averaged and spatially distributed performance metrics are used to explain the interaction between hydrological processes and terrain resolution. The spatial sensitivity test reveals the relationship between basin response and catchment partitioning and suggests an appropriate choice for model resolution which resolves the critical variable sources area.

4.2 Spatial Aggregation of Triangulated Terrain

Terrain aggregation affects the slope, aspect and curvature fields which in turn influence model predictions of runoff and moisture dynamics. Studies by Vieux (1993), Brown *et al.* (1993) and Kuo *et al.* (1999) suggest that the aggregation effect on hydrologic model response can be deduced from the coarsening of terrain properties. In particular, the effect of model resolution on topographic curvature has been highlighted as an important control on hydrologic response, including the soil moisture distribution and runoff production (Kuo *et al.*, 1999). Since catchments vary widely in topographic form, it is expected that spatial aggregation effects are site-specific and related to basin geomorphic properties, such as terrain roughness (*e.g.*, Wolock and McCabe, 2000).

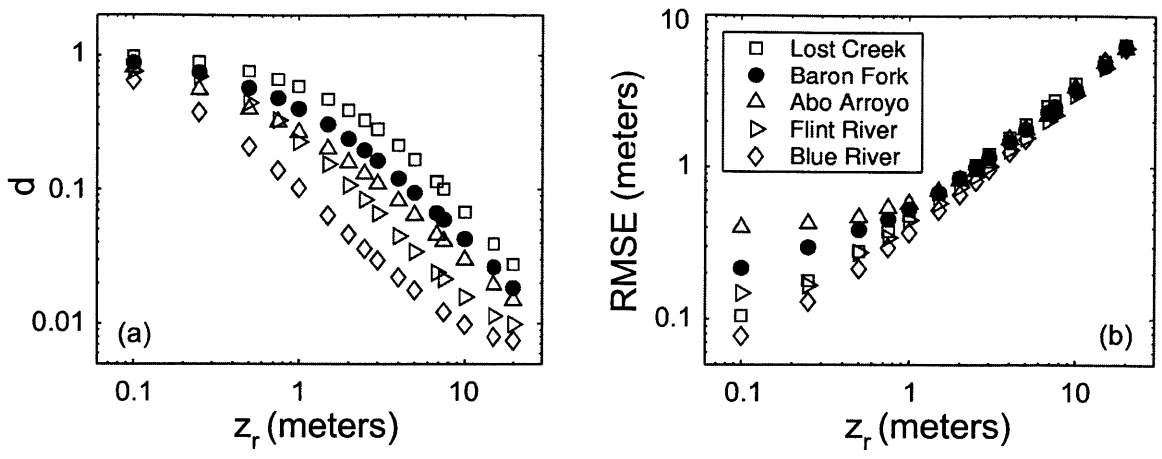

Figure 4.1. TIN aggregation characteristics for a series of watersheds (see Table 4.1). (a) Horizontal TIN resolution ($d = n_t/n_g$) and (b) root mean square error (*RMSE*) between TIN and original DEM as a function of the vertical tolerance parameter (z_r).

The effect of TIN resolution on terrain attributes, such as slope and curvature, has received limited attention. An appropriate metric is first required for concisely describing TIN resolution and relating it to terrain model accuracy. In computational geometry, the sampling of a DEM into a TIN of a specified number of nodes is often used to quantify spatial aggregation (de Berg and Dobrindt, 1998). In this study, we define the horizontal point density (d) to capture the degree of aggregation in a TIN model as:

$$d = \frac{n_t}{n_g}, \tag{4.1}$$

where n_t and n_g are the number of TIN and DEM nodes, respectively. Large values of d imply that the TIN approaches the original DEM. Comparisons of terrain attributes and hydrologic simulations across a range of d should reveal the effect of terrain aggregation.

For hydrographic TINs, the horizontal resolution is varied by selecting different values of the vertical tolerance (z_r). Figure 4.1a presents the relationship between z_r and d for a series of watersheds listed in Table 4.1. To derive each relation, a hydrographic TIN

Watershed	A [km^2]	r [m]	n_g [#]	μ [m]	σ [m]	Δz [m]
Abo Arroyo, NM	990.29	28.16	1,248,806	1854.87	222.20	1624.94
Baron Fork, OK	808.15	30.00	897,949	346.54	59.02	367.88
Blue River, OK	1236.38	30.00	1,373,762	259.48	66.49	245.23
Flint River, GA	697.71	30.00	775,242	264.79	19.71	105.00
Lost Creek, UT	576.58	27.06	787,296	2172.37	195.55	1021.33

Table 4.1. Watershed characteristics from USGS DEMs. A is the basin area; r is the grid resolution; n_g is the number of DEM cells; μ is the mean elevation; σ is the elevation standard deviation; Δz is the elevation range.

was constructed from the DEM at each tolerance level (z_r = 0.1 to 20 m), resulting in d = 0.01 to 1. In comparing the basins, it is apparent that the $z_r - d$ relation depends strongly on the terrain properties. The catchments differ substantially in topography, as captured by the elevation standard deviation (σ). As σ is increased, the horizontal resolution required to achieve a given tolerance level increases. For instance, a vertical tolerance of z_r = 2.5 m is attained in the Blue River (low σ) with a low resolution (d = 0.04), while for the Lost Creek (high σ) a higher resolution (d = 0.33) is required.

A second metric for evaluating TIN model accuracy is the root mean square error (*RMSE*) between the TIN and the original DEM. Figure 4.1b shows the variation of *RMSE* with z_r for the series of basins in Table 4.1. As the vertical tolerance increases, the vertical accuracy in the TIN model decreases. The *RMSE* provides a better indication of the global elevation error as compared to the maximum deviation captured in z_r. As a result, the range of *RMSE* values (0.08 to 6.4 m) is narrower. In comparing the basins, notice that *RMSE* differences are mostly observed for low values of z_r. As the tolerance level is increased beyond z_r = 1 m, the TIN model accuracy is similar across a range of different topographic characteristics. For example, the Abo Arroyo (high σ) and the Blue River (low σ) have similar *RMSE* for z_r = 10 m, but larger differences for z_r = 0.1 m.

The relations between the tolerance parameter (z_r) and the horizontal density (d) and vertical accuracy (*RMSE*) can be used to select an appropriate TIN resolution. For example, choosing a tolerance of z_r = 1 m for the Baron Fork will lead to a TIN with d = 0.4 and *RMSE* = 0.53 m. This aggregation level can then be compared to the required computational demands and terrain precision for the hydrologic application. Hydrologic response is expected to be a function of TIN resolution with inter-model (range of d) variability playing an important role. Optimizing the selection of d should lead to a resolution fine enough to leave results unaltered, yet coarse enough to allow for efficient simulations. In the following, we seek to explain the variability of a TIN-based hydrology model with respect to the aggregation of the triangulated terrain.

4.3 Distributed Hydrologic Modeling on Triangulated Terrain

Distributed models simulate watershed processes by taking into account rainfall, terrain, surface and subsurface heterogeneities (*e.g.*, Wigmosta *et al.*, 1994, Garrote and Bras, 1995). The selected domain resolution determines the level of detail retained in the landscape descriptors. Resampling basin features onto a common resolution impacts the simulation of hydrologic processes. Processes with characteristic lengths smaller than the element size are parameterized, while larger scale processes are explicitly represented (Blösch and Sivapalan, 1995). While this has been addressed in grid models, the effect of TIN resolution on basin processes has received little attention. Given the availability of TIN-based hydrology models (Goodrich *et al.*, 1991, Palacios-Vélez and Cuevas-Renaud, 1992, Tachikawa *et al.*, 1994, Tucker *et al.*, 2001), understanding the effect of terrain coarsening on hydrologic simulations is essential for determining an appropriate model resolution that minimizes computational effort while retaining hydrologic accuracy.

In this chapter, we test the spatial sensitivity of the tRIBS model, a distributed model designed for real-time, continuous hydrologic forecasting (Ivanov *et al.*, 2003a). In previous studies, tRIBS has been used for multi-year flood simulations in three basins, Blue River (1230 km^2), Baron Fork (808 km^2) and Illinois River (1640 km^2), using rainfall estimates from NEXRAD (Ivanov *et al.*, 2003b). The distributed model has also been coupled to a radar nowcasting model to provide flood forecasts at multiple gauges (Vivoni *et al.*, 2003a). Previously, model resolution has been selected through an ad-hoc procedure by retaining high terrain accuracy while reducing the number of nodes. Typically, a single value for the vertical tolerance (z_r) was chosen such that the resolution (d) was in the range of 3–7% and n_t was less than 100,000 nodes. For example, the Baron Fork TIN used in Ivanov *et al.* (2003a) consisted of n_t = 66,000 nodes (d = 0.08) with z_r = 6.8 m and $RMSE$ = 2.3 m. This resolution permitted a reasonable computational effort for multi-year simulations in the basin. The sensitivity analysis conducted here should show the degree of model coarsening allowable without loosing hydrologic accuracy.

4.4 Study Catchment and Model Simulations

To investigate the effect of TIN resolution on hydrologic simulations, we selected the Peacheater Creek in Christie, OK, due to its size and complex terrain (Figure 4.2a). The basin is a 64 km^2 gauged subbasin of the Baron Fork watershed consisting primarily of silt loam soils and forested (42%), grassy (57%) and urban (1%) areas. Basin elevation varies from 248 m near the outlet to 432.5 m along an isolated ridge in the northeast. Given its location in the Ozark Plateau, the southern part is rugged and heavily dissected while the northern portion is flat or gently sloping. The basin TIN is derived from a USGS 30-m DEM (n_g = 70,966) using the hydrographic TIN procedure and including the

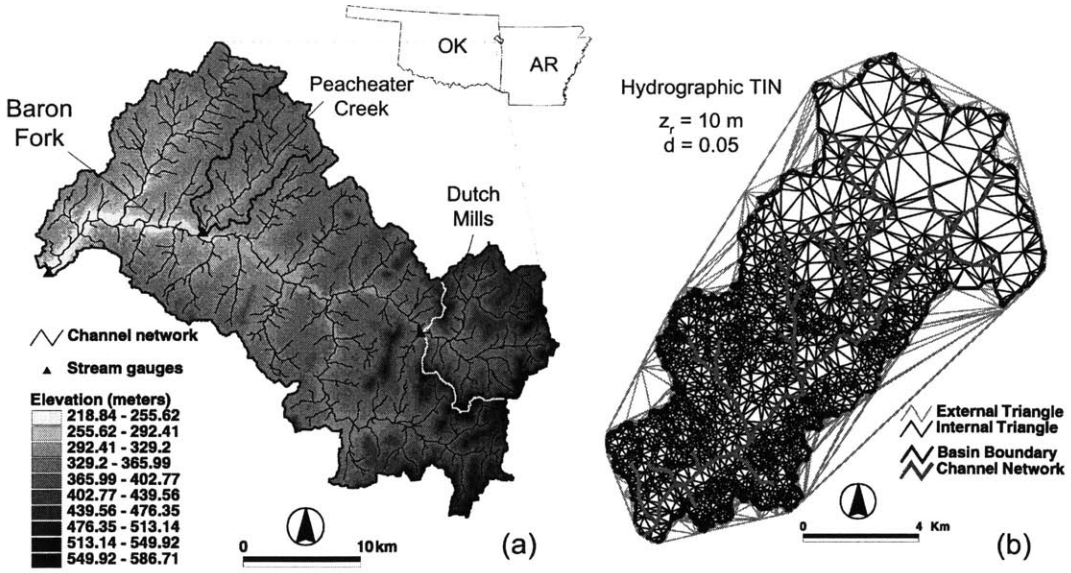

Figure 4.2. Location of study catchment. (a) Digital elevation model for the Peacheater Creek basin as subcatchment of the Baron Fork along the Oklahoma-Arkansas border. (b) Peacheater Creek TIN at coarse resolution ($d = 0.05$, $n_t = 3811$).

stream network and basin boundary derived from the DEM. TIN elements within the basin vary in size according to the slope distribution, with larger elements found along the plateau region and floodplains and the smaller triangles concentrated along the rugged hillslopes. Figure 4.2b shows the TIN domain at a coarse resolution ($d = 0.05$).

4.4.1 Hydrologic and Topographic Representation

Topographic complexity in the Peacheater Creek controls the catchment response to rainfall via interactions between the active shallow aquifer, stream network and land-surface (Vivoni *et al.*, 2003b). Lateral moisture redistribution driven by surface gradients leads to regions that are saturated (unsaturated) near convergent (divergent) areas. In addition, groundwater flow is controlled by surface gradients since the aquifer thickness is nearly constant in the basin (Imes and Emmett, 1994). Changes in TIN resolution and

associated terrain attributes (e.g. elevation, slope, curvature) should lead to variations in surface and subsurface hydrologic flow pathways and gradients.

Figure 4.3 shows the variation of the TIN resolution and vertical accuracy with the selection of the tolerance parameter for Peacheater Creek. By varying z_r from 0.1 to 20 m, the TIN resolution changed from d = 0.94 (fine) to 0.03 (coarse). As d increases, the number of TIN nodes approaches the DEM with a corresponding decrease in *RMSE*. The three arrows in Figure 4.3a point to the domains (d = 0.94, 0.42, 0.05) shown in Figures 4.3b-d as Voronoi polygon distributions. Note the element size vary in the basin (intra-model) for each d and also between the different basin representations (inter-model). For the fine domain, the Voronoi polygons approach the DEM cell size.

4.4.2 Model Parameterization and Calibration

Topographic and land-surface characteristics in the Peacheater Creek were used to parameterize and calibrate the tRIBS model. Model calibration was undertaken through a manual procedure that adjusts soil, vegetation and channel parameters to match the observed stream hydrograph for a sequence of storm and interstorm periods. The multi-step procedure ensures that model performance is reliable at the element, hillslope and catchment scales. Table 4.2 presents a subset of the calibration parameters obtained from the modeling effort reported by Ivanov *et al.* (2003b). Initial parameter estimates were based on established relationships to soils and vegetation types (*e.g.*, Bras, 1990). The calibration exercise then consisted of tuning a limited number of parameters within narrow ranges while retaining the spatial distribution of the soil and vegetation classes.

Model calibration was carried out for a single resolution d = 0.08 (z_r = 6.8 m) using flow data at Baron Fork during 1993-1999. This resolution allowed for efficient

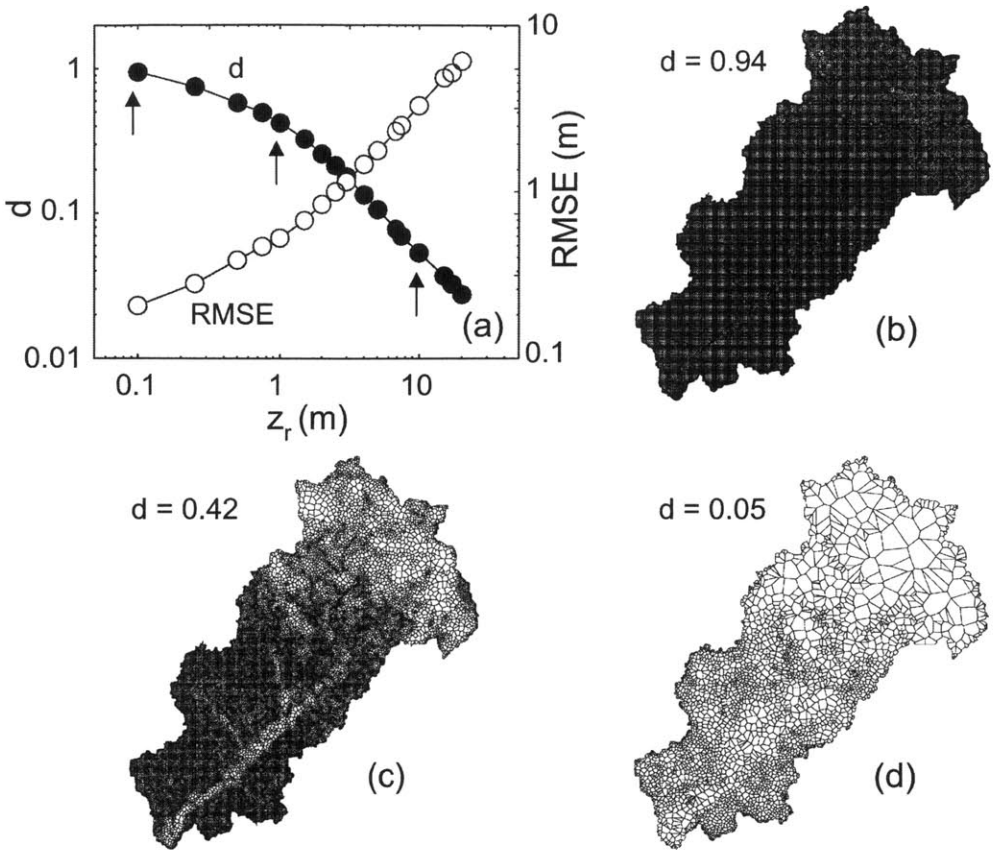

Figure 4.3. Multiple resolution models for Peacheater Creek. (a) Horizontal point density (*d*) and vertical accuracy (*RMSE*) as a function of tolerance level (z_r). Voronoi polygons for $d = 0.94$ (b), 0.42 (c) and 0.05 (d) corresponding to $z_r = 0.1$, 1 and 10 meters.

multi-year simulations over the large domain with good performance in the Peacheater Creek over the period (Ivanov *et al.*, 2003a,b). Calibrated parameters are considered to be robust in light of the multi-year verification. In addition, the calibrated set performance well when transferred to the adjacent Illinois River (Ivanov *et al.*, 2003b). We deem the calibration adequate for the purpose of evaluating the variation of hydrologic predictions with TIN resolution. Simulations in the Peacheater Creek also allow the full range of resolutions (d = 0.01 to 0.94) to be explored with reasonable computational effort, as compared to the larger basins.

Parameter	*Units*	*Soil and Land Cover Classification*		
		Forest	Grassland	Urban
Soils Properties				
K_s	[mm/hr]	35	2.8	0.5
θ_s	[–]	0.4	0.3	0.3
θ_r	[–]	0.05	0.05	0.05
λ_o	[–]	0.3	0.25	0.2
ψ_b	[mm]	-100	-200	-400
f	[mm^{-1}]	0.0009	0.0004	0.0007
a_r	[–]	400	400	200
Vegetation Properties				
a	[–]	0.16	0.2	0.13
h	[m]	12	0.7	0.1
K_t	[–]	0.8	0.9	0.8
r_s	[s/m]	60	40	100
v	[–]	0.6	0.65	0.1

Table 4.2. Subset of tRIBS model parameter values for the Peacheater Creek simulations. K_s: saturated hydraulic conductivity; θ_s: soil moisture at saturation; θ_r: residual soil moisture; λ_o: pore distribution index; ψ_b: air entry bubbling pressure; f: conductivity decay; a_r: anisotropy ratio; a: albedo; h: vegetation height; K_t: optical transmission coefficient; r_s: minimum stomatal resistance; v: vegetation fraction.

4.4.3 Simulation Period and Model Initialization

The tRIBS model was applied for each TIN resolution for a one year period from November 1997 to 1998. This period was selected since various major storms passed through the basin and the wet winter and dry summer seasons were well represented. The initial interstorm conditions allowed for model initialization with respect to the recorded USGS baseflow discharge (Q_b). Hourly rainfall observations from NEXRAD and surface weather data were used to force the model continuously over the simulation period. A total of 1194 mm of precipitation were measured from NEXRAD (4-km by 4-km) during the year averaged over the basin. The rainfall and meteorological forcing were held constant between resolutions to ensure appropriate hydrologic comparisons. In addition, the basin area and stream network were represented equally across catchment resolutions.

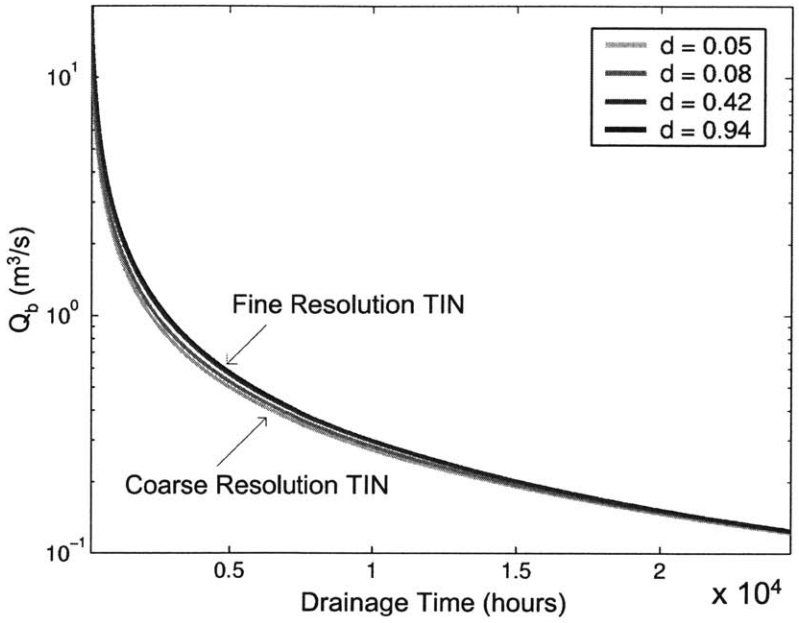

Figure 4.4. Baseflow discharge (Q_b) during the Peacheater Creek drainage experiments for d = 0.94, 0.42, 0.08 and 0.05.

Preliminary simulations revealed the sensitivity of the different resolutions to the initial water table position (not shown). In order to minimize these effects, we obtained the saturated depth by conducting a drainage experiment using the calibrated model. For each TIN, the basin was drained from a saturated state, in the absence of rain and evaporation, until the observed initial baseflow (Q_b = 0.1 m^3/s) was reached. This allowed for a readjustment of the water table in the topographic context of each TIN. Figure 4.4 shows the variation of baseflow drainage with d, particularly over the first year. The coarse TIN exhibits faster subsurface drainage relative to the finer resolutions. As time progresses, differences in Q_b are minimized, with Q_b = 0.1 m^3/s reached in 3.3 to 3.5 years into the drainage period. The groundwater field corresponding to the observed Q_b was then used to initialize the water table depth and soil moisture profile in the basin.

Preliminary studies also indicated the need to account for the dynamic adjustment of the water table distribution under conditions of rainfall and evaporation. To minimize these transient effects, we forced the model with the 1997-1998 sequence of rainfall and meteorological data repeatedly over a multiple year period. We found that the periodic forcing allowed for a dynamic equilibrium to be reached after two years. Differences in the hydrograph response and basin water balance between the second and third year were minimal. As a result, we utilized the simulations from the third consecutive year as the basis for hydrologic comparison of the different TIN resolutions.

4.5 Results

The hydrologic performance of the tRIBS model is evaluated through a multiple resolution validation using the calibrated parameter set. Refsgaard (1997), Molnár and Julien (2000) and Vázquez *et al.* (2002) performed similar tests in the context of grid models. These studies highlighted the variability in flood response with respect to grid size and suggested a resolution minimizing computational effort while retaining realistic model performance. In the following, we present the effects of TIN model resolution on several integrated and distributed metrics of basin response including the catchment hydrograph, basin water balance, runoff partitioning, and surface-groundwater dynamics.

4.5.1 Catchment Hydrograph

The variability of the basin hydrograph is indicative of the integrated catchment sensitivity to topographic resolution. Figure 4.5 shows the observed basin-averaged rainfall over the Peacheater Creek and the corresponding simulated discharge from four model resolutions (d = 0.05, 0.08, 0.42, 0.94) over the study period. As the model TIN

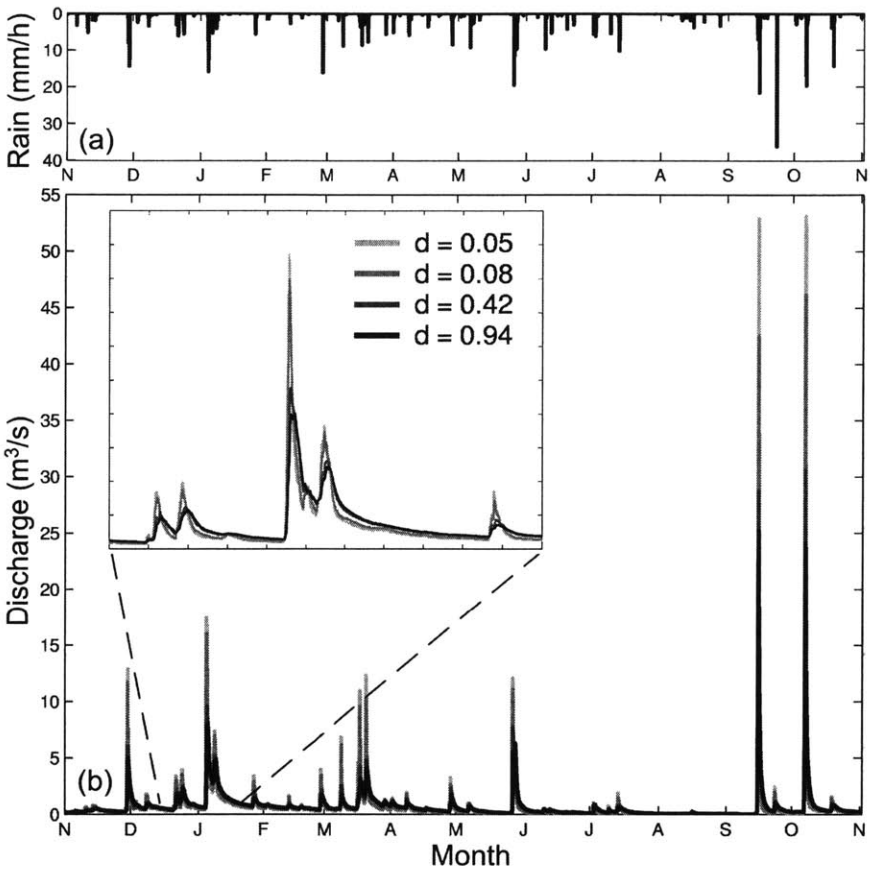

Figure 4.5. Catchment hydrographs at multiple resolutions over the one-year simulation. (a) Mean areal rainfall in Peacheater Creek. (b) Outlet discharge at: d = 0.05, 0.08, 0.42 and 0.94. The inserted figure details a 46 day period (12/16/1997 to 01/31/1998).

resolution is changed with the same calibration set, there are observable differences in peak discharge (Q_p), time to peak (t_p), runoff volume and baseflow recession. Over various storm events, the peak discharge decreases considerably as resolution is increasedfrom d = 0.05 to 0.42, while a smaller decrease is observed from d = 0.42 to 0.94. The higher peak rates for coarser model resolutions are accompanied by a decrease in the peak timing and an increase in the recession rate. The underlying causes for these hydrograph variations are related to the effect of terrain resolution on the model dynamics. For example, the increased baseflow recession results from the faster

subsurface drainage in coarser resolution models (Figure 4.4). The insert in Figure 4.5 highlights these hydrograph differences for a flood event in January 4–5, 1998.

The hydrograph variation with TIN resolution is further explored in Figure 4.6 by comparing Q_p and t_P over the full d range for three events of differing magnitudes. Peak discharge decreases as the resolution is varied from coarse (d = 0.03) to fine (d = 0.94). The rate of decrease in Q_p with d varies across resolutions and for each event. Events 1 to 3 experience a 57%, 72% and 63% drop in Q_p from coarse to fine domains, respectively. Decreases in Q_p are accompanied by increases in t_p. Notice that the sharpest changes are observed as the model resolution is coarsened to values less than d = 0.1. The variability in Q_p and t_p suggests that coarser domains result in a quicker, more pronounced flood response as compared to finer terrain models. The increase in t_p can be partially attributed to the lengthening of overland and channel flow paths as the number of model elements increases, while the decrease in Q_p should be related to differences in rainfall partitioning at the land-surface. To fully explain the resolution variation in discharge and response time, a closer look at the basin water balance and runoff generation processes follows.

4.5.2 Annual Water Balance

The variation in runoff response with terrain aggregation can be explored through the catchment hydrologic balance shown in Figure 4.7a for Peacheater Creek over the one-year simulation period. The water balance components are defined as:

$$\Delta S_S + \Delta S_U = P - ET - R\,, \tag{4.2}$$

where ΔS_S and ΔS_U are the changes in the saturated and unsaturated zone storage, P is the total rainfall, ET is the total evapotranspiration and R is the basin runoff. Normalized by

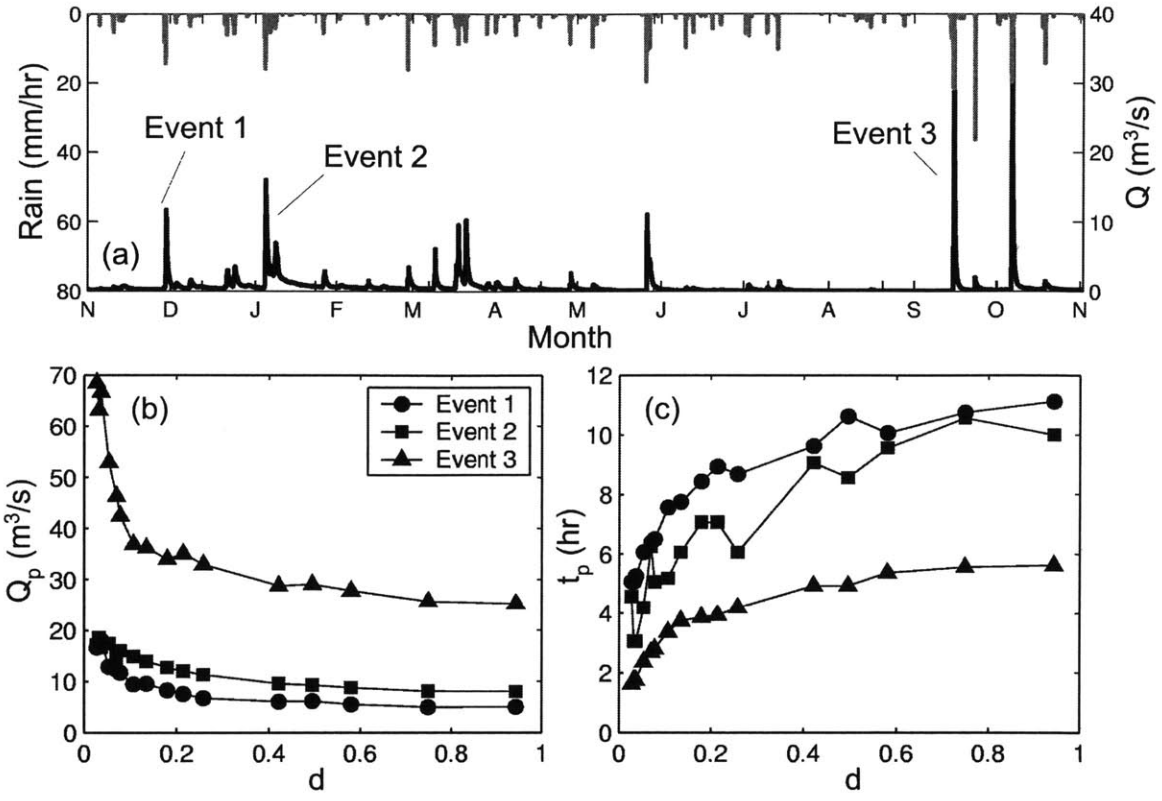

Figure 4.6. Hydrograph sensitivity to TIN resolution. (a) Basin-averaged rainfall and hydrograph for d = 0.08 with indication of three selected events. (b) Peak discharge Q_p (m^3/s) and (c) time to peak discharge t_p (hr) as a function of d for the selected events.

rainfall (P), (4.2) yields the fraction of incoming precipitation that is partitioned between the basin storage (ΔS_S, ΔS_U) and loss terms (ET, R). Rainfall partitioning is a function of the surface soil moisture state and the topographic gradients leading to lateral moisture exchanges in the unsaturated and saturated zones. As model resolution is varied, the water balance components reflect the moisture adjustments that occur over the annual period in each terrain context for the same applied rainfall.

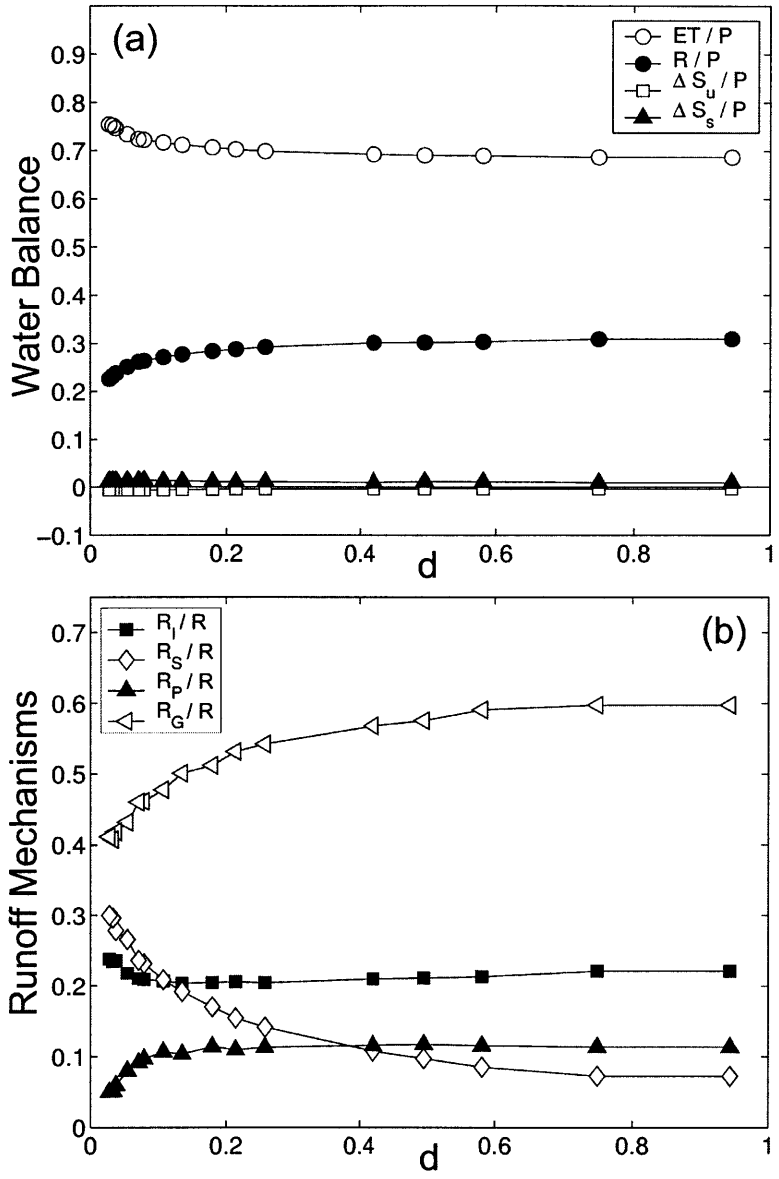

Figure 4.7. Hydrologic sensitivity to resolution. (a) Components of the basin water balance normalized by the total rainfall (P): evapotranspiration (ET), runoff (R) and the change in saturated (ΔS_S) and unsaturated (ΔS_U) storage over the study period. (b) Simulated runoff mechanisms as a fraction of total runoff: infiltration-excess runoff (R_I), saturation-excess runoff (R_S), perched return flow (R_P) and groundwater exfiltration (R_G).

The water balance highlights the importance of the loss terms in determining the spatial sensitivity of the hydrologic model. In Figure 4.7a, runoff and evapotranspiration depend on TIN resolution, in particular for coarse models ($d < 0.1$). ET decreases with higher d potentially due to differences in surface saturation among resolutions. In response to higher ET rates for coarse resolutions, runoff is observed to decrease over the range $d = 0.1$ to 0.03. It is interesting to note that changes in ET and R are minor over a broad range of resolutions. In addition, the sensitivity of ΔS_S and ΔS_U to d is small, as a result of the initialization conditions. By allowing each TIN to reach dynamic equilibrium prior to the simulations, meaningful hydrologic comparisons can be made across different terrain models. As a result, the dominant resolution effect in the multiscale hydrologic balance is the partitioning between evapotranspiration and runoff at the land-surface.

4.5.3 Runoff Mechanisms

Runoff sensitivity to terrain resolution is linked to the mechanisms leading to runoff generation within Peacheater Creek. Due to the interaction of moisture fronts in the unsaturated zone and the variable water table, total runoff from a particular location can be decomposed into a variety of runoff types (see Ivanov *et al.*, 2003a). At the catchment outlet, the total runoff (R) is partitioned into:

$$R = R_I + R_S + R_P + R_G, \tag{4.3}$$

where R_I, R_S, R_P and R_G correspond to infiltration-excess, saturation-excess, perched return flow and groundwater exfiltration runoff. Each component is separately generated throughout the basin and routed individually through the river network. Infiltration- and saturation-excess runoff correspond to a quick, surface flow response to rainfall (R_I+R_S), while groundwater baseflow and perched return flow are due to delayed, subsurface flow

resulting from lateral moisture exchanges (R_G+R_P). Figure 4.7b shows the variation of the runoff types with TIN resolution as a fraction of the total runoff (Figure 4.7a).

The runoff type variations with terrain resolution provide insights to the variable basin response to rainfall. Both R_I and R_P are relatively insensitive to resolution from d = 0.1 to 1, whereas both vary sharply over d = 0.03 to 0.1. In contrast, the aggregation effect on R_S and R_G occurs over the full resolution range. Note that a shift occurs in the dominant type of basin response near d = 0.08. Surface response (R_I+R_S) is more pronounced in the coarse domains, while subsurface response (R_G+R_P) is the principal mechanism in fine resolution models. For coarse models, runoff primarily occurs from rainfall on saturated regions, while for fine domains, runoff is produced predominantly via exfiltration of subsurface flow along streams. The shift from surface to subsurface runoff is consistent with the decrease in Q_p and the increase in t_p observed as the model domain progressively approaches the DEM resolution. These runoff variations are related to the sensitivity of surface saturation and groundwater dynamics to terrain resolution.

4.5.4 Surface Saturation Dynamics

Terrain aggregation effects on the saturation-excess runoff component are directly related to the extent of the surface saturated area within the basin. Precipitation on wet regions contributes quickly to surface runoff and leads to an early and pronounced discharge response. Changes in the dynamic saturation pattern or variable source area as the topographic resolution is altered lead to differences in rainfall partitioning into runoff and evapotranspiration. The fractional saturated area in the basin (a_S) is defined as:

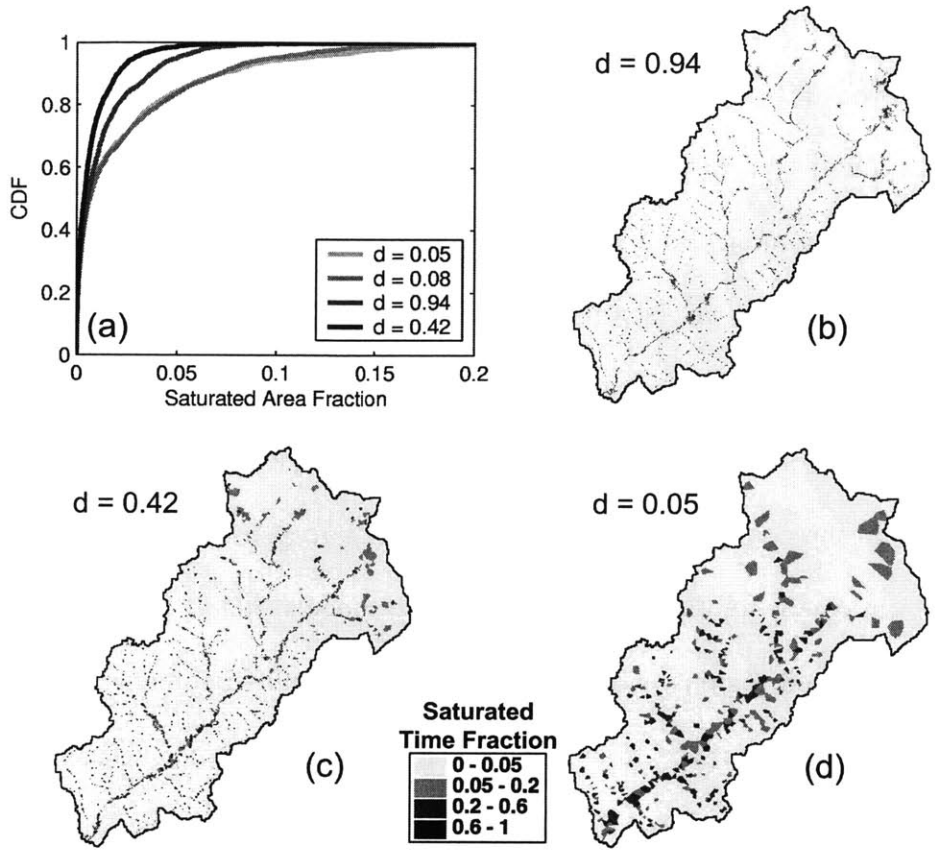

Figure 4.8. Surface saturation sensitivity to resolution. (a) Cumulative density function (CDF) of the saturated basin area fraction (a_S) for model resolutions: d = 0.05, 0.08, 0.42 and 0.94. The spatial distribution of saturation time as a fraction of the total simulation time is shown for d = 0.94 (b), d = 0.42 (c), and d = 0.05 (d).

$$a_S = \frac{A_S}{A} \qquad A_S = \sum_i \left(A_i \middle| \theta_s = 1\right), \tag{4.4}$$

where A is the total catchment area, A_i is the Voronoi polygon area, and θ_s is the surface soil moisture. Saturated elements (θ_s = 1) typically occur in convergent areas near the stream network or in topographic hollows which are sensitive to terrain resolution.

Figure 4.8a shows the cumulative density function (CDF) of a_S over the simulation period and its variability with TIN resolution. For coarse domains (d = 0.05, 0.08), high a_S values occur more frequently during the year, demonstrating that terrain resolution has a direct effect on saturation dynamics. Figures 4.8b-d illustrate the spatial

distribution of the surface saturation for resolutions d = 0.94, 0.42, 0.05. Here, the fraction of the total simulation time under saturation conditions (θ_s = 1) is shown for each model element at the different resolutions. As d decreases, saturated regions are poorly resolved near the stream network and occupy a larger area fraction. Larger saturated areas lead to greater runoff production from the saturation-excess mechanism. In addition, the increased saturated area leads to a higher potential for evapotranspiration. Differences in a_S with terrain aggregation lead to variability in rainfall partitioning at the land-surface.

4.5.5 Groundwater Dynamics

Groundwater dynamics vary with terrain aggregation as evidenced by the spatial sensitivity of the saturated drainage and groundwater exfiltration. In the saturated zone, lateral exchanges between elements are controlled by the gradient in the local water table:

$$Q_S = -Tw\frac{\partial z_H}{\partial l} = -Tw\tan\beta, \tag{4.5}$$

where Q_S is the groundwater flux, T is the aquifer transmissivity, w is the flow width, z_H is the saturated thickness, l is the flow distance and tan β is water table slope. Terrain aggregation will impact the subsurface flow geometry through the flow width (w) and distance (l) which leads to differences in subsurface gradients. Coarse resolutions tend to decrease Q_S as the gradients in the water table topography are reduced. This is consistent with the lower percentage of groundwater exfiltration observed in coarse resolutions.

Variations in the groundwater temporal dynamics due to differences in subsurface spatial gradients are shown in Figure 4.9a. Changes in the saturated thickness (Δz_H) over the simulation for d = 0.94, 0.42, 0.08, 0.05 are shown as cumulative density functions (CDF). Overall, Δz_H is small (± 0.1 m), due to the equilibrium conditions reached in the

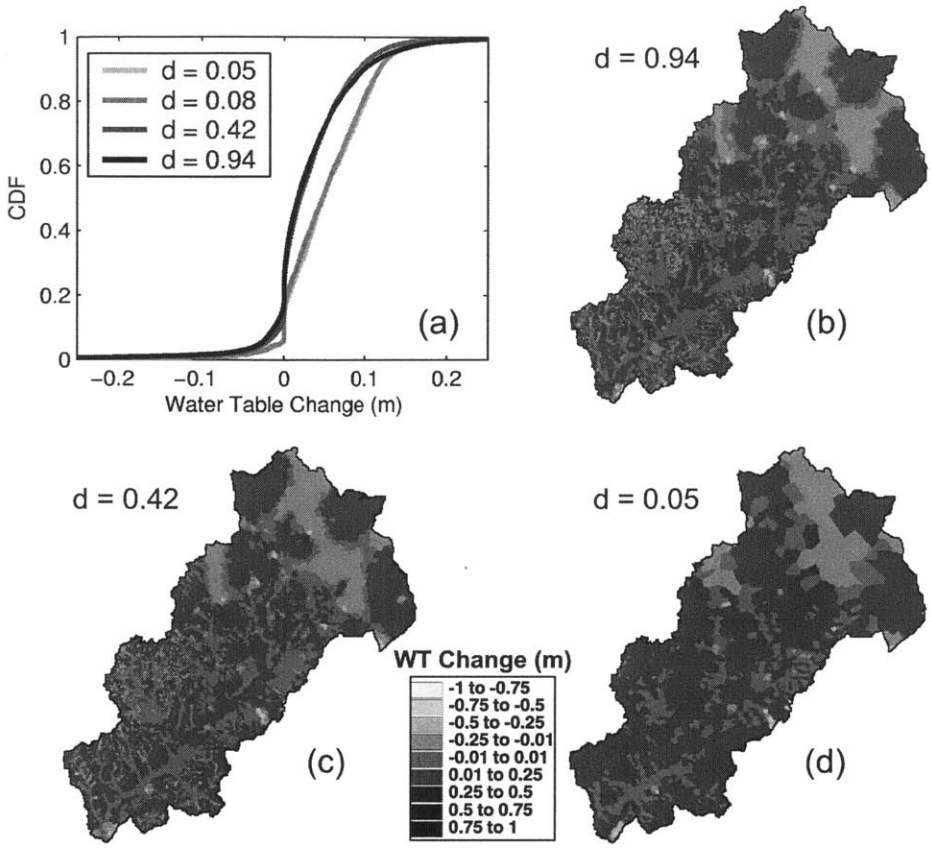

Figure 4.9. Groundwater dynamics sensitivity to resolution. (a) Cumulative density function (CDF) of the change in saturated zone thickness (Δz_H) over the simulation. The spatial distribution of Δz_H is shown for $d = 0.94$ (b), $d = 0.42$ (c), and $d = 0.05$ (d).

groundwater system prior to model simulations. Minor differences across d are due to variations in subsurface flows, with coarser models having a slightly higher increase in z_H during the period. This is consistent with the variability of the saturated storage in the basin water balance. The spatial organization of Δz_H into regions of net groundwater recharge ($+\Delta z_H$) or discharge ($-\Delta z_H$) is shown in Figures 4.9b-d. Note that as resolution is coarsened, larger elements lead to losses in the detailed recharge/discharge pattern observed in fine domains. Large element sizes near the channel network also lead to differences in groundwater dynamics that affect saturated zone drainage and baseflow recession.

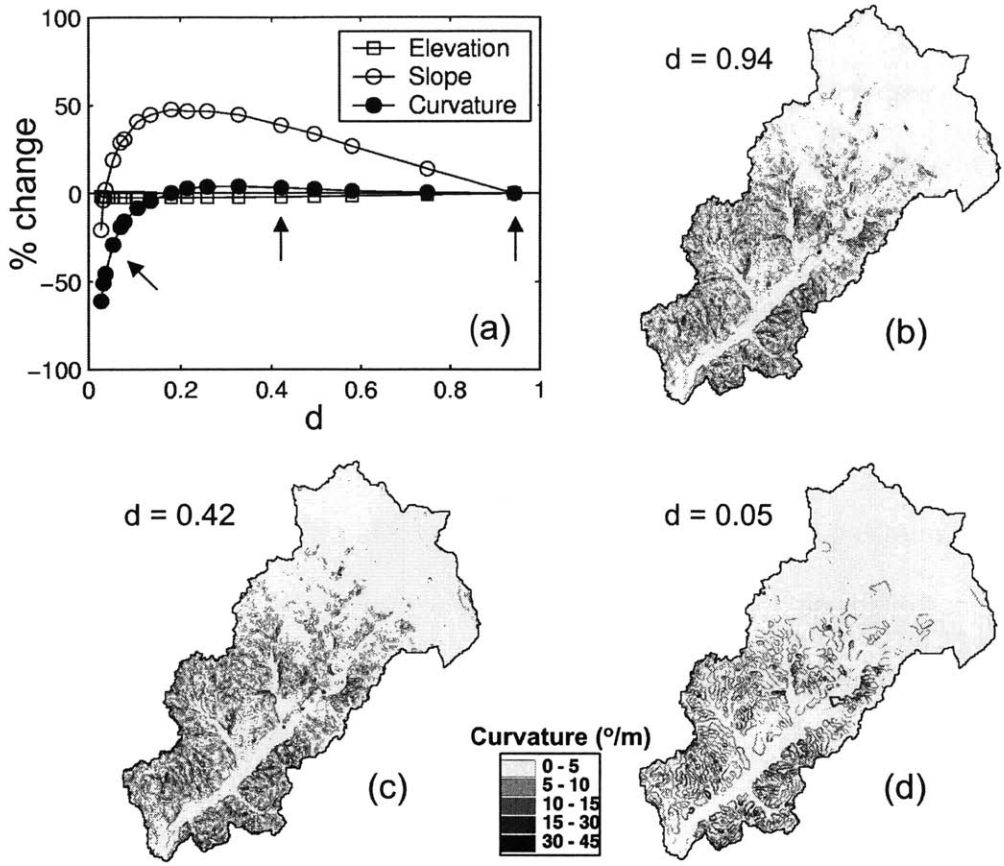

Figure 4.10. Terrain attribute sensitivity to resolution. (a) Percent change in mean basin elevation, slope and curvature from the highest resolution (d = 0.94). The three arrows point to the curvature fields shown for d = 0.94 (b), d = 0.42 (c), and d = 0.05 (d).

4.5.6 Terrain Attributes

The variation of the surface-subsurface dynamics with TIN resolution lead to differences in the basin response that can be explained through the aggregation properties of catchment elevation, slope and curvature. Figure 4.10a presents the sensitivity of the terrain attributes across the range of model resolutions for Peacheater Creek. Here, the percent change (%) in elevation, slope and curvature are shown in reference to the finest resolution (d = 0.94). Note that the mean elevation experiences a minimal % change with d, while the mean slope and curvature exhibit variations with model resolution. A gradual increase in mean slope is observed as the domain is coarsened from d = 0.94 to 0.1. Over

this interval, the mean curvature has minimal dependence on d. For coarse domains (d = 0.03 to 1), sharp changes are apparent in both the mean slope and curvature.

Figures 4.10b-d illustrate the spatial distribution of the curvature field for three resolutions (d = 0.94, 0.42, 0.05). While the curvature field is preserved when coarsening the TIN from d = 0.94 to 0.42, the lowest resolution model (d = 0.05) shows marked differences in the curvature distribution. As slope and curvature determine hydrologic gradients and flow convergence, the sensitivity of the terrain attributes in coarse domains is indicative of the hydrologic response variability. This is consistent with the resolution dependence in coarse domains (d = 0.03 to 0.1) identified in the basin hydrograph, water balance and runoff generation. From knowledge of the coarsening of the curvature field, for example, an estimate of the effect of TIN resolution on runoff generation can be determined prior to hydrologic model simulations.

4.6 Discussion and Conclusions

The spatial sensitivity analysis presented in this chapter has demonstrated the differences in hydrologic response as the triangulated terrain resolution is varied from values near the original DEM (d = 0.94; 66,959 nodes) to much coarser representations (d = 0.03; 1,968 nodes). The spatial aggregation of the TIN-based hydrology model impacts the prediction of the basin hydrograph as well as the spatial distribution of catchment response. Over a wide range of resolutions, we identified a relation between the sensitivity in the hydrograph response, the underlying surface-subsurface dynamics and the coarsening of terrain attributes. This was achieved by analyzing the resolution dependence of the basin water balance, the runoff generation mechanisms and spatial-

temporal dynamics of the surface saturated area and the subsurface zone. The insights provided by these hydrologic metrics suggest the following:

(1) The sensitivity of the hydrologic model to TIN resolution primarily occurs for coarse representations (d = 0.03 to 0.1) where large variations are observed in the storm hydrograph (Q_p, t_p), runoff partitioning (R_I, R_S, R_P, R_G), evapotranspiration (ET) and basin saturation fraction (a_s). The primary cause for these interrelated sensitivities is the loss of resolution in the flat, near-channel regions. When the domain is coarsened to the point of poorly resolving the variable source area, an overestimation of the saturated surface area occurs which subsequently affects rainfall partitioning. This, in turn, leads to a shift from slow subsurface runoff to quick surface flow, which impacts the basin hydrograph shape.

(2) Over a broad range of resolutions (d = 0.1 to 0.94), the sensitivity of the hydrologic model to topographic representation is minimal. Many processes exhibit weak resolution dependence in the direction of progressively finer domains. Over this range, the total basin runoff and evapotranspiration are rather constant. In addition, the variable source area and groundwater dynamics show similarities in temporal and spatial patterns. This weak sensitivity suggests that hydrologically-significant regions in the catchment are properly represented for resolutions finer than d = 0.1, which is also apparent from an analysis of the resolution effect on the terrain attributes (elevation, slope, curvature).

Minimizing the tradeoff between hydrologic model sensitivity and computational demands would suggest a minimum resolution near d = 0.1 for the Peacheater Creek simulations using the calibrated parameter set obtained by Ivanov *et al.* (2003b). This is consistent with the fact that the model calibration was obtained at a resolution d = 0.08, suggesting that hydrologic sensitivity is dependent on the calibration process. Calibrating

the model at a different resolution may shift the transition between weak and strong resolution dependence. Here, we identified that hydrologic sensitivity is strong for domains coarser than the calibrated resolution and weak for finer discretizations. This is an encouraging result that suggests performing the model calibration at a coarse enough resolution to allow for efficient model simulations. Higher resolution domains can then be simulated accurately with only minor changes to the calibrated parameter set.

Given the variation of basin response with TIN aggregation, selecting the domain resolution is a critical step during model calibration. The results in this chapter suggest that an adequate terrain model should capture the variable source areas at a high resolution. Near-stream regions are hydrologically-significant by contributing to runoff production and serving as primary zones for evapotranspiration. When poorly resolved, these regions lead to large discrepancies in hydrologic simulations, in particular causing a shift in the basin response towards surface runoff. Similar results were obtained by Vivoni *et al.* (2003c) by comparing a hydrologic-index TIN model with increased resolution in saturated areas with a coarse topographic model. Hydrologic sensitivity to TIN resolution decreases once the surface saturation areas are properly represented. This finding holds promise for the multiscale calibration and application of TIN-based hydrology models.

References

Bates, P.D., Marks, K.J. and Horritt, M.S. 2003. Optimal use of high-resolution topographic data in flood inundation models. *Hydrological Processes*. 17(3), 537-557.

Beven, K.J. and Kirkby, M.J. 1979. A physically-based variable contributing area model of basin hydrology. *Hydrological Sciences Bulletin*. 24, 43-69.

Blösch, G. and Sivapalan, M. 1995. Scale issues in hydrological modeling: A review. *Hydrological Processes*. 9, 251-290.

Bras, R.L. 1990. *Hydrology: An Introduction to Hydrologic Science*. Addison-Wesley Longman, Reading, MA.

Brasington, J. and Richards, K. 1998. Interactions between model predictions, parameters and DTM scales for Topmodel. *Computers & Geosciences*. 24(4), 299-314.

Brown, D.G., Bian, L. and Walsh, S.J. 1993. Response of a distributed watershed erosion model to variations in input data aggregation levels. *Computers & Geosciences*. 19(4), 499-509.

Bruneau P., Gascuel-Odoux C., Robin, P., Merot, P. and Beven, K. 1995. Sensitivity to space and time resolution of a hydrological model using digital elevation data. *Hydrological Processes*. 9, 69-81.

de Berg, M. and Dobrindt, K.T.G. 1998. On levels of detail in terrains. *Graphical models and image processing*. 60(1), 1-12.

Downer, C.W., Ogden, F.L., Martin, W.D. and Harmon, R.S. 2002. Theory, development, and applicability of the surface water hydrologic model *CASC2D*. *Hydrological Processes*. 16, 255-275.

Environmental Research Systems Institute. 1992. *Understanding GIS: the Arc/Info method*. ESRI Press. Redlands, CA. 400 pgs.

Famiglietti, J.S. and Wood, E.F. 1994. Multiscale modeling of spatially variable water and energy balance processes. *Water Resources Research*. 30(11), 3061-3078.

Farr, T.G. and Kobrick, M. 2000. Shuttle Radar Topography Mission produces a wealth of data. *American Geophysical Union. EOS*. 81, 583-585.

Garrote, L. and Bras, R.L. 1995. A distributed model for real-time flood forecasting using digital elevation models. *Journal of Hydrology*. 167, 279-306.

Gesch, D., Oimoen, M., Greenlee, S., Nelson, C., Steuck, M. and Tyler, D. 2002. The national elevation dataset. *Photogrammetric Engineering and Remote Sensing*. 68(1), 5-15.

Goodrich, D.C., Woolhiser, D.A. and Keefer, T.O. 1991. Kinematic routing using finite elements on a triangular irregular network. *Water Resources Research*. 27(6), 995-1003.

Haddeland, I., Matheussen, B.V. and Lettenmaier, D.P. 2002. Influence of spatial resolution on simulated streamflow in a macroscale hydrologic model. *Water Resources Research*. 38(8): doi:10.1029/2001WR000854.

Higy, C. and Musy, A. 2000. Digital terrain analysis of the Haute-Mentue catchment and scale effect for hydrologic modeling with TOPMODEL. *Hydrology and Earth System Sciences*. 4(2), 225-237.

Horritt, M.S. and Bates, P.D. 2001. Effects of spatial resolution on a raster based model of flood flow. *Journal of Hydrology*. 253, 239-249.

Imes, J.L. and Emmett, L.F. 1994. Geohydrology of the Ozark Plateaus Aquifer System in parts of Missouri, Arkansas, Oklahoma, and Kansas, *U.S. Geolologica Survey Professional Paper, 1414-D*.

Ivanov, V.Y., Vivoni, E.R., Bras, R.L. and Entekhabi, D. 2003a. Development of a TIN-based distributed hydrologic model for real-time, continuous forecasting. Submitted to *Water Resources Research*.

Ivanov, V.Y., Vivoni, E.R., Bras, R.L. and Entekhabi, D. 2003b. Preserving high-resolution surface and rainfall data in operational-scale basin hydrology: A fully-distributed, physically-based approach. Submitted to *Journal of Hydrology*.

Jenson, S.K. and Domingue, J.O. 1988. Extracting topographic structure form digital elevation data for geographic information system analysis. *Photogrammetric Engineering and Remote Sensing*. 54(11), 1593-1600.

Lee, J. 1991. Comparison of existing methods for building triangular irregular network models of terrain from grid digital elevation models. *International Journal of Geographical Information Systems*. 5(3), 267-285.

Kumler, M.P. 1994. An intensive comparison of triangulated irregular networks (TINs) and digital elevation models (DEMs). *Cartographica*. 31(2), Monograph 45, 48 pgs.

Kuo, W-L., Steenhuis, T.S., McCulloch, C.E., Mohler, C.L., Weinstein, D.A., DeGloria, S.D. and Swaney, D.P. 1999. Effect of grid size on runoff and soil moisture for a variable-source area hydrology model. *Water Resources Research*. 35(11), 3419-3428.

Molnár, D.K. and Julien, P.Y. 2000. Grid-size effects on surface runoff modeling. *Journal of Hydrologic Engineering*. 5(1), 8-16.

Nelson, E.J., Jones, N.L. and Berrett, R.J. 1999. Adaptive tessellation method for creating TINS from GIS data. *Journal of Hydrologic Engineering*. 4(1), 2-9.

Palacios-Velez, O.L. and Cuevas-Renaud, B. 1992. SHIFT: A distributed runoff model using irregular triangular facets. *Journal of Hydrology*. 134, 32-55.

Refsgaard, J.C. 1997. Parameterisation, calibration and validation of distributed hydrologic models. *Journal of Hydrology*. 198, 69-97.

Saulnier, G-M., Obled, C. and Beven, K. 1997. Analytical compensation between DTM grid resolution and effective values of saturated hydraulic conductivity within the Topmodel framework. *Hydrological Processes*. 11, 1131-1346.

Schmugge, T.J., Kustas, W.P., Ritchie, J.C., Jackson, T.J. and Rango, A. 2002. Remote sensing in hydrology. *Advances in Water Resources*. 25(8-12), 1367-1385.

Tachikawa, Y., Shiiba, M. and Takasao, T. 1994. Development of a basin geomorphic information system using TIN-DEM structure. *Water Resources Bulletin*. 30(1), 9-17.

Tarboton, D.G., Bras, R.L. and Rodriguéz-Iturbe, I. 1991. On the extraction of channel networks from digital elevation data. *Hydrological Processes*. 5(1), 81-100.

Tucker, G.E., Lancaster, S.T., Gasparini, N.M., Bras, R.L. and Rybarczyk, S.M. 2001. An object-oriented framework for distributed hydrologic and geomorphologic modeling using triangulated irregular networks. *Computers & Geosciences*. 27(8), 959-973.

Tsai, V.J.D. 1993. Delaunay triangulations in TIN creation: an overview and a linear-time algorithm. *International Journal of Geographical Information Systems*. 7(6), 501-524.

Valeo, C. and Moin, S.M.A. 2000. Grid-resolution effects on a model for integrating urban and rural areas. *Hydrological Processes*. 14, 2505-2525.

Vázquez, R.F., Feyen, L., Feyen, J. and Refsgaard, J.C. 2002. Effect of grid size on effective parameters and model performance. *Hydrological Processes*. 16, 355- 372.

Vieux, B.E. 1993. DEM aggregation and smoothing effects on surface runoff modeling. *Journal of Computing in Civil Engineering*. 7(3), 310-338.

Vivoni, E.R., Ivanov, V.Y., Bras, R.L. and Entekhabi, D. 2002. Topography, triangular irregular networks and hydrological similarity. *Journal of Hydrologic Engineering*. (Accepted).

Vivoni, E.R., Entekhabi, D., Bras, R.L., Ivanov, V.Y., Van Horne, M.P., Grassotti, C. and Hoffman, R.N. 2003a. Space-time predictability of hydrometeorological flood events. Submitted to *Journal of Hydrometeorology*.

Vivoni, E.R., Entekhabi, D., Bras, R.L. and Ivanov, V.Y. 2003b. Coupled surface-subsurface response to rainfall: Nonlinearity and scale-dependence. Submitted to *Water Resources Research.*

Vivoni, E.R., Teles, V.T., Ivanov, V.Y., Bras, R.L. and Entekhabi, D. 2003c. Embedding landscape processes into triangulated terrain models. Submitted to *International Journal of Geographical Information Science.*

Watson, D.F. and Philip, G.M. 1984. Systematic triangulations. *Computer Vision, Graphics, and Image Processing*. 26, 217-223.

Walker, J.P. and Willgoose, G.R. 1999. On the effect of digital model accuracy on hydrology and geomorphology. *Water Resources Research*. 35(7), 2259-2268.

Wigmosta, M.S., Vail, L.W. and Lettenmaier, D.P. 1994. A distributed hydrology-vegetation model for complex terrain. *Water Resources Research*. 30(6), 1665-1679.

Wolock, D.M. and McCabe, G.J. 2000. Differences in topographic characteristics computed from 100- and 1000-m resolution digital elevation model data. *Hydrological Processes*. 14, 987-1002.

Wolock, D.M. and Price, C.V. 1994. Effects of digital elevation model map scale and data resolution on a topography-based watershed model. *Water Resources Research*. 30(11), 3041-3052.

Wood, E.F., Sivapalan, M. and Beven, K. 1990. Similarity and scale in catchment storm response. *Reviews of Geophysics*. 28(1), 1-18.

Wood, E.F., Lettenmaeir, D., Liang, X., Nijssen, B. and Wetzel, S.W. 1997. Hydrologic modeling of continental-scale basins. *Annual Reviews of Earth and Planetary Sciences*. 25, 279-300.

Xevi, E., Christiaens, K., Espino, A., Sewnandan, W., Mallants, D., Sorensen, H. and Feyen, J. 1997. Calibration, validation and sensitivity analysis of the MIKE-SHE model using the Neuenkirchen catchment as a case study. *Water Resources Management*. 11, 219-242.

Zhang, W. and Montgomery, D.R. 1994. Digital elevation model grid size, landscape representation, and hydrologic simulations. *Water Resources Research*. 30(4), 1019-1028.

Chapter 5:

Space-time Predictability of Hydrometeorological Flood Events

5.1 Introduction

Hydrologic prediction using distributed modeling remains a fundamental problem in hydrometeorology. Uncertainty about future rainfall events limits our ability to extend flood lead time despite advances in hydrologic modeling (*e.g.*, Singh and Woolhiser, 2002). Approaches to rainfall prediction are currently limited by the forecast space and time scales of interest, as well as available meteorological data and models. For example, Browning and Collier (1989) discuss the performance of various forecasting strategies as a function of lead time. Despite progress, issuing quantitative precipitation forecasts (QPFs) is still among the most difficult challenges in hydrometeorology (Ganguly and Bras, 2002). The challenge increases when rainfall forecasts are to be used to predict flooding with distributed hydrologic models (DHMs) that are sensitive to the temporal and spatial distribution of rainfall (*e.g.*, Pessoa *et al.*, 1993, Bell and Moore, 2000).

The primary objective for utilizing QPFs in hydrometeorology is to increase the lead time for issuing flood warnings. In real-time operation, hydrologic models must incorporate precipitation forecasts to avoid assuming negligible future rainfall (Collier, 1991). In the absence of forecasts, the maximum lead time for flood warning is the basin response time. Rain estimates from radars, satellite sensors and models (Droegemeier *et al.*, 2000) may allow extrapolating rainfall to increase hydrologic predictability (Yates *et al.*, 2000, Smith and Austin, 2000). Although limited to short times, radar extrapolation

models have demonstrated forecast skill in meteorological applications (*e.g.*, Dixon and Weiner, 1993, Wolfson *et al.*, 1999). In this chapter, nowcasting QPFs are used to drive a spatially-explicit flood forecasting tool calibrated for the catchment of interest.

Distributed hydrologic models offer distinct advantages over lumped models used widely for flood forecasting (Garrote and Bras, 1995, Ivanov *et al.*, 2003). In recent years, there has been a significant improvement in the inputs to physically-based DHMs, including digital elevation models (DEMs), land-surface maps and hydrometeorological data (ASCE, 1999). In distributed models, basin runoff response can vary according to the temporal and spatial variability in rainfall and surface properties. This capability permits simulating basin conditions traditionally excluded from operational forecasts, including discharge forecasts at internal stream gauging stations. In addition, the increased model sensitivity to rainfall forcing can be used to critically evaluate the QPF performance. Benoit *et al.* (2000), for example, demonstrated the hydrologic verification of an atmospheric model with a distributed flood forecast.

In this chapter, we evaluate the combined use of a radar extrapolation model and a distributed hydrologic model to assess the limits of flood predictability by quantifying forecast performance as a function of lead time and catchment scale. We also address the impact of spatial rainfall variability and storm evolution on the performance of the combined models. The approach takes advantage of an operational radar network as well as high-resolution land-surface data for parameterizing, calibrating and forcing the distributed model. In previous studies, the hydrologic model forced with radar data has reproduced discharge observations and provided insights on the basin dynamics for the study area (Ivanov *et al.*, 2003). Here, we simulate the real-time operation of the

hydrologic model by introducing rainfall forecasts during storm evolution. Comparisons to observation-driven flood hindcasts and flow measurements serve to quantify the distributed quantitative flood forecast (dQFF) skill.

5.2 Model description

In this chapter, we use the Storm Tracker Nowcasting Model (STNM) (Chornoboy *et al.*, 1994, Wolfson *et al.*, 1999) to generate radar rainfall forecasts over the Arkansas-Red Basin (ABRFC; ~500 000 km^2). The STNM algorithm produces high resolution forecasts for short lead times as forcing to the TIN-based Real-time Integrated Basin Simulator (tRIBS) (Ivanov *et al.*, 2003). Applied to an operational-scale watershed (~800 km^2), the tRIBS model generates multiple-gauge flood forecasts in various modes.

5.2.1 STNM nowcasting model

Precipitation nowcasting can be defined as the production of short-range forecasts using extrapolation methods and observed rainfall fields from ground-based radars, rain gauges or satellite observations (*e.g.*, Dixon and Weiner, 1993, Tsanis *et al.*, 2002, Hamill and Nehrkorn, 1993). One source of rainfall data is the NEXRAD radar (WSR-88D) network in the US, which provides frequent observations over large domains at a high spatial resolution (Young *et al.*, 2000). Although employed in many hydrologic studies (*e.g.*, Johnson *et al.*, 1997, Carpenter *et al.*, 2001), NEXRAD data has been infrequently used in combination with nowcasting algorithms for the purpose of short-term flood prediction. Pereira Fo *et al.* (1999) and Yates *et al.* (2000) have shown the feasibility of this approach using lumped and semi-distributed hydrologic models. Results

from these studies showed that radar nowcasting provides more accurate rainfall forecasts as compared to numerical weather prediction models at short lead-times.

The STNM was originally designed for 0 to 1 hour radar reflectivity prediction in aviation applications (Wolfson *et al.*, 1999). It is distinguished by its ability to separate the storm envelope motion from embedded convective activity through the use of a scale separation filter. The model utilizes the cross-correlation of successive filtered images to generate large-scale motion vectors applied to the original multiscale field. Recently, Van Horne *et al.* (2003) evaluated the algorithm for radar rainfall forecasting over the ABRFC. Results show that the STNM model has skill in predicting high temporal (0.25 to 1 h) and spatial resolution (2 to 4 km) rainfall from the radar network, especially for linear, organized events driven by large-scale forcing. In this study, we assess nowcasting forecast skill through comparisons between flood forecasts and discharge measurements.

5.2.2 tRIBS distributed hydrologic model

The tRIBS model is a physically-based DHM developed for continuous flood forecasting using rainfall estimates from gauges or weather radar (Ivanov *et al.*, 2003). In addition, tRIBS also utilizes radar QPFs for real-time flood prediction. In an operational setting, available quantitative precipitation estimates (QPEs) are used up to the present time. Rainfall forecasts from radar nowcasting, meteorological models or hybrid methods can then be used as forcing up to a specified lead time (Grassotti *et al.*, 2002). The intensity, pattern and timing of the QPF over the basin are integrated into a flood discharge delayed by the basin response time. We evaluate the resulting dQFFs by comparing them to those produced by a QPE-driven model run. The transformation of

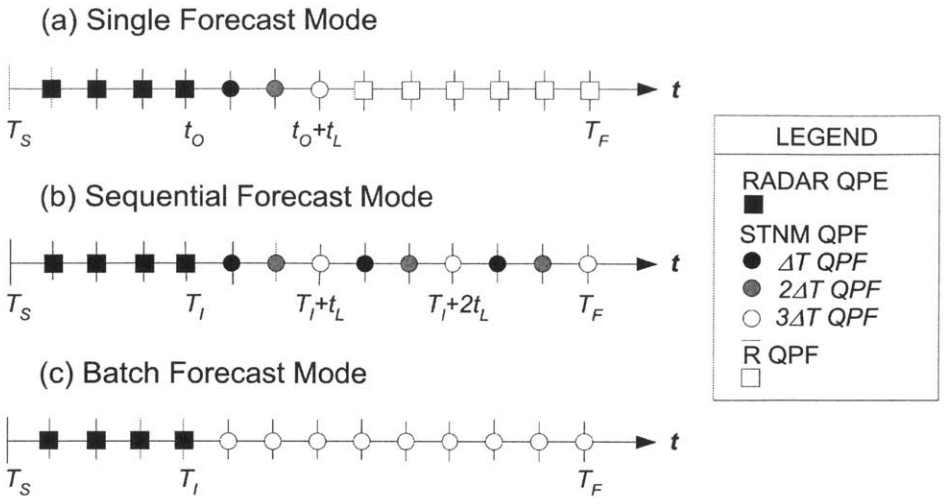

Figure 5.1. Rainfall-flood forecasting modes with lengths $t_L = 3\Delta T$. (a) Single forecasts. (b) Sequential forecasts. (c) Batch forecasts.

rainfall forecast skill to flood predictability as a function of lead time and basin scale can be explicitly quantified using this approach.

5.3 Real-time rainfall and flood forecasting

The combined rainfall and flood forecasting is illustrated in a simulated real-time setting utilizing three modes of operation: *single*, *sequential* and *batch* (Figure 5.1). In the forecast experiments, we examine the hydrologic model response to various rainfall specifications. Rainfall inputs to the hydrologic model are gridded fields (QPEs or QPFs) at regular intervals (ΔT) during the period, defined by a starting time (T_S) and a final time (T_F). The hydrological simulations cover the entire time (t) interval:

$$T_S \leq t \leq T_F , \tag{5.1}$$

while the rainfall forecasts extend between the forecast origin (t_O) and T_F (Figure 5.1). For each storm, the onset of rainfall (T_I) occurs sufficiently after T_S so that the hydrological model has established a steady baseflow prior to the flood event. For each

mode, the radar QPEs are used in the hydrologic model until the start of the rainfall forecast (t_O) after which the STNM nowcasting or persistence QPFs are utilized, either as a distributed rainfall field or as a mean areal precipitation (MAP) value. A persistence forecast is generated in each mode by replacing the QPF with the last available QPE. In each experiment, the STNM or persistence forecast length is denoted by a lead time (t_L).

5.3.1 Single Forecasts

In the single mode, the QPE at $t_O \geq T_I$ is extrapolated to produce forecasts over the lead time t_L (Figure 5.1a). In real-time operation, the tRIBS model can be forced with radar QPEs up to t_O and with STNM (or persistence) QPFs over the interval:

$$t_O \leq t \leq t_O + t_L . \tag{5.2}$$

For all $t > t_O + t_L$, a spatio-temporal mean rainfall during the storm event is used until the end of the flood forecast period (T_F):

$$\overline{R} = \frac{1}{A}\int_A \left[\frac{1}{t_O}\int_0^{t_O} R(x,y,\tau)d\tau \right] dA , \tag{5.3}$$

where A is the basin area (km^2) and $R(x,y,\tau)$ is the time-varying rainfall field (mm h^{-1}) observed up to t_O. By taking storm history into account, $\overline{R}$ is an improvement over zero or climatology rain values used to extend flood forecasts (*e.g.*, Mecklenburg *et al.*, 2000).

A single flood forecast can be issued for each radar observation during a storm. For nowcasting models, rainfall forecast skill varies with the storm evolution during the forecast period. In the hydrology model, single forecasts issued at different origins should produce variations in the flood prediction. Testing this variability illustrates the effect of storm evolution on flood predictability when using the single forecast mode.

5.3.2 Sequential Forecasts

Although single forecasts have shown promise (*e.g.*, Cluckie and Owens, 1987), flood forecast skill can be improved by using a sequence of radar QPFs after $t_O = T_I$. In the sequential mode (Figure 5.1b), the STNM (or persistence) forecasts made using QPEs up to and including T_I are used for the interval:

$$T_I < t \leq T_I + t_L . \tag{5.4}$$

The forecasts using QPEs up to $T_I + t_L$ are then used for the next time interval:

$$T_I + t_L < t \leq T_I + 2t_L , \tag{5.5}$$

and the updating process is repeated until T_F. The tRIBS model is initially forced with QPEs prior to T_I. During the forecast interval, a sequence of multi-step ahead forecasts (*e.g.* 0, ΔT and $2\Delta T$ lead time from T_I) is constructed for each time t_L interval based on all previous QPEs. This technique updates the STNM model at a marching t_L and can be applied over T_I to T_F, eliminating the need for the spatial-temporal mean rainfall.

The sequential mode emulates the real-time operation of the forecasting system by using multiple radar images. The resulting QPFs are a temporal interpolation of the radar QPEs using a mixture of forecasts of different skill. Increasing t_L should result in a decrease in skill as the extrapolation may not properly represent storm dynamics.

5.3.3 Batch Forecasts

An alternative to the sequential mode is more appropriate when continuous flood forecasts are required at a specific lead time (t_L). In the batch forecast mode, a series of QPFs of equal t_L (all ΔT lead time forecasts) are used to force the hydrology model during the forecast interval (T_I to T_F) (Figure 5.1c). This technique utilizes the STNM model to provide a series of single step-ahead forecasts that are appropriate when the

radar temporal resolution is high. For the shortest lead time, the sequential and batch forecast modes are equivalent except at t_O where the sequential mode uses a QPE. Increasing t_L should decrease flood forecast skill as the group of QPFs are longer extrapolations of the observed rain patterns. Figure 5.1 illustrates the three modes (single, sequential, batch) for the case $t_L = 3\Delta T$. Note the sequential mode is mixture of QPFs of varying length (multi-step), while the batch mode is a collection of forecasts of equal length (single step).

5.3.4 Performance metrics

Model performance is assessed using four metrics to compare observations (O) and forecasts (F) of discharge ($m^3\ s^{-1}$): correlation coefficient (CC), efficiency coefficient (E), bias (B), and mean absolute error (MAE). The correlation coefficient is:

$$CC = \frac{\sum_{i=1}^{N}\left(O_i - \overline{O}\right)\left(F_i - \overline{F}\right)}{\left(\sum_{i=1}^{N}\left(O_i - \overline{O}\right)^2\right)^{0.5}\left(\sum_{i=1}^{N}\left(F_i - \overline{F}\right)^2\right)^{0.5}}, \tag{5.6}$$

where the overbar denotes a mean value, measures the linear relationship between forecasts and observations (Grecu and Krajewski, 2000). The efficiency improves upon CC for model evaluation purpose (Legates and McCabe, 1999) and is computed as:

$$E = 1 - \frac{\sum_{i=1}^{N}\left(O_i - F_i\right)^2}{\sum_{i=1}^{N}\left(O_i - \overline{O}\right)^2}. \tag{5.7}$$

E varies from $-\infty$ to 1, with larger values indicating improved performance and $E \leq 0$ implying the observed mean is as good as or better than the forecasts. The dimensionless bias (B) measures the correspondence between the mean observations and forecasts:

Basin	USGS Gauge	A (km^2)	h (m)	μ (m)	σ (m)	L (km)	S ($m\ km^{-1}$)	Land Use[a] (%)	Soils[b] (%)
BF	07197000	808.15	213.71	346.54	59.02	67.26	5.47	52.2, 46.3, 1.3	94, 6
DM	07196900	106.87	300.68	408.07	57.44	18.64	13.41	44.3, 54.1, 1.5	78, 22
PC	07196973	63.87	244.36	327.63	28.08	19.90	9.26	41.7, 57.7, 0.7	100, 0

Table 5.1. Characteristics of the nested watersheds. A is the basin area (km^2); h is the gauge elevation (m); μ is the DEM mean elevation (m); σ is the DEM standard deviation (m); L is the maximum outlet distance (km); S is the relief ratio ($\Delta z\ L^{-1}$ in m km^{-1}). (a) The land use categories are forest, grassland, urban (% area). (b) The soils texture categories are silt loam and fine sandy loam (% area).

$$B = \frac{\overline{F}}{\overline{O}}, \tag{5.8}$$

defined following Grecu and Krajewski (2000). The *MAE* describes the absolute difference between the observations and forecasts without emphasizing the value of outliers (Legates and McCabe, 1999):

$$MAE = \frac{1}{N}\sum_{i=1}^{N}\left|O_i - F_i\right|. \tag{5.9}$$

We assess model performance by comparing forecasts with QPE-driven flood predictions taken as ground truth. Furthermore, the skill metrics are used to determine flood predictability as function of spatial and temporal scale.

5.4 Application

Quantitative flood forecasts using the STNM and tRIBS models are presented for two storm events over the ABRFC utilizing the forecast modes previously discussed. In the following, we describe the hydrometeorological events as well as the data used to parameterize, force and verify the hydrologic model.

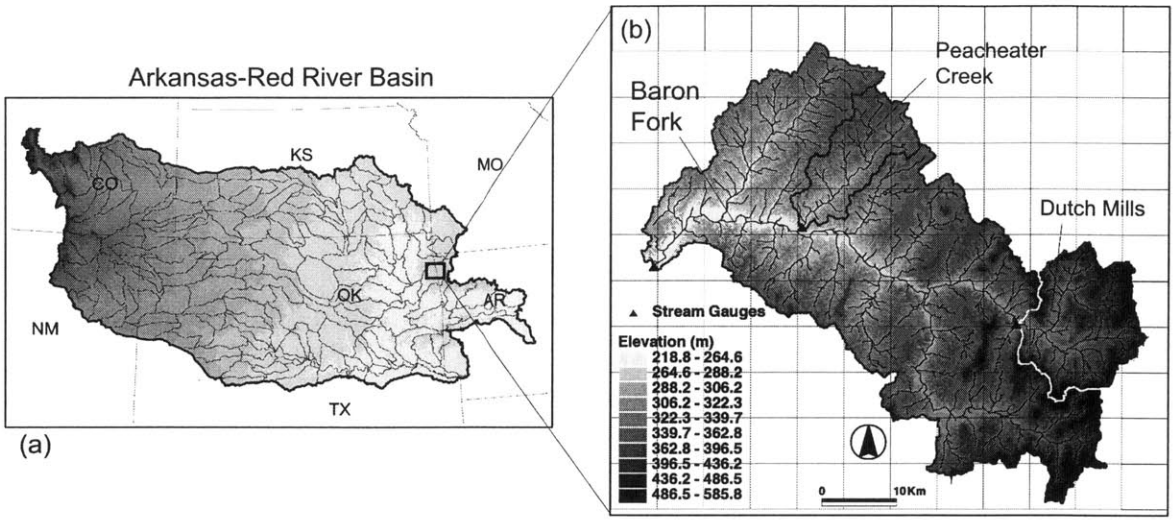

Figure 5.2. Location of the study area. (a) Arkansas Red-River basin topographic data and interior basins. (b) Baron Fork topographic representation including stream network, discharge gauging stations and outlines of NEXRAD 4-km radar grid cells.

5.4.1 Study area

The tRIBS model is applied to the Baron Fork at Eldon, OK (BF) and two sub-basins, the Peacheater Creek at Christie, OK (PC) and Baron Fork at Dutch Mills, AR (DM) (Table 5.1). Figure 5.2a illustrates the nested basins in relation to the ABRFC domain. Topography is derived from a USGS 30-m DEM using the hydrographic TIN procedure described in Vivoni *et al.* (2002) (Figure 5.2b). Given its location in the Ozark Plateau, parts of the basin are rugged while others are gently sloping. Since terrain variability is high, triangular elements in the TIN vary in area from 0.13 m^2 to 0.60 km^2.

The Baron Fork is characterized by a mixed land use of deciduous and evergreen forest (52.2%); croplands and orchards (46.3%); and small towns (1.3%). The surface soil texture is primarily silt loam (94%) and fine sandy loam (6%). The river network has a maximum length of 67.3 km and a mean drainage density of 0.86 km^{-1}. Various studies have focused on the Baron Fork due to its unregulated nature, high stream gauge density and a long time series of radar data (*e.g.*, Johnson *et al.*, 1997, Carpenter *et al.*, 2001).

5.4.2 Radar rainfall data

In this study, we utilize two radar products over the ABRFC, the NEXRAD Stage III/P1 and the proprietary Weather Services International (WSI) NOWrad data. Although both are based on NEXRAD, they differ in the algorithms used to correct, merge and convert reflectivity to rainfall. Young *et al.* (2000) describe the methodologies used to derive the Stage III/P1 data. In a recent study, Grassotti *et al.* (2003) showed the products compared well at mutiple time scales. The focus in this chapter is on the WSI data since it is available at a higher resolution (2-km, 15-min) than Stage III/P1 (4-km, 1-h).

Radar rainfall estimates are mapped to the Hydrologic Rainfall Analysis Project grid, transformed to UTM coordinates and extracted using the basin boundary (Figure 5.2). At the basin scale, there are 72, 13 and 10 radar cells (4 × 4-km) over the BF, DM and PC basins, respectively. Three overlapping radars in proximity to the basin (Slatington Mountain: 50 km, Tulsa: 69 km, and Springfield: 168 km) provide comprehensive radar coverage. Despite abundant observations, intercomparison studies have highlighted the limitations and potential radar errors over this region (*e.g.*, Smith *et al.*, 1996, Grassotti *et al.*, 2003).

5.4.3 Hydrometeorological flood events

Two storm periods in 1998 were selected for evaluating the combined forecasts. Criteria for selection included: (1) availability of radar data, (2) significant flooding, and (3) varying storm characteristics. The two events exhibit linear, frontal (*i.e.*, mesoscale) organization making them amenable to the nowcasting model (Van Horne *et al.*, 2003). The storms either caused flooding exceeding the regulatory limits at BF (563.5 $m^3 s^{-1}$) or DM (283.4 $m^3 s^{-1}$) or constituted the annual basin flood (USCoE Tulsa District, 2002).

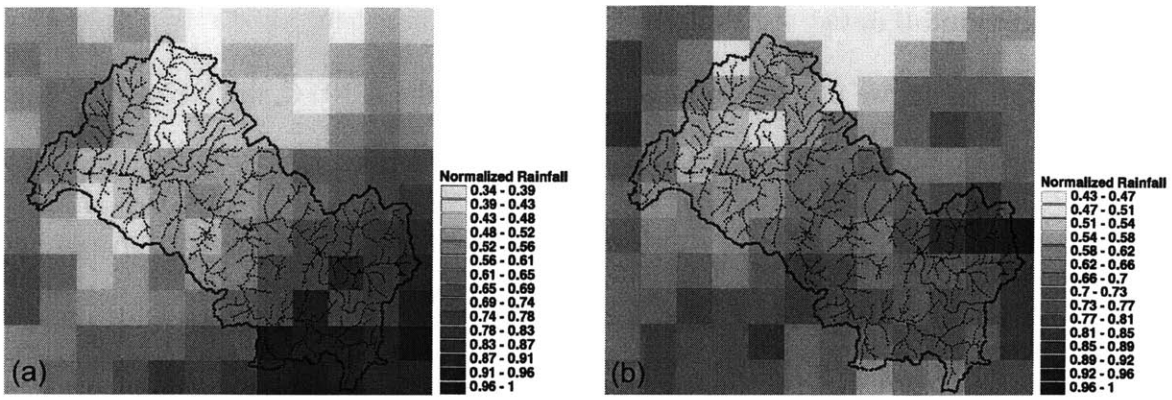

Figure 5.3. Spatial distribution of normalized total rainfall. Normalization is performed with the maximum radar value shown in parenthesis. (a) Jan 1998 (163.27 mm). (b) Oct 1998 (152.16 mm).

Period	D (h)	I_{15} (mm h^{-1})	P_T (mm)	R_T (mm)	ϕ (–)	Q_p (m^3 s^{-1})	t_B (h)	t_R (y)
4-13 Jan 1998	30.5	52.02	98.51	117.86	1.20	893.93	13.25	6.75
5-8 Oct 1998	20.0	36.66	83.17	20.13	0.24	273.85	15.25	1.43

Table 5.2. Storm characteristics. D is the rainfall duration (h); I_{15} is the maximum 15-min intensity at any radar cell (mm h^{-1}); P_T is the total basin-averaged rainfall (mm); R_T is the total runoff (mm); ϕ is the runoff ratio (P_T/R_T); Q_p is the observed peak discharge (m^3 s^{-1}); t_B is the basin lag-time (h); t_R is the estimated return period (y).

5.4.3.1 January 4-8 1998

This hydrometeorological event was connected with a major intrusion of arctic air into the Southern Plains. Precipitation began as an unorganized event and then formed into a slow-moving frontal storm. Over the Baron Fork, this long-duration storm brought significant amounts of rainfall (Table 5.2). The storm moved from west to east oriented in a north-east to south-west direction. The spatial rainfall variability illustrates a gradient in accumulation with higher rainfall in the southeast corner (Figure 5.3a). Basin response to the storm was pronounced, with 894, 492 and 62 m^3 s^{-1} in discharge recorded at the BF, DM and PC gauges, respectively (Figure 5.4a). The flood response is of high magnitude

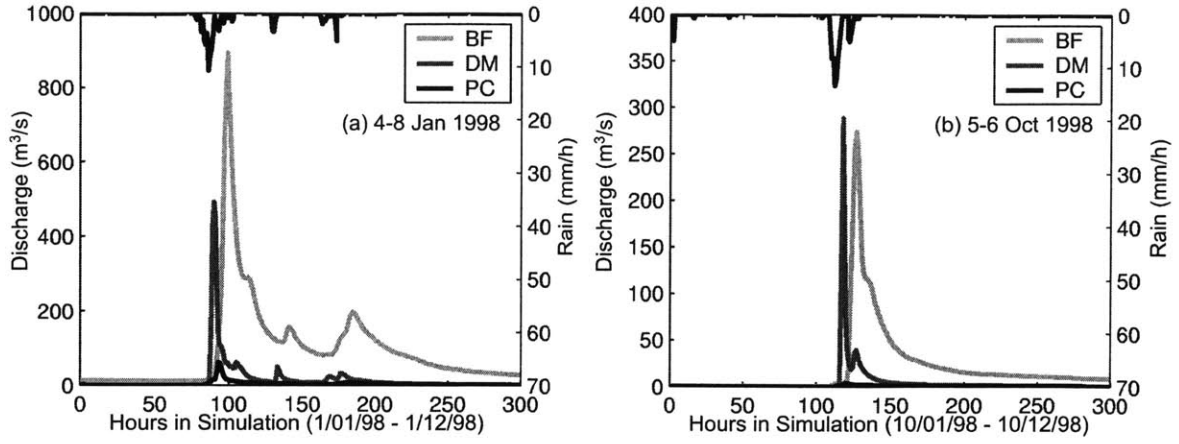

Figure 5.4. Observed mean areal rainfall over Baron Fork and USGS discharge for each gauged basin. (a) Jan 1998. (b) Oct 1998.

in relation to historical peak measurements (Figure 5.5). In addition, the basin lag time is relatively short (13 hours), suggesting the predominance of an overland flow response.

5.4.3.2 October 5-6 1998

As a linear, highly-organized convective system, this event is characteristic of the fall storms in the region (Bradley and Smith, 1994). The storm initially developed as several convective cells and grew into a continuous, intense squall line moving eastward and oriented northeast to southwest. Over the Baron Fork, the rainfall intensity varied as the storm moved upstream along the main river axis during its 20 hour duration (Figure 5.3b). The high rainfall amounts over the northeast corner induced a variable response, resulting in a decaying flood wave downstream (Figure 5.4b). For the Baron Fork, the flood represents a 1.43 and 2.26 year return period at Eldon (274 $m^3 s^{-1}$) and Dutch Mills (289 $m^3 s^{-1}$), respectively (Figure 5.5). As compared to the January event, the flood had a longer lag time (15 hours) and lower runoff ratio in the basin (Table 5.2).

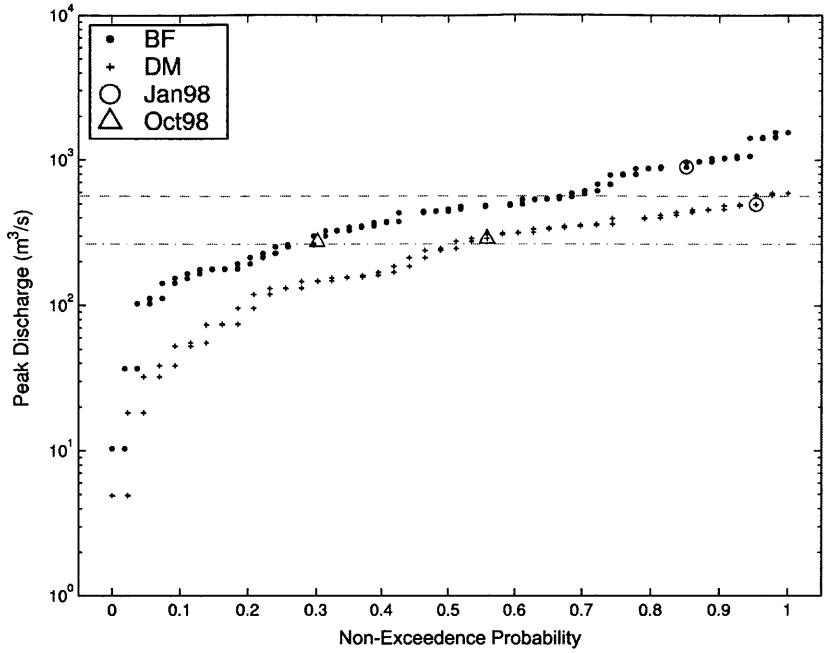

Figure 5.5. Sample flood frequency distribution based on annual peak observations from 1945-2001 (BF) and 1958-2001 (DM). The horizontal lines represent the U.S. Army Corps of Engineers regulatory flood limits at BF (dashed) and DM (dashed-dot).

5.4.4 Model calibration and hydrologic response

The tRIBS model was calibrated separately for each storm using the multiple-gauge observations. Treating each period individually is justified based on the differences in flood response, in particular the runoff ratio and lag time. A nested calibration was followed where the parameters of each sub-basin were modified prior to calibrating the overall response. Initial parameter estimates were based on relationships to soils and vegetation, while the calibration strategy at each basin follows Ivanov *et al.* (2003). The initial water table distribution was obtained using the pre-storm baseflow and topographic distribution (*e.g.*, Ivanov *et al.*, 2003). To reduce groundwater initialization errors, a dry spin-up period was allowed before the simulation of each flood event.

Figure 5.6 presents the calibrated tRIBS model response to WSI radar rainfall (4-km, 15-min) for the two flood events. In addition to rainfall, surface meteorological data

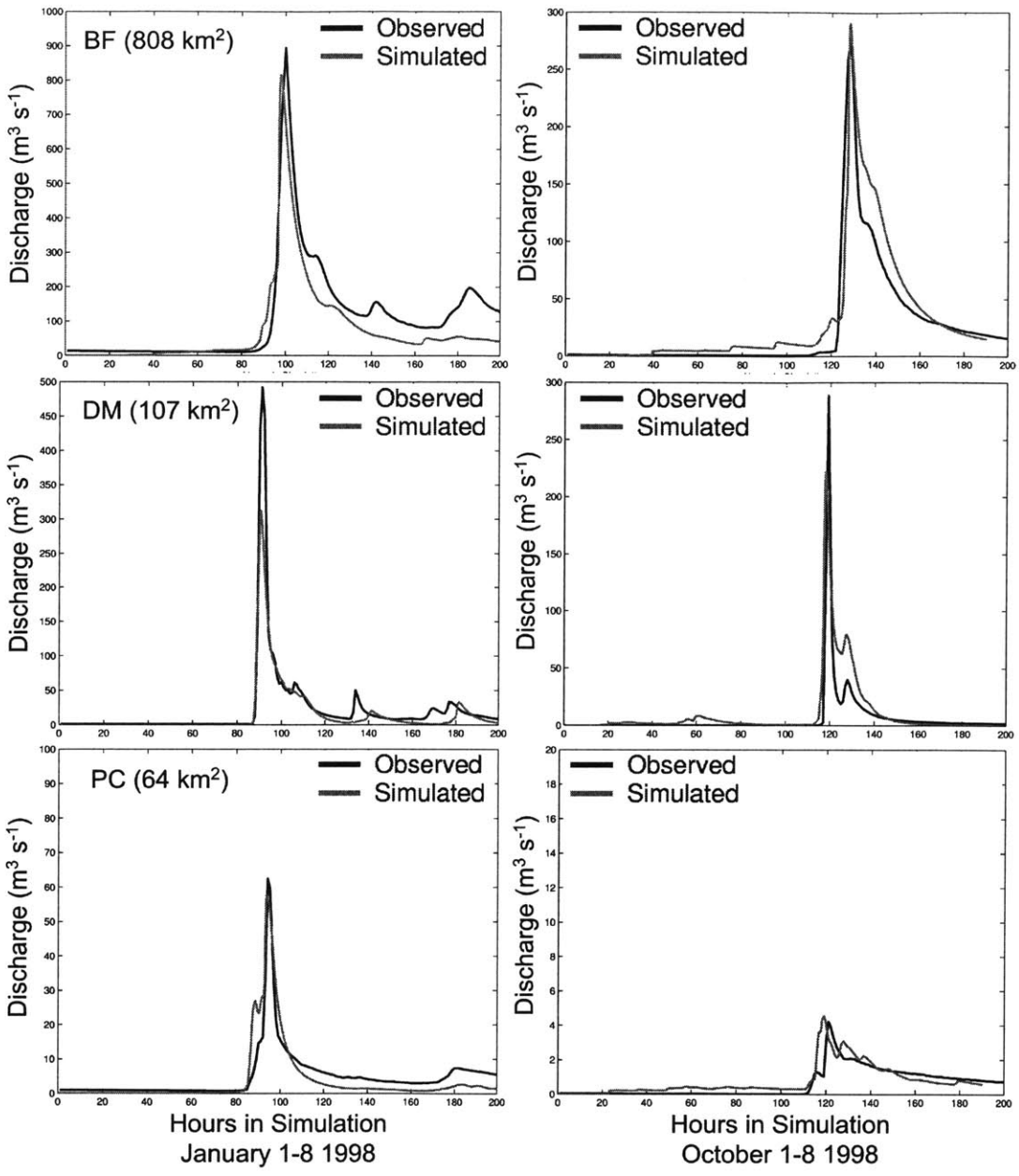

Figure 5.6. Comparison of the observed and simulated hydrographs for the two events: Jan 1998 (left), Oct 1998 (right), and three gauges: BF (top), DM (middle) and PC (bottom).

are used to drive the radiation and energy balance in the model. The calibrated model adequately reproduces the flood events as compared to observations. Minor discrepancies in peak discharge and time to peak within the sub-basins may be due to inaccuracies in the radar estimates, discharge data or calibration parameters. Overall, the multi-gauge

Basin	A (km^2)	L (km)	S (m km^{-1})	D_d (km^{-1})	t_c (h)
1	108.23	25.73	6.06	0.9895	5.78
2	1.41	2.59	34.01	0.8264	0.51
3	2.67	4.52	21.44	0.7701	0.93
4	12.14	8.06	14.94	0.8059	1.67
5#	65.06	19.90	9.26	0.8293	4.03
6	610.60	50.33	6.81	0.8355	9.26
7	450.26	40.01	8.11	0.8352	7.25
8	365.25	35.03	9.09	0.8209	6.27
9	182.91	29.78	9.49	0.8230	5.44
10*	106.91	18.64	13.41	0.8370	3.32
11	49.07	12.72	19.10	0.8692	2.16
12	21.18	9.03	24.92	0.8700	1.50
13	4.29	3.53	51.27	0.7720	0.55
14	0.78	1.33	112.77	0.3033	0.19
15+	808.39	67.26	5.47	0.8630	12.59

Table 5.3. Sub-basin characteristics. A is the basin area (km^2); L is the maximum sub-basin outlet distance (km); S is the relief ratio (m km^{-1}); D_d is the drainage density (km^{-1}); t_c is the time of concentration (h) from Kiprich (1940): $t_c = 0.000325\ L^{0.77}S^{-0.385}$, where units are L (m) and S (m m^{-1}).

calibration provides confidence in the distributed model and its capability for predicting streamflow in the ungauged interior basins described in Table 5.3.

5.5 Results

Results from the combined models are illustrated through comparisons between the dQFFs and the QPE-driven model response. A discussion of the results using Stage III/P1 data for October 1998 has been presented in Vivoni *et al.* (2003). Here, we focus on the forecast performance as a function of basin scale and lead time for the WSI data.

5.5.1 Performance of Coupled Rainfall-Runoff Forecast Modes

5.5.1.1 Single Forecast Mode

Performance of a single STNM QPF as forcing to the tRIBS model is evaluated at various forecast origins (t_O) for the two storm events. Rainfall forecasts up to t_L = 12 h

were issued at seven consecutive hourly intervals. The forecast origins were chosen during the storm rising limb, spanning 1100 to 1700 UTC on 4 January 1998 and 1200 to 1800 UTC on 5 October 1998. The 12-h STNM forecasts (t_O to $t_O + t_L$) were combined with the spatio-temporal mean rainfall ($t_O + t_L$ to T_F) to produce 30-h flood forecasts at the stream gauges and multiple interior catchments (Table 5.3).

The performance of the single QPFs is highly sensitive to the selection of t_O as shown in Figure 5.7 for the October event. In Figure 5.7a, the cumulative rainfall is normalized by the observed storm total rain. Deviations from the QPE (108-140th hour) depend on storm evolution, with the QPFs underestimating rain for early t_O during storm growth (1200-1500 UTC) and overestimating the QPE during the decay phase (1600-1700 UTC). After the storm passes (1800 UTC), the QPF approaches the observed value. Discrepancies in the rain forecast translate to deviations in the QPF-driven floods. In Figures 5.7b-d, the cumulative discharge, normalized by the QPE-driven flood volume, is shown for the gauged basins. The flood forecast variability with respect to t_O follows the description for the QPFs. Similar sensitivity to t_O was obtained for the January event.

5.5.1.2 Sequential Forecast Mode

Despite demonstrating skill, the dependence on forecast time is a strong argument against the single forecast mode. Determining an optimal t_O may not be feasible as the forecasted rain can deviate quickly from observations. Alternatively, the nowcasting method can be updated with new observations as these become available from the radar network. For the sequential scheme, QPEs are ingested into the STNM at every t_L interval during the storm evolution. Sequential forecast performance is evaluated for the entire storm period, thus avoiding forecast dependence on the specified forecast origin.

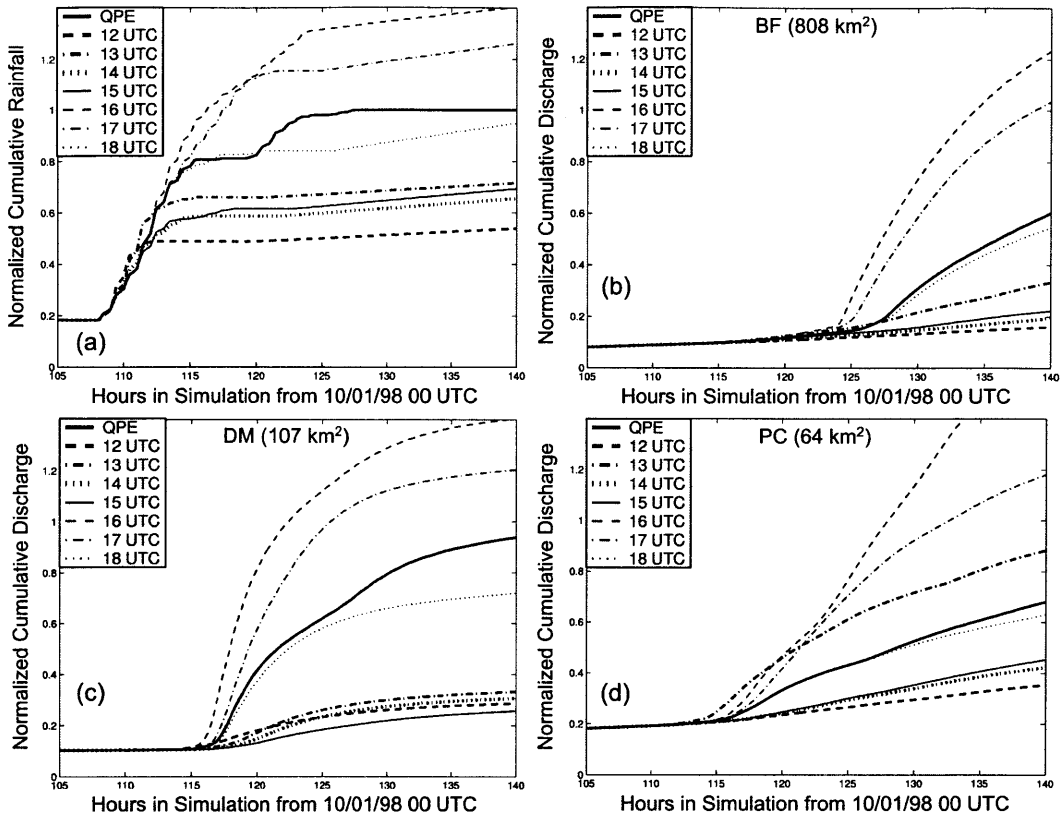

Figure 5.7. Single forecast performance for the October event at different origins (1200 to 1800 UTC). (a) Normalized cumulative basin rainfall. Normalized cumulative discharge at BF (b), DM (c) and PC (d). Thick solid line represents the QPE-driven model run.

As t_L is increased from 0.25 to 3-h (ΔT = 15-min), the sequence of STNM QPFs is used to interpolate additional time between the QPEs. Therefore, flood forecast skill is expected to decrease with lead time. Figure 5.8 shows the normalized cumulative rainfall and discharge for a series of sequential QPFs of varying t_L. Comparisons are made to the QPE-driven run for the October event (96-140th hour). For lead times less than 60-min, the rainfall and flood forecast cluster near the QPE run (Figures 5.8a-8d). Once one hour is passed, the sequential QPFs generally become worse, although rainfall overestimation leads to improved behavior at large t_L for the DM sub-basin (Figure 5.8c). Sequential forecasting is significantly better than the single mode, as storm evolution is updated

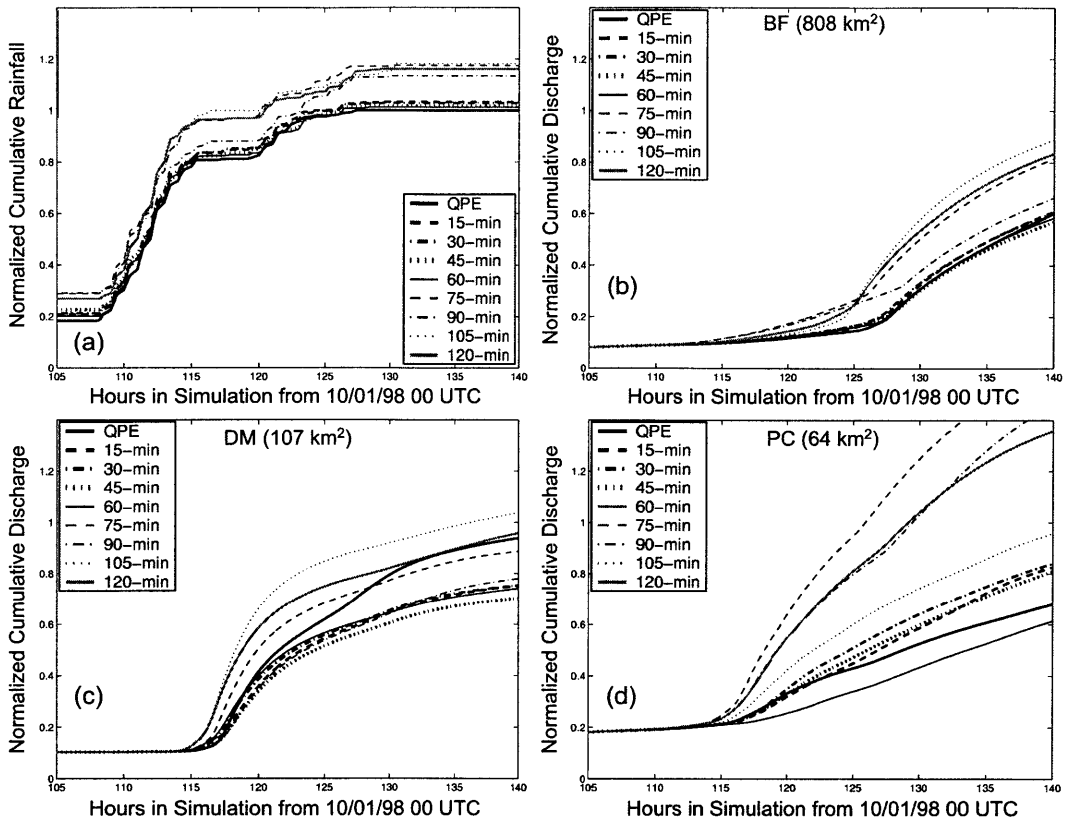

Figure 5.8. Sequential forecast performance for the October event. Forecasts with lead times from 15-120-min are compared to the QPE run for (a) normalized cumulative basin rainfall and normalized cumulative discharge at BF (b), DM (c) and PC (d).

explicitly via observations. Comparisons of Figures 5.7 and 5.8 demonstrate the forecast enhancement. Through the temporal interpolation of available QPEs, the sequential forecast enhances flood predictability up to lead times consistent with nowcasting skill.

5.5.1.3 Batch Forecast Mode

As an alternative to the sequential mode, the batch forecast scheme is used to issue single-step ahead forecasts of equal relative skill (t_L) from frequent observations (Figure 5.1c). The STNM and tRIBS models are evaluated in batch mode for the two storms by varying the lead time from 0.25 to 3-h in steps of 15-min. In Figure 5.9, the normalized cumulative rainfall and flood hydrographs are presented for the October

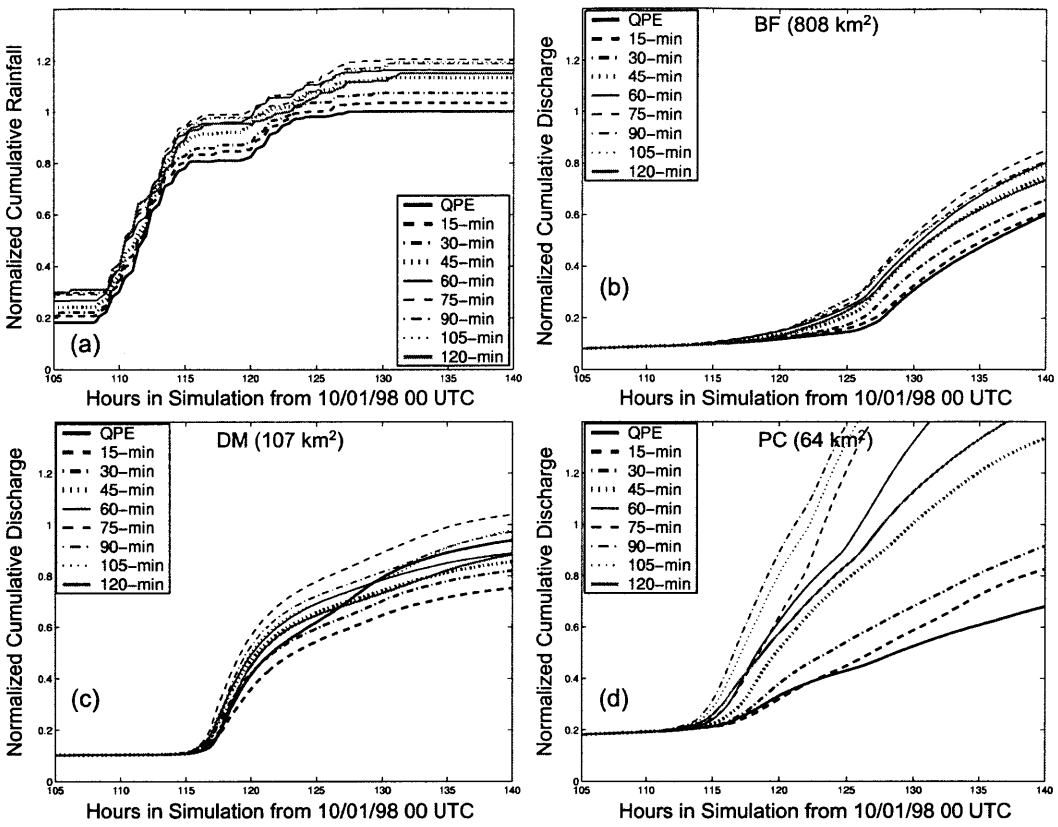

Figure 5.9. Same as Figure 5.8, but for the batch forecast mode.

storm. Note that the forecasted cumulative plots cluster close to the QPE-driven model results, as in the sequential mode, but that the variation with increasing lead time is smoother. Performance is also a function of the basin characteristics as seen from the variability among BF, DM and PC. Similar results were obtained for the January storm.

5.5.2 Temporal and Spatial Dependence of Multi-Gauge Hydrographs

5.5.2.1 Forecast Lead Time Dependence

The dependence of rainfall forecast skill on the lead time since the last available observation has been well documented (*e.g.*, Georgakakos, 1986, Pereira Fo *et al.*, 1999, Grecu and Krajewski, 2002). Van Horne *et al.* (2003), in particular, quantified the decrease in forecast skill of the STNM nowcasting model for the January and October

1998 events through the use of the critical success index (CSI) over the ABRFC. As lead time was increased from 0.25 to 2 hours, the CSI performance of the WSI-based STNM forecast decreased in comparison to the observed radar fields.

The decrease in rainfall skill with lead time should translate to a reduction in flood forecast skill with the combined STNM-tRIBS models. In order to test this, model runs in the sequential and batch modes were evaluated as a function of lead time. Figure 5.10 presents the lead time variation of *E*, *CC*, *B* and *MAE* for both events. These metrics compare the forecasted hydrograph to the QPE-driven simulation at the basin outlet. Note the marked change in skill (*E* and *CC* decrease, *B* and *MAE* increase) as t_L is increased beyond 1-h for the October event in the sequential mode. Although less striking for the January event, these results suggest that the rainfall lead time limits flood forecast skill. Similar results were obtained for the batch mode (see Figure 5.12), although a smoother variation with lead time is apparent. In general, the performance of the rainfall-flood forecasts is observed to be both lead time and storm dependent.

5.5.2.2 Catchment Scale Dependence

The dependence of forecast skill on catchment scale has received much less attention, in part due to the inability of lumped models to predict hydrographs at internal gauges. Most rainfall-runoff studies focus on a particular watershed without considering the variability in response with basin scale (*e.g.*, Mimikou and Baltas, 1996, Pereira Fo *et al.*, 1999, Yates *et al.*, 2000, Dolciné *et al.*, 2001). With the advent of radar data and distributed hydrologic models, it is feasible to address scaling issues in the context of flood forecasting. The identification of a particular basin scale above or below which the forecast skill is invariant would be useful forecasting knowledge.

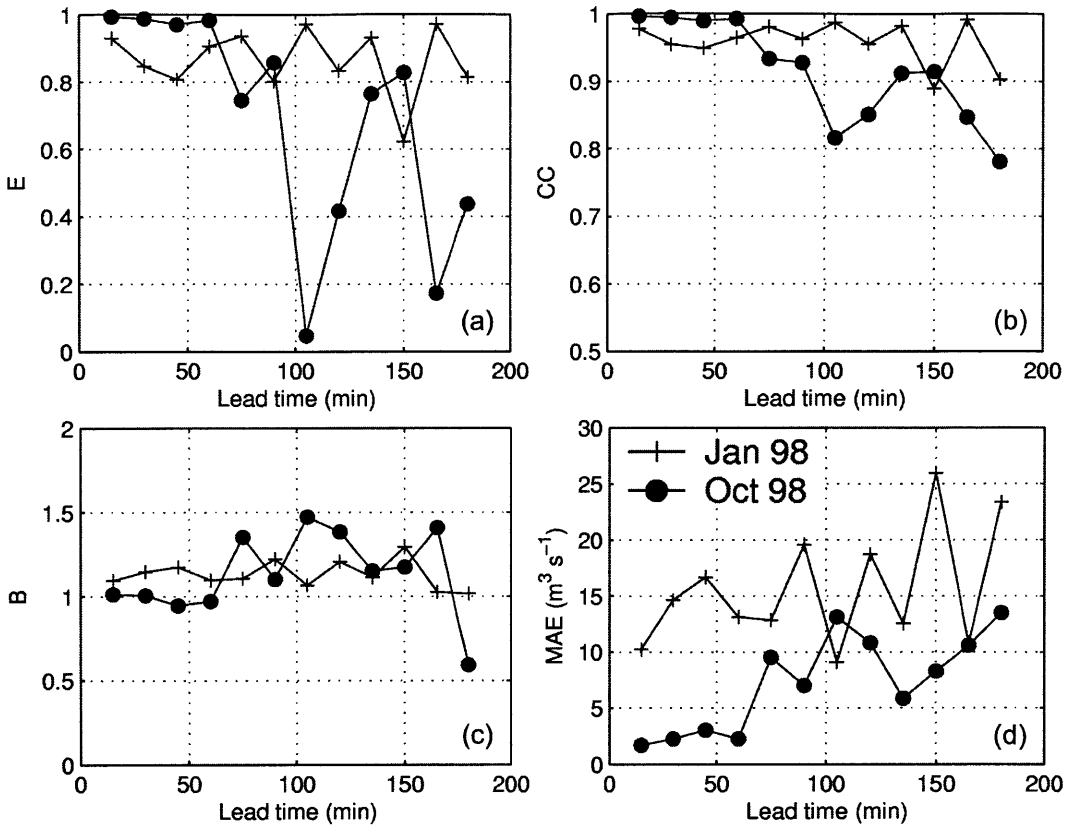

Figure 5.10. Flood forecast skill as a function of lead time for the sequential mode at BF. (a) Efficiency, (b) Correlation coefficient, (c) Bias (*B*) and (d) Mean absolute error

To test dependence on spatial scale, model runs were evaluated as a function of basin area. The interior basins in Table 5.3 represent a range of physiographic properties including a difference in area (*A*) of three orders of magnitude (0.8 to 800 km^2). For the sequential mode at a lead time of 1-h, Figure 5.11 presents the variation of skill (*E*, *CC*, *B* and *MAE*) with area for both events. Note the difference in skill as *A* is increased beyond 200 km^2. For smaller areas, values of *E*, *CC* and *B* vary considerably. Both *E* and *CC* stabilize to values near 0.9, while *B* fluctuates around unity after $A \sim 200$ km^2. The *MAE* behaves differently as it can increase or decrease with area. Similar results were obtained for the batch mode. In general, the metrics (*E*, *CC* and *B*) show a spatial dependence in forecast skill with an identified threshold beyond which performance is similar.

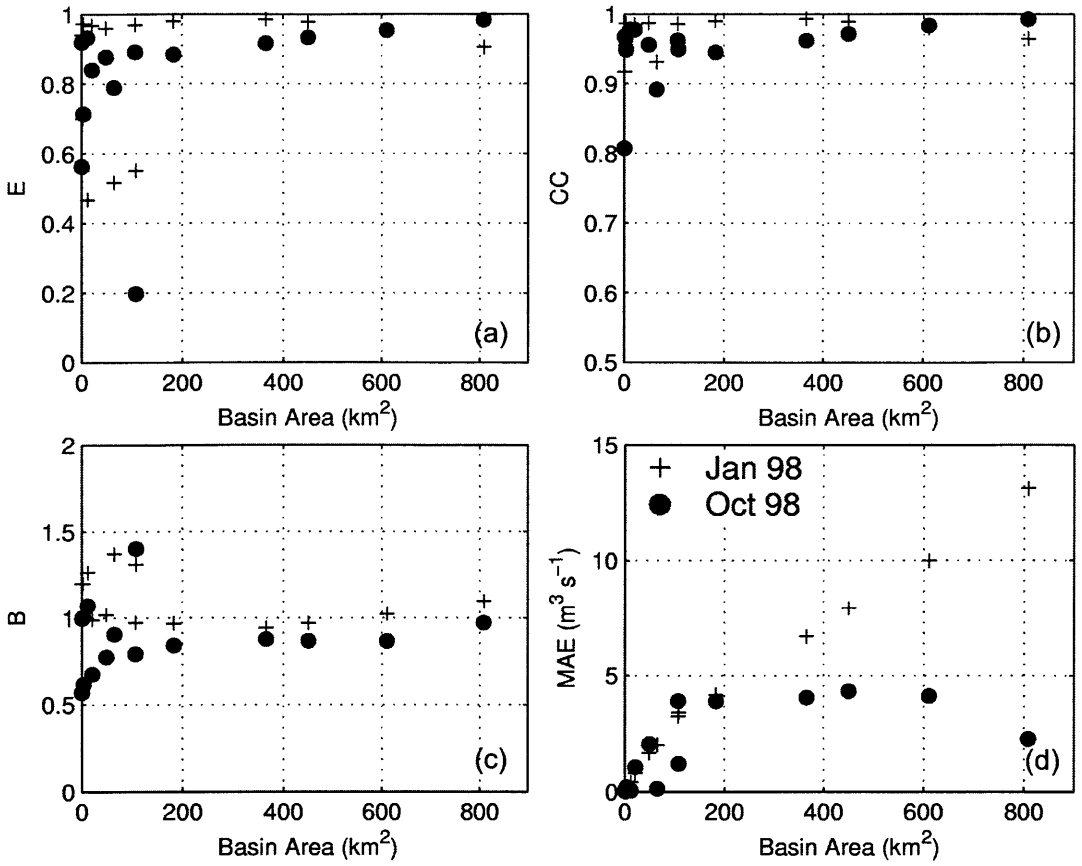

Figure 5.11. Flood forecast skill as a function of basin area for the 1-h sequential mode. (a) Efficiency, (b) Correlation coefficient, (c) Bias and (d) Mean absolute error.

5.5.2.3 Rainfall Variability Dependence

Flood event predictability depends on the nowcasting ability to accurately forecast rainfall in the appropriate place and time. In describing space-time forecast dependence, the combined STNM-tRIBS models have utilized the full radar content and the spatial sensitivity of the hydrologic model. Model skill can be further investigated by separating the effects of the spatial distribution from the temporal variation of the rainfall forecast. This is frequently done for assessing the impact of rainfall variability on hydrologic simulations (*e.g.*, Pessoa *et al.*, 1993, Bell and Moore, 2000).

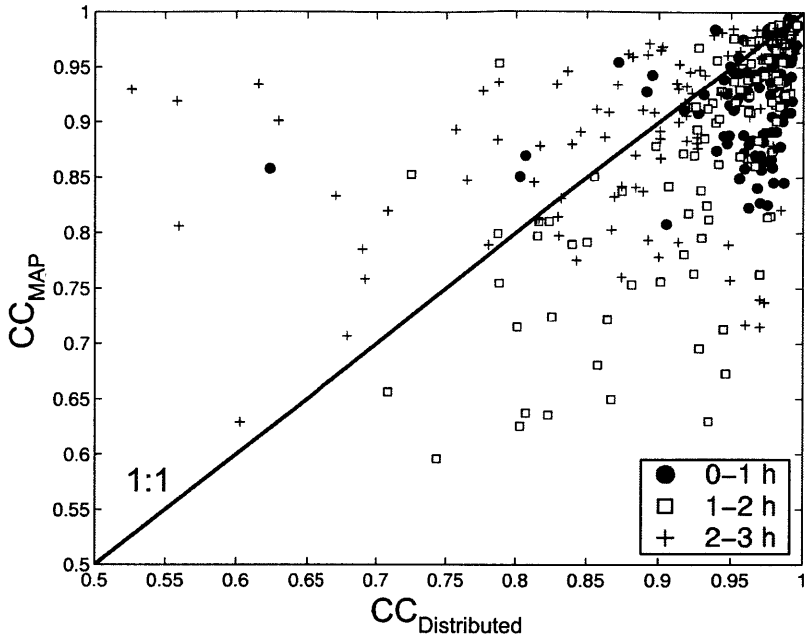

Figure 5.12. Impact of spatial rainfall variability on flood forecast skill for the sequential mode stratified by lead time.

To test the importance of rainfall variability, we compare the sequential mode using the distributed radar data with a mean areal precipitation (MAP) derived from the forecast rain field. The basin-averaged rain is identical in temporal variation to the STNM forecast. As a result, the forecast rainfall loses its spatial structure yet retains its dependence on lead time. Figure 5.12 compares the correlation coefficient (*CC*) of the distributed and average forecasts, illustrating that rainfall variability is important over a range of lead times. The results are stratified into three lead time categories: 0 to 1, 1 to 2, and 2 to 3 h. This classification shows that for low t_L (0 to 2-h), forecast skill is greater for the distributed rainfall (higher *CC*). For high t_L (> 2-h), the MAP forecast outperforms the distributed product. This suggests that retaining the rainfall spatial variability is most important for short t_L while an average product may be advantageous for large t_L.

5.5.3 Quantitative Comparisons of Flood Forecast Methods

Flood forecast skill for STNM-tRIBS modes is compared to a simple persistence forecast for the two storm events and in three nested basins (Figure 5.13). Persistence assumes a static rain field during the forecast interval while the STNM mimics storm dynamics. Although there is variability in the mode performance, we can elucidate some key features. The persisted rainfall provides the best flood forecast for very short lead-times ($t_L < 0.75$ h) across basin scales and events. Storm evolution over a particular sub-basin determines the time over which persistence is the favored method. When the rainfall pattern changes quickly, persistence underperforms relative to the STNM. Capturing storm dynamics through large-scale rainfall extrapolation in the batch and sequential modes is critical for lead times in the range of one to three hours. In a similar study, Dolciné *et al.* (2001) also found that nowcasting was superior to persistence in terms of rainfall and flood forecast skill.

Flood forecast skill varies between the sequential and batch modes with the particular storm dynamics. In addition to varying smoothly with t_L, the batch mode tends to perform better in events exhibiting growth, decay or rapid motion (October 1998). For storms that retain their structure as they pass over the catchment (January 1998), the sequential forecast is superior. These differences are related to the formulation of each mode. As an interpolation of radar observations, the sequential mode benefits from slow changes in storm structure. On the other hand, the batch forecast considers all available data so that growth and decay are explicitly retained through observations.

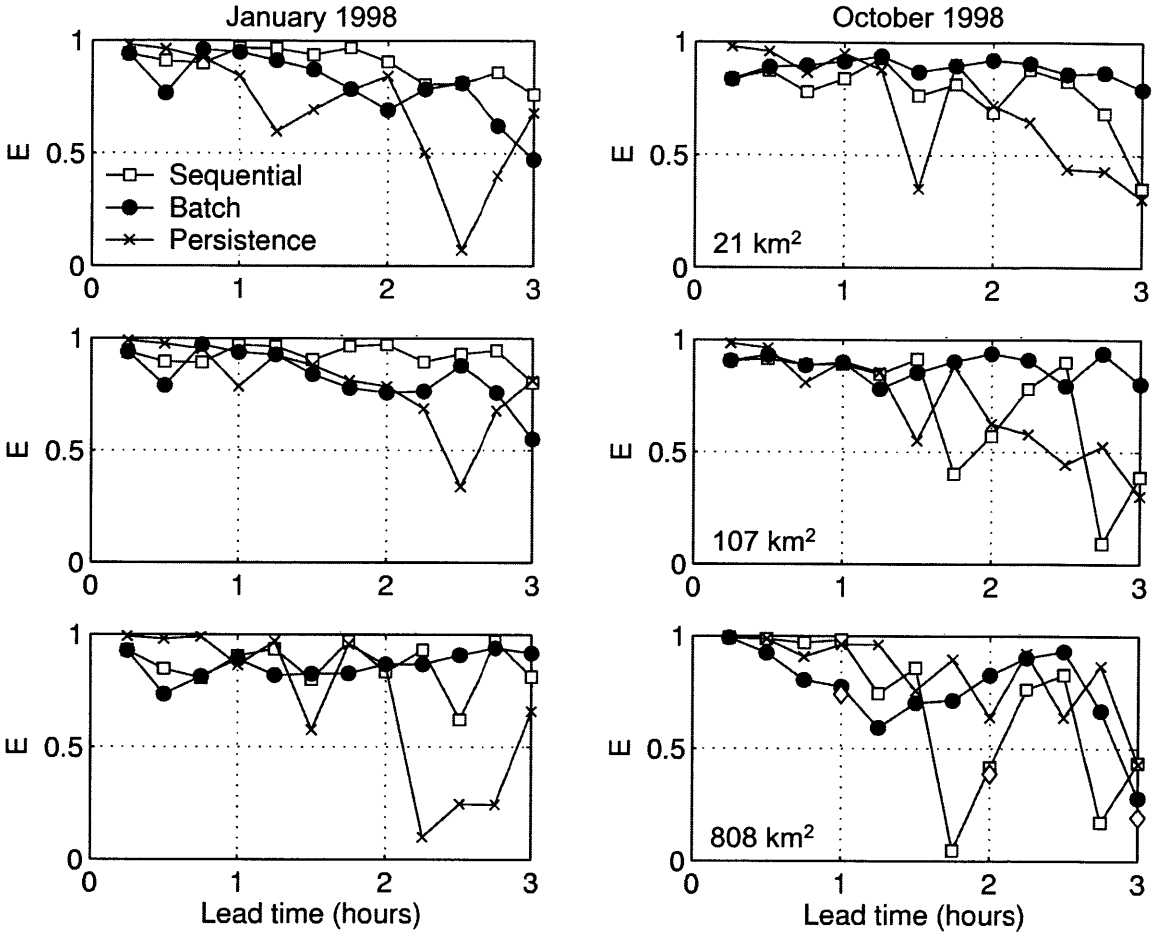

Figure 5.13. Flood forecast skill versus lead time for the Jan (left) and Oct (right) events at BF (bottom), DM (middle) and sub-basin 12 (top). The diamonds for Oct 1998 at BF are results using NEXRAD (4-km, 1-hour) in sequential mode.

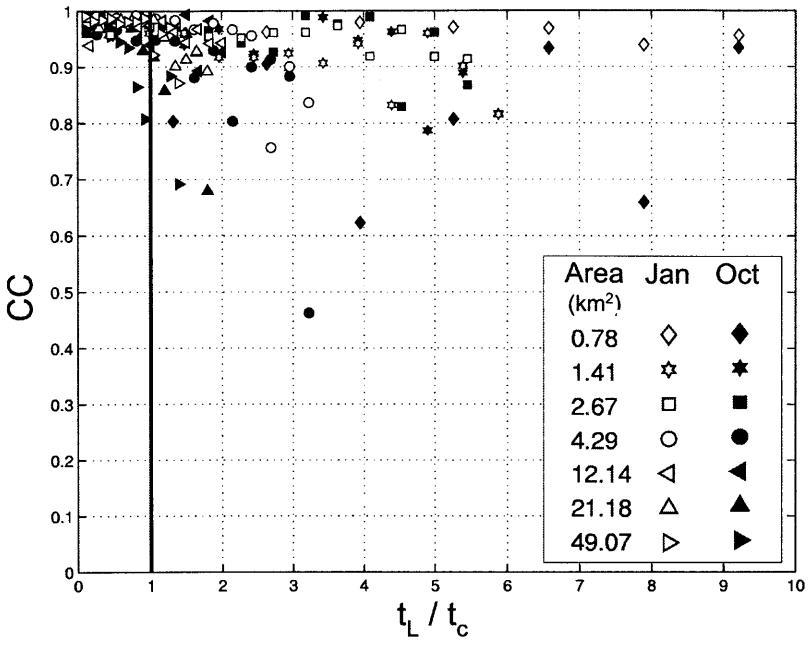

Figure 5.14. Space-time scale dependence of flood forecast skill for the smallest seven sub-basins during the two flood events. Flood forecast skill, as measured by correlation coefficient (*CC*) worsens for $t_L/t_C > 1$.

5.5.4 Rainfall-Flood Predictability and Scale

Identifying the space-time scales over which the combined forecasts have high skill is critical for determining flood predictability. Using the nowcasting model, flood forecast skill has been shown to decrease with lead time for one basin scale (Figure 5.10) and increase with basin area at a single lead time (Figure 5.11). A useful synthesis of both effects can be derived by scaling the forecast lead-time with the basin time of concentration (t_c). Table 5.3 presents t_c for each Baron Fork sub-basin, computed from the relief ratio (S) and length (L) in each channel network (Kirpich, 1940). An empirical estimate of the basin lag time, t_c provides a means for scaling t_L without knowledge of the storm-dependent response in each sub-basin. In this context, t_c captures differences in basin spatial scale.

Figure 5.14 shows the variation of flood forecast skill with the space-time scale (t_L/t_c) for the sequential mode. The results are limited to the smallest sub-basins (A=0.78 to 49.07 km^2) since these have response times (t_c = 0.19 to 2.16 h) within the maximum lead time (t_L = 3 h). Note that flood forecast skill decreases sharply for values of $t_L/t_c > 1$, suggesting that the limit of flood predictability is related to this scale. For rainfall forecast with t_L less than the basin response time, the flood forecast skill is high. As the forecast lead time increases relative to the basin spatial scale (t_c), forecast skill deteriorates. Nowcasting predictions work best within basins whose response time is on the order or less than the rainfall forecast lead time. Using t_L/t_c for different events and forecasting models may serve as an adequate indication of rainfall-flood predictability.

5.6. Discussion and Conclusions

The primary objective for utilizing rainfall forecasts in hydrology models is to increase flood warning time and accuracy. In this study, an algorithm based on the extrapolation of large-scale storm motion is used to derive short-term rainfall predictions. Forecasts are subsequently used in a distributed model to produce multiple-gauge flood hydrographs. Through comparisons to radar-driven simulations, flood predictability of the coupled models is assessed in a simulated real-time operation. Results indicate that flood prediction skill decreases with forecast lead-time and increases with basin area. The space-time model performance is shown to be a function of the ratio of the lead time to basin lag time. This analysis suggests that hydrometeorological forecast skill is high for the space-time scales corresponding to flash flood events in small, headwater basins.

The combined forecast system takes advantage of a high resolution radar network. For generating flood predictions utilizing all available radar data, two techniques were

developed to provide multi-step ahead (sequential) or single-step ahead (batch) forecasts. The sequential and batch modes improve flood forecast skill in relation to a persistence forecast, in particular over one to three hour lead times. In order to extend forecast skill, rainfall forecasts from atmospheric models and satellite rainfall nowcasting should be evaluated within the existing framework (*e.g.*, Grassotti *et al.*, 2002, Ganguly and Bras, 2002). In particular, predictions from meteorological models could provide skill over longer lead times. A promising development is the lead-time dependent fusion of rainfall forecasts from multiple sources.

Distributed hydrologic models provide new opportunities for flood forecasting in multiple, nested basins of varying scale. Flood prediction in interior catchments provides information on the differential runoff production within a basin and its propagation through the channel network as a function of rainfall spatial variability. In an operational setting, the spatial-temporal variation of flood discharge can improve existing flood warning techniques. In addition, distributed models provide quantitative predictions of internal hydrologic states and fluxes which may be useful in many applications. Understanding the space-time predictability of soil moisture, for example, is a promising area of research that can also be addressed with the combined use of a radar nowcasting and distributed hydrologic models.

References

ASCE Task Committee. 1999. *Geographic information system modules and distributed models of the watershed.* ASCE, Reston, VA. 120 pp.

Bell, V.A. and Moore, R.J. 2000. The sensitivity of catchment runoff models to rainfall data at different spatial scales. *Hydrology and Earth System Science.* 4, 653-667.

Benoit, R., Pellerin, P., Kouwen, N., Ritchie, H., Donaldson, N., Joe, P. and Soulis, E.D. 2000. Toward the use of coupled atmospheric and hydrologic models at regional scales. *Monthly Weather Review.* 128, 1681-1705.

Bradley, A.A. and Smith, J.A. 1994. The hydrometeorological environment of extreme rainstorms in the Southern Plains of the United States. *Journal of Applied Meteorology.* 33, 1418-1431.

Browning, K.A. and Collier, C.G. 1989. Nowcasting of precipitation systems. *Reviews of Geophysics.* 27, 345-370.

Carpenter, T.M., Georgakakos, K.P. and Sperfslagea, J.A. 2001. On the parametric and NEXRAD-radar sensitivities of a distributed hydrologic model suitable for operational use. *Journal of Hydrol*ogy. 253, 169-193.

Chornoboy, E.S., Matlin, A., Morgan, J. 1994. Automated storm tracking for terminal air traffic control. *Lincoln Laboratory Journal.* 7(2), 427-448.

Cluckie, I.D. and Owens, M.D. 1987. Real-time rainfall runoff models and use of weather radar information. In: *Weather radar and flood forecasting*, ed. Collinge, U.K. and Kirkby, C. Chichester, UK. 171-190.

Collier, C.G. 1991. The combined use of weather radar and mesoscale numerical model data for short-period rainfall forecasting. In *Hydrological Application of Weather Radar*, ed, Horwood, E. Chichester, UK. 331-348.

Dixon, M. and Weiner, G. 1993. TITAN: Thunderstorm identification, tracking, analysis and nowcasting – A radar-based methodology. *Journal of Atmospheric and Oceanic Technology.* 10, 785-797.

Dolciné, L., Andriue, H., Sempere-Torres, D. and Creutin, D. 2001. Flash flood forecasting with coupled precipitation model in mountainous Mediterranean basin. *Journal of Hydrologic Engineering.* 6, 1-10.

Droegemeier, K.K. and Coauthors. 2000. Hydrological aspects of weather prediction and flood warning: Report of the Ninth Prospectus Development Team of the U.S. Weather Research Program. *Bulletin of the American Meteorological Society.* 81, 2665-2680.

Ganguly, A.R. and Bras, R.L. 2002. Distributed quantitative precipitation forecasting using information from radar and numerical weather prediction models. Submitted to *Journal of Hydrometeorology.*

Garrote, L. and Bras, R.L. 1995. A distributed model for real-time flood forecasting using digital elevation models. *Journal of Hydrology.* 167, 279-306.

Georgakakos, K.P. 1986. A generalized stochastic hydrometeorological model for flood and flash-flood forecasting. 2. Case studies. *Water Resources Research.* 22, 2096-2106.

Grassotti, C., Hoffman, R.N., Vivoni, E.R., Entekhabi, D., Ivanov, V. and Van Horne, M.P. 2002. *Real-time hydrometeorological forecasting from radar and satellite observations.* ARO DAAD-19-00-C-0114 Final Report, 85 pp.

Grassotti, C., Hoffman, R.N., Vivoni, E.R. and Entekhabi, D. 2003. Multiple timescale intercomparison of two radar products and rain gauge observations over the Arkansas-Red River basin. Accepted to *Weather and Forecasting.*

Grecu, M. and Krajewski, W.F. 2000. A large-sample investigation of statistical procedures for radar-based short-term quantitative precipitation forecasting. *Journal of Hydrology.* 239, 69-84.

Hamill, T.M. and Nehrkorn, T. 1993. A short-term cloud forecast scheme using cross correlations. *Weather and Forecasting.* 8, 401-411.

Ivanov, V.Y., Vivoni, E.R., Bras, R.L. and Entekhabi, D. 2003. Development of a triangulated irregular network model for real-time, continuous hydrologic forecasting. Submitted to *Water Resources Research.*

Johnson, D., Smith, M., Koren, V. and Finnerty, B. 1997. Comparing mean areal precipitation estimates from NEXRAD and rain gauge networks. *Journal of Hydrologic Engineering*. 4, 117-124.

Kirpich, Z.P. 1940. Time of concentration of small agricultural watersheds. *Civil Engineering*. 10, 362.

Legates, D.R. and McCabe, G.J. 1999. Evaluating the use of "goodness-of-fit" measures in hydrologic and hydroclimatic model validation. *Water Resources Research.* 35, 233-241.

Mecklenburg, S., Bell, V.A., Moore, R.J. and Joss, J. 2000. Interfacing an enhanced radar echo tracking algorithm with a rainfall-runoff model for real-time flood forecasting. *Phys. Chem. Earth (B).* 25, 1329-1333.

Mimikou, M.A. and Baltas, E.A. 1996. Flood forecasting based on radar rainfall measurements. *Journal of Water Resources Planning and Management.* 122, 151-156.

Pereira Fo, A.J., Crawford, K.C. and Stensrud, D.J. 1999. Mesoscale precipitation fields. Part II: Hydrometeorologic modeling. *Journal of Applied Meteorology*. 38, 102-125.

Pessoa, M.L., Bras, R.L. and Williams, E.R. 1993. Use of weather radar for flood forecasting in the Sieve basin: A sensitivity analysis. *Journal of Applied Meteorology*. 32, 462-475.

Singh, V.P. and Woolhiser, D.A. 2002. Mathematical modeling of watershed hydrology. *Journal of Hydrologic Engineering*. 7, 270-292.

Smith, J.A., Seo, D.J., Baeck, M.L. and Hudlow, M.D. 1996. An intercomparison study of NEXRAD precipitation estimates. *Water Resources Research.* 32, 2035-2045.

Smith, K.T. and Austin, G.L. 2000. Nowcasting precipitation – a proposal for a way forward. *Journal of Hydrology.* 239, 34-45.

Tsanis, I.K., Gad, M.A. and Donaldson, N.T. 2002. A comparative analysis of rain-gauge and radar techniques for storm kinematics. *Advances in Water Resources*. 25, 305-316.

Van Horne, M.P., Vivoni, E.R., Entekhabi, D., Hoffman, R.N. and Grassotti, C. 2003. Quantitative precipitation forecasts from radar nowcasting for hydrologic applications over the Arkansas-Red River basin. Submitted *to Journal of Hydrometeorology.*

Vivoni, E.R., Ivanov, V.Y., Bras, R.L. and Entekhabi, D. 2002. Topography, triangulated irregular networks and hydrological similarity. Submitted to *Journal of Hydrologic Engineering.*

Vivoni, E.R., Van Horne, M.P., Ivanov, V.Y., Entekhabi, D., Bras, R.L., Grassotti, C. and Hoffman, R.N. 2003. Quantitative flood forecasts based on short-term radar nowcasting. Preprints, *17th Conference on Hydrology*, Long Beach, CA, AMS. J4.4.

Wolfson, M.M., Forman, B.E., Hallowell, R.G. and Moore, M.P. 1999. The growth and decay storm tracker. Preprints, *79th AMS Annual Conf.*, Dallas, TX, AMS. 4.3.

Yates, D.N., Warner, T.T. and Leavesley, G.H. 2000. Prediction of a flash flood in complex terrain. Part II: A comparison of flood discharge simulations using rainfall input from radar, a dynamic model and an automated algorithmic system. *Journal of Applied Meteorology*. 39, 815-825.

Young, C.B., Bradley, A.A., Krajewski, W.F., Kruger, A. and Morrissey, M.L. 2000. Evaluating NEXRAD multisensor precipitation estimates for operational hydrologic forecasting. *Journal of Hydrometeorology.* 1, 241-254.

Chapter 6:

Coupled Surface-Subsurface Response to Rainfall: Nonlinearity and Scale-dependence

6.1 Introduction

The response of natural catchments to rainfall depends on the mechanisms of runoff generation and their spatial and temporal organization over complex terrain. To investigate this issue, a number of distributed catchment models incorporating the land-surface and atmospheric heterogeneities controlling runoff have been developed. These quantitative tools have been used to investigate the impact of rainfall variability on floods (*e.g.*, Ogden and Julien, 1993, Winchell *et al.*, 1998), understand the role of topography in hydrologic response (*e.g.*, Western and Grayson, 2000, Berger and Entekhabi, 2001), and identify couplings between vadose zone and aquifer processes (*e.g.*, Paniconi and Wood, 1993, Levine and Salvucci, 1999).

To date, however, computational and hydrologic constraints in existing models have precluded investigations of the transient, surface-subsurface response to rainfall over complex terrain. For example, the interaction between surface and groundwater topography, the lateral redistribution of soil moisture, and the dynamics of surface saturation over heterogeneous basins have received limited attention. In this chapter, we address the transient catchment response to storm events using a coupled surface-subsurface model and examine the implications on the nonlinearity and scale-dependence of the rainfall-runoff transformation.

Following Sivapalan *et al.* (2002), the nonlinearity in catchment response refers to the observation that a unit increase in rainfall may not produce an equivalent increase in

measured runoff. While linear theory is the foundation of the unit hydrograph and similar approaches, it has been recognized from numerous studies that catchment runoff response can be highly nonlinear (*e.g.*, Betson, 1964, Dunne and Black, 1970, Caroni *et al.,* 1986, Troch *et al.*, 1993b, Risbey and Entekhabi, 1996). Recent work by Robinson *et al.* (1995) has shown that nonlinearity in basin runoff arises from both the hillslope response and network geomorphology, depending primarily on watershed size. At many scales, the runoff mechanisms operating in a catchment have been shown to affect the runoff response with consequences to flood frequency (Sivapalan *et al.*, 1990, Robinson and Sivapalan, 1997). Differences in the time scales of surface and subsurface flows are a critical source for the observed nonlinearity in basin response. Surface (infiltration- or saturation-excess) runoff is a quick response as infiltration is limited by soil properties or saturated conditions. Subsurface (return flow or groundwater) runoff is slower as infiltration and subsurface paths delay the response to rain. Transitions in runoff mechanisms over a heterogeneous basin are largely dictated by storm properties such as rain duration and intensity (Larsen *et al.*, 1994, Menabde and Sivapalan, 2001).

Rainfall characteristics elicit different responses by preferentially forcing quick and/or slow components of the surface-subsurface system. Saghafian and Julien (1995) showed, for example, that nonlinear response in pervious catchments can be attributed to conditions where rain duration is shorter than the basin time to equilibrium. Caroni *et al.* (1986) showed that runoff nonlinearity was also a function of rain intensity, with linear behavior observed for larger events. Superimposed on storm variability are spatial heterogeneities in topography, soils and vegetation which create conditions favorable to particular mechanisms (*e.g.*, Freeze, 1974, Sivapalan *et al.,* 1987). For example, regions

of flow convergence near streams interact strongly with the groundwater table to produce saturation-excess runoff. As aquifer recharge increases, saturated regions expand and lead to greater runoff production for a unit rainfall amount. Thus, the nonlinearity in response attributed to variable source areas depend on the basin wetness and storm characteristics.

In addition to influencing the nonlinear runoff response, surface and groundwater interactions impart a signature on the scale dependency of runoff. Following Sivapalan *et al.* (2002), scale-dependence refers to the effect of catchment area on runoff properties. Numerous studies have shown that discharge may exhibit stronger or weaker dependence on scale as area increases, depending on the hydrologic processes in the basin (*e.g.*, Wang *et al.*, 1981, Goodrich *et al.*, 1997). Both antecedent wetness and storm characteristics, through forcing particular mechanisms, create differences in runoff scale-dependence over multiple subbasins. In small catchments, the short response times relative to storm duration lead to contributions from surface and subsurface runoff. As catchment scale increases, storm duration is shorter than the response time from each mechanism, thus leading to partial contributions. Thus, in natural basins, stream discharge results from the interrelationship between processes with multiple time constants and catchment size.

In this chapter, we address the nonlinearity and scale dependence of catchment runoff in a topographically complex, humid watershed. A distributed hydrologic model, the *TIN-based Real-time Integrated Basin Simulator* (tRIBS) (Ivanov *et al.*, 2003a), is applied with spatially-uniform forcing to investigate the coupled surface and groundwater response at multiple gauges. The numerical model is used as an interpretive tool for addressing observed storm event differences in basin response. The relation between runoff production and catchment response time and magnitude is investigated to elucidate

the causes for nonlinearity with respect to rainfall amount. Antecedent wetness conditions imposed through a distributed water table position are varied to explore its effect on runoff generation. Finally, scale relationships of the catchment response characteristics are analyzed in the context of the coupled unsaturated-saturated flow model.

6.2. Hydrologic Data and Catchment Simulations

Runoff sensitivity to surface-groundwater interactions is explored through use of the tRIBS model in a humid watershed. The basin is well-suited for investigating the relationship between runoff mechanisms and flood response due to a spatially-variable water table that reacts quickly to rainfall. Frequent flood occurrences are typically due to Fall and Spring storms (Bradley and Smith, 1994; Michaud *et al.*, 2001). The active aquifer provides rain-fed discharge and baseflow throughout the year (Imes and Emmett, 1994). In the following, we describe the basin and its hydrologic data, prior efforts leading to model calibration and the numerical simulations conducted in this chapter.

6.2.1 Study catchments

tRIBS is applied to the Baron Fork at Eldon, OK (BF: 808 km^2) that includes two gauged subbasins, Peacheater Creek at Christie, OK (PC: 65 km^2) and Baron Fork at Dutch Mills, AR (DM: 107 km^2). Figure 6.1a presents the basins, gauging stations, and stream network overlaid on a TIN derived from a USGS 30-m DEM (Vivoni *et al.*, 2002). Parts of the basin are rugged and heavily dissected while others are flat or gently sloping. The basin is composed of a mixed land use of forest (52.2%), croplands (46.3%), and towns (1.3%) (Figure 6.1b). Surface soil texture is primarily silt loam (94%) and fine sandy loam (6%). Alluvial deposits are common along the floodplain, while shale,

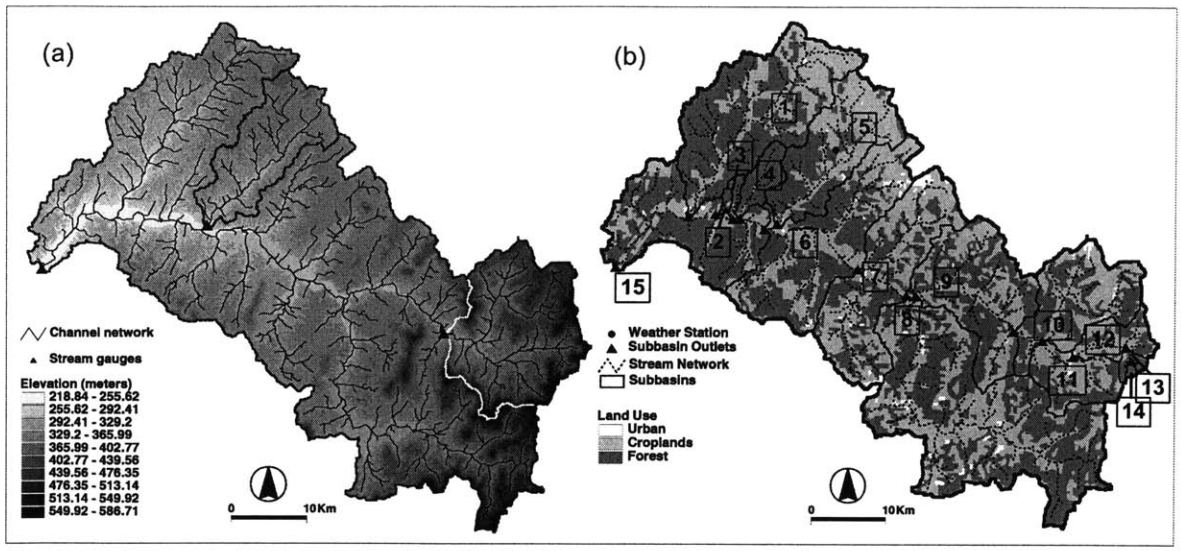

Figure 6.1. Model description of surface topography and land-use. (a) TIN representation including modeled stream network, and gauging stations for BF (outer basin), PC (black inner basin), and DM (white inner basin). (b) Spatial distribution of land use and land cover (urban, forest, grassland) with the sub-basin locations and outlets (numbered 1-15) and the weather station.

limestone, and chert are present in ridges and hillslopes. The Springfield Plateau aquifer underlying the basin feeds groundwater to the streams through various springs (Imes and Emmett, 1994). The channel network has tributaries ranging from first to fifth order, a maximum length of 67.3 km and a mean drainage density of 0.86 km^{-1}. The channel geometry is estimated from the relations presented by Carpenter *et al.* (2001).

In addition to the gauged basins, a series of ungauged interior watersheds were delineated from the DEM to represent a range of catchment scales and properties (Figure 6.1b). Table 6.1 presents a limited set of geomorphic parameters (*e.g.*, channel slope, S; stream length, L; mean elevation, μ; and elevation standard deviation, σ) that characterize the nested basins, including three orders of magnitude range in area, A = 0.8 to 800 km^2. Numerous studies have focused on the hydrology of the Baron Fork and its sub-catchments due to its unregulated nature, high rain and stream gauge density and a long

Basin	A (km^2)	μ (m)	σ (m)	L (km)	S ($m\ km^{-1}$)	D_d (km^{-1})
1	108.23	316.72	29.22	25.73	6.06	0.99
2	1.41	282.36	17.90	2.59	34.01	0.83
3	2.67	290.04	23.52	4.52	21.44	0.77
4	12.14	302.00	24.45	8.06	14.94	0.81
5#	65.06	327.63	28.08	19.90	9.26	0.83
6	610.60	360.08	58.66	50.33	6.81	0.84
7	450.26	374.52	59.41	40.01	8.11	0.84
8	365.25	385.55	59.64	35.03	9.09	0.82
9	182.91	386.59	57.18	29.78	9.49	0.82
10*	106.91	408.07	57.44	18.64	13.41	0.84
11	49.07	413.34	63.30	12.72	19.10	0.87
12	21.18	427.63	59.04	9.03	24.92	0.87
13	4.29	468.17	48.50	3.53	51.27	0.77
14	0.78	479.81	42.91	1.33	112.77	0.30
15+	808.39	346.54	59.02	67.26	5.47	0.86

Table 6.1. Characteristic of the Baron Fork and subbasins. A is the basin area; μ is the DEM mean elevation, σ is the DEM standard deviation; L is the maximum subbasin distance; S is the relief ratio; D_d is the drainage density. Symbols indicate gauges: (#) Peacheater Creek, (*) Baron Fork at Dutch Mills, and (+) Baron Fork at Eldon.

time series of high-quality radar rainfall data (*e.g.*, Johnson *et al.*, 1997). In addition, a model intercomparison project has been recently performed in Baron Fork to compare lumped and distributed approaches to flood forecasting (Smith *et al.*, 2003).

6.2.2 Rainfall and hydrologic observations

Hydrologic measurements in the catchment consist of three USGS stream gauges, various rain gauges, multiple NEXRAD radars and one weather station (Figure 6.1b). Gauge-corrected radar is a reliable source of hourly (4-km by 4-km) precipitation data in the basin. The mean annual rain of 1240 mm is primarily distributed in two wet periods (March-June and September-November). Over the years 1993 to 2000, the mean areal precipitation in the Baron Fork varied from light rain (less than 1 mm/hr for one hour) to intense storm events (greater than 20 mm/hr over 6 hours). The variability in rainfall

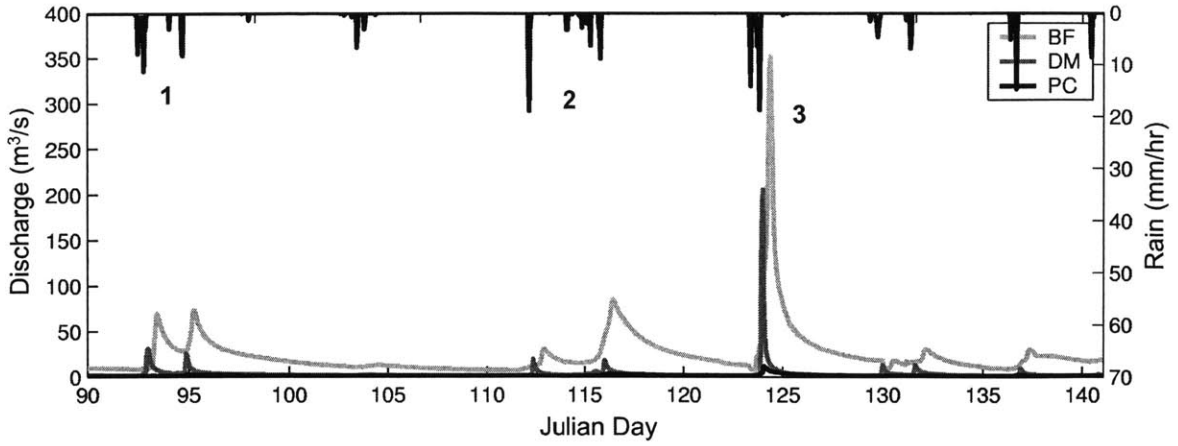

Figure 6.2. Nonlinearity and scale effects in basin response from NEXRAD-based mean areal rainfall (mm/hr) and USGS observed discharge (m^3/s) at the BF (light gray), DM (dark gray) and PC (black) catchments over the Spring period, 04/01/1999 to 05/22/1999. For the series of events 1, the runoff response is proportional to rainfall forcing. The large rainfall in series 2 produces low discharge (due to long interstorm period), while a similar magnitude storm event in series 3 produces the maximum yearly flood for the basins.

duration, intensity and spatial pattern, in addition to antecedent conditions in the heterogeneous catchment, lead to a variable runoff response during storm and interstorm events. Discharge data from the nested streamflow gauges illustrate how the observed variability in rainfall is transformed in a nonlinear manner into runoff (Figure 6.2).

Large flood events in the basin have a tendency to occur in October and May in response to large-scale storm events (*e.g.*, Bradley and Smith, 1994). As an example, Figure 6.2 illustrates the maximum flood in 1999 occurring in May 4-5 (event 3) preceded by a series of storms. The storm, composed of two rain bands embedded with intense convective cells, caused discharge reaching 351, 206 and 12 m^3/s in the BF, DM and PC basins. Although flood levels were not reached (563.5, 283.4 m^3/s at BF, DM), the event was significant in terms of flood frequency. It is observed that flood magnitude in this case depends on antecedent wetness conditions in the basin. The series of events leading up to the flood induced high moisture content and pronounced baseflow in the

basin that ultimately led to a vigorous response to rainfall. A prior storm of similar magnitude (event 2) elicited a weaker runoff response as the antecedent wetness was low due to a long interstorm period. For the series of events in early April (event 1), the basin response is proportional to rainfall forcing. Surface-subsurface interactions are expected to partially explain the observed nonlinearity in floods with respect to rainfall.

6.2.3 Numerical simulations of catchment response

Catchment response variability due to the interaction of surface and groundwater is explored in this study through a set of numerical simulations. The multi-year model calibration over the Baron Fork is used to specify the surface, subsurface and channel properties. Given the verified model, the sensitivity of the basin response is explored as a function of the initial water table position and rainfall properties. For these experiments, a spatially-uniform storm is assumed since our objective is to identify nonlinearity and scale effects in flood response and their relationship to underlying runoff mechanisms. In addition, a single storm event is simulated without considering a continuous simulation, as in Ivanov *et al.* (2003a,b). Interstorm variability is captured by specifying different initial states corresponding to observed baseflow. Both assumptions can be readily relaxed through the use of observed or simulated rainfall patterns.

In these simulations, we address the impact of uniform storm rainfall duration (t_r) and intensity (i) on the production of runoff from variable locations within a complex catchment. Storm durations and intensities chosen for the simulations are representative of the conditions leading to flash flooding in small basins in the Southern Great Plains (Michaud *et al.*, 2001). We focus on flood events in the Fall period (September to November) rather than Spring to minimize effects from snowmelt that may induce

surface wetness conditions not related to the water table position. In addition, the impact of evapotranspiration on runoff production and water table fluctuations is reduced during the Fall due to tree leaf-out and low atmospheric demand. Accordingly, the Fall period moisture conditions in the basin are a strong function of the interannual fluctuations in Summer rain. We capture this interannual variability through the different initial water table states. Spatial patterns in antecedent wetness are due to redistribution of moisture in the hillslope system. In this manner, the representative rainfall forcing in the Fall is applied to the expected baseflow conditions given possible amounts of Summer rainfall.

6.3. Results

Simulations of the basin response to uniform rain are discussed with respect to the antecedent wetness and storm properties. The model predictions of peak discharge (q_p) and time to peak (t_p) are then related to the runoff mechanisms and catchment scale.

6.3.1 Antecedent moisture conditions

A key to surface-groundwater coupling over complex terrain is the hydrologic partitioning at the land-surface that occurs as a function of water table depth (Salvucci and Entekhabi, 1995). The water table position relative to the surface determines (1) the location of perennial and permanently saturated areas near channels or riparian zones, (2) the partitioning of rainfall into distinct surface runoff mechanisms, and (3) the moisture and evapotranspiration within the top soil layer. Accordingly, determining the basin response to rainfall using a coupled surface-subsurface model requires appropriate treatment of the water table position. Here, we study the effect of groundwater depth on catchment response by selecting three antecedent wetness conditions.

To initialize the model, both the saturated zone thickness and soil moisture profile must be specified. The initial moisture profile $\theta(z)$ is determined entirely by the soil hydraulic properties and the depth to water table (N_{wt}). Ivanov *et al.* (2003a) describe a method for constructing an initial groundwater distribution based on Sivapalan *et al.* (1987). As an alternative, we determine a model-based initial water table position through a drainage experiment. By allowing a fully-saturated catchment to drain for an extensive period of time (10 years), the transient readjustment of the subsurface head field occurs within the geomorphic context of the modeled basin. In the absence of rain and evapotranspiration, discharge produced in the catchment is due exclusively to exfiltration from the saturated zone. VanderKwaak and Loague (2001) used a similar strategy to initialize a surface-subsurface model prior to a storm event simulation.

Figure 6.3 presents the groundwater system response from the long-term drainage in Baron Fork. The rating curve obtained for the shallow aquifer relates subsurface discharge to the water table level. In this model, baseflow (Q_b) produced in the basin is routed through the hillslope and channel networks to the outlet. The spatial distribution of the water table position (N_{wt}) and its moments (mean (μ) and standard deviation (σ)) are also measured. From the observed discharge at Baron Fork (1993-2000), we selected three different initial states: *wet* (Q_b = 5 m^3/s), *medium* (Q_b = 2 m^3/s) and *dry* (Q_b = 0.5 m^3/s). These levels represent distinct baseflow observed prior to storm events with exceedence probabilities of 0.48 (wet), 0.75 (medium), and 0.99 (dry). In Figure 6.3, the states correspond to μ [N_{wt}] = –4.57 m (wet), –5.49 m (medium), –6.79 m (dry) which occur 330, 840 and 3360 days into the basin drainage, respectively. Of note is that both the mean and spatial pattern (σ [N_{wt}]) of the water table vary during the drainage period.

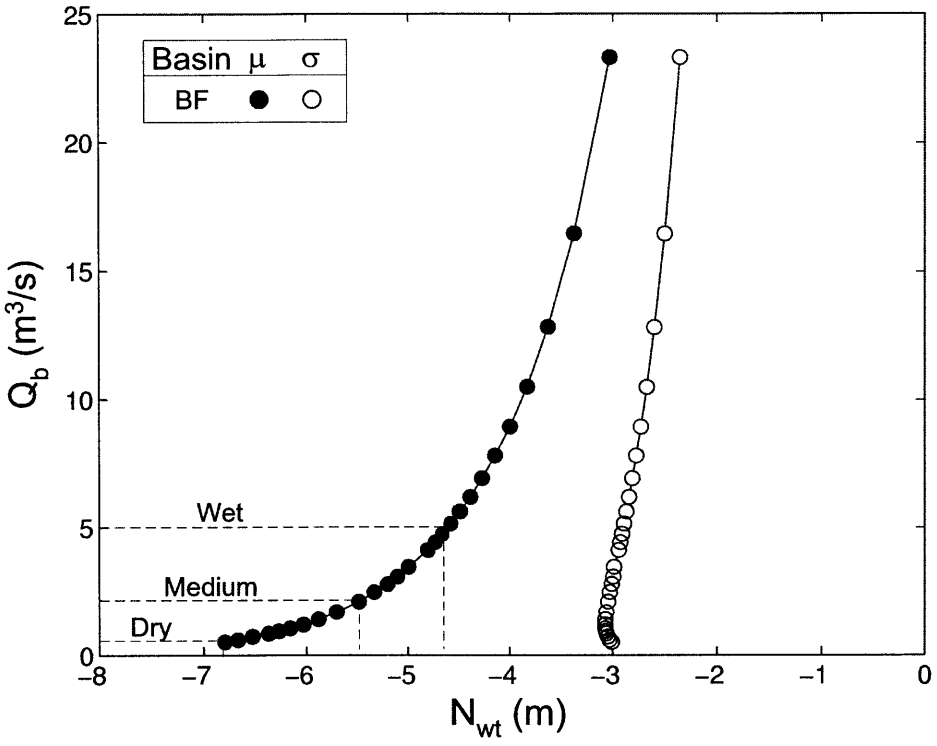

Figure 6.3. Groundwater recession curves for the Baron Fork. Mean (μ) and standard deviation (-σ) of depth to groundwater table (N_{wt}) versus baseflow discharge (Q_b).

More importantly, the groundwater rating curve provides insight into the saturated zone dynamics that control catchment response to rainfall. Eltahir and Yeh (1999) and Marani *et al.* (2001), for example, describe the physical basis for the nonlinearity in observed relations between baseflow and water table position. Nonlinear rating curves result from the strong interaction between the groundwater level and the surface topography. As an aquifer drains, the initial decrease in baseflow is strong as the saturated land-surface area is rapidly depleted of moisture. As the recession progresses, the intersection between the aquifer and land-surface is confined to the channel network and the baseflow declines at a slower rate. In light of this, the catchment response to rainfall should be a strong function of antecedent wetness and its location within the nonlinear groundwater rating curve (*e.g.*, wet versus dry).

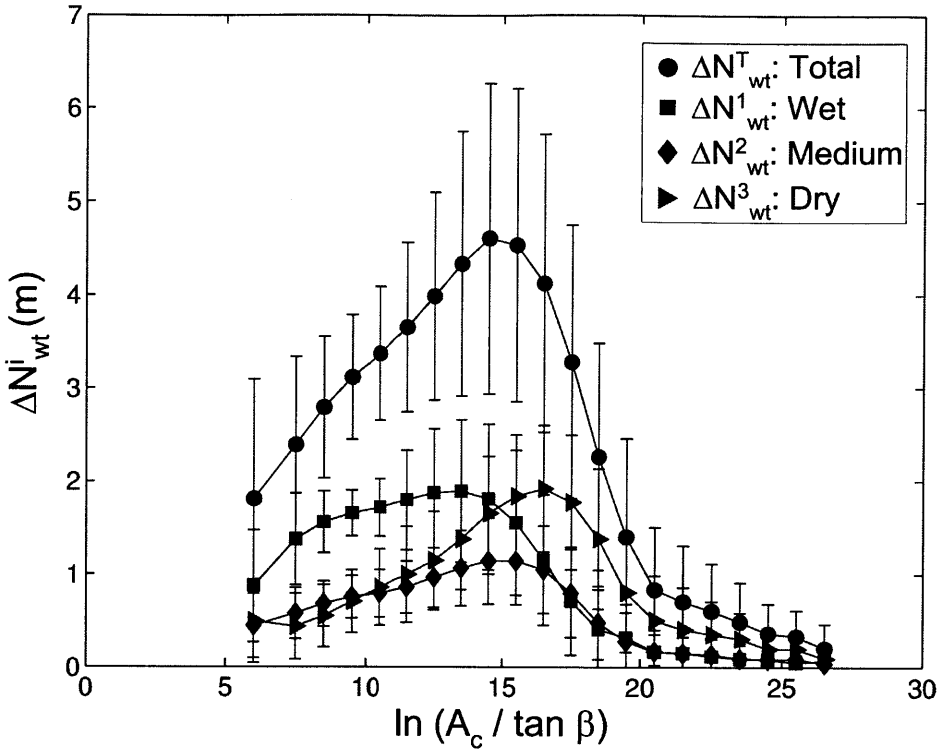

Figure 6.4. Time evolution of topographic control on groundwater recession. Bin mean values (symbols) and standard deviation (bars) of the change in water table position (ΔN^i_{wt}) over four time periods versus the topographic index, λ = ln (A_c / tan β). ΔN^T_{wt}: total water table decrease between saturated state and Q_b (dry); ΔN^1_{wt}: decrease between saturation and Q_b (wet); ΔN^2_{wt}: decrease between Q_b (wet) and Q_b (medium), ΔN^3_{wt}: decrease between Q_b (medium) and Q_b (dry).

The distribution of the groundwater state giving rise to the nonlinear system response is further explored in Figure 6.4 as the time-evolution of the water table decrease (ΔN^i_{wt}). Given the coupling between aquifer level and topography in producing baseflow, determining the locations contributing to exfiltration is of primary interest. In Figure 6.4, basin elements are classified according to an index of hydrologic similarity:

$$\lambda = \ln\left(\frac{A_c}{\tan\beta}\right), \tag{6.1}$$

where A_c is the drainage area and β is the local slope angle, that captures differences in saturation due to landscape location (*e.g.*, Beven and Kirkby, 1979, O'Loughlin, 1986).

The space-time evolution of the basin drainage is represented by the water table drop (ΔN^{i}_{wt}) between the initial time and end of the drainage (ΔN^{T}_{wt}) as well as the difference between wetness states, ΔN^{1}_{wt} (initial–wet), ΔN^{2}_{wt} (wet–medium), ΔN^{3}_{wt} (medium–dry).

The spatial dynamics in Figure 6.4 indicate that groundwater exfiltration over the drainage period (ΔN^{T}_{wt}) is strongly related to topographic position. The largest decreases in saturated thickness occur for elements with λ = 12 to 18, suggesting that these regions supply the highest moisture to baseflow. Nevertheless, ΔN^{T}_{wt} is composed of separate periods with differing contributions from the basin. From the initial to the wet state (ΔN^{1}_{wt}), baseflow is dominated by steep upland regions (low λ). With much of the soil columns saturated throughout the basin, the highest flows occur under the steepest gradients. As time progresses, upland areas are depleted of moisture and the groundwater change (ΔN^{2}_{wt}) decreases. Subsequently, the flat lowland regions begin to dominate baseflow as evidenced by the pronounced peak at higher λ (ΔN^{3}_{wt}). Furthermore, the soil columns in the basin are less moist leading to lower total baseflow. These surface-groundwater dynamics are consistent with the observations by Zecharias and Brutsaert (1988) and indicate the potential variability in catchment response as the antecedent conditions are varied from wet to dry.

6.3.2 Storm hydrograph response

The storm event response in the Baron Fork is explored through variations of the initial groundwater table position and rainfall properties. The initial states vary slightly in their saturated surface area (A_s) prior to the storm. The saturated basin fraction (A_s/A) is 0.06 (wet), 0.03 (medium) and 0.01 (dry) for the three states. In terms of groundwater

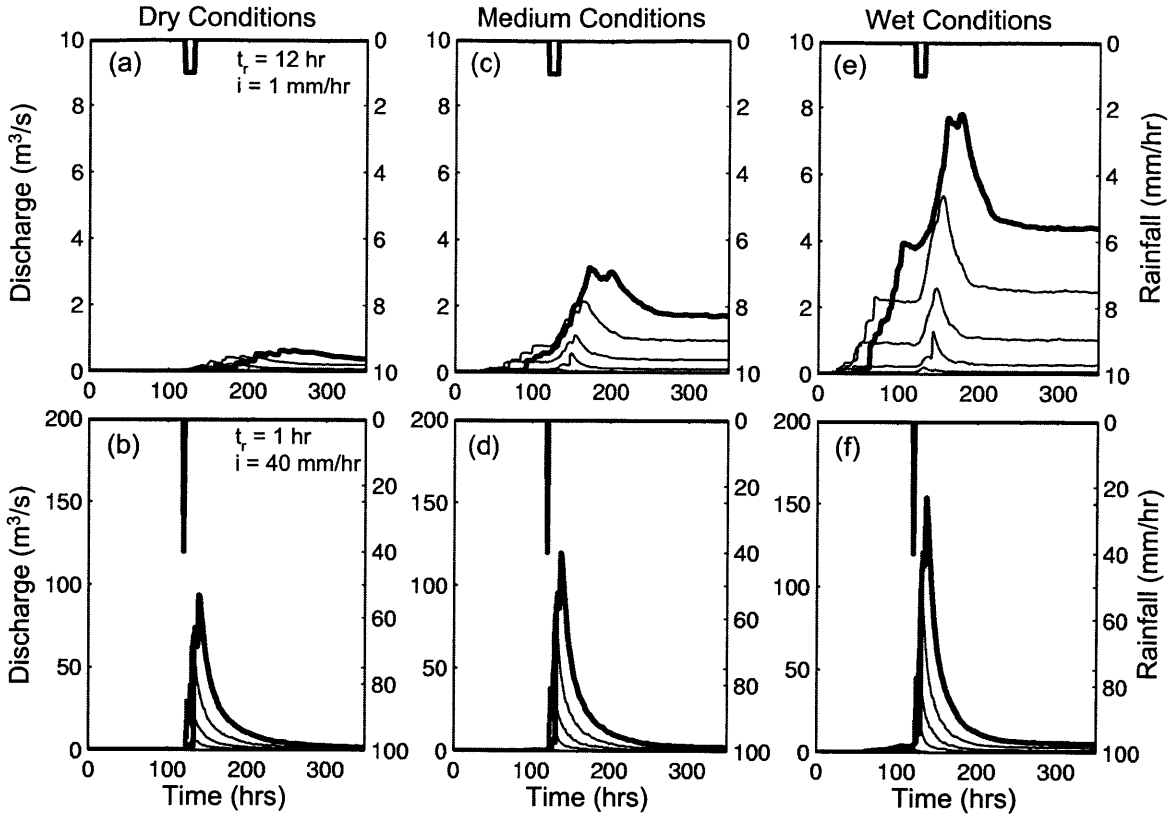

Figure 6.5. Hyetographs and multi-gauge response to storm event under varying rainfall and wetness conditions (wet, medium, and dry). The top row (a, c, e) represent a combination of low rain rate (i = 1 mm/hr) and long duration (t_r = 12 hr). The bottom row (b, c, d) illustrates results for a high rain rate (i = 40 mm/hr) and short duration (t_r = 1 hr). The thick solid line correspond to the outlet discharge (808 km^2), while the thin lines represent catchment areas of 450.26, 182.91, 65.06, 12.14 and 0.78 km^2, respectively.

position, however, the initial states vary significantly with the mean depth to water table equal to 4.57 m (wet), 5.49 m (medium) and 6.79 m (dry). These antecedent conditions influence the runoff response to the uniform rain event arriving 120 hours into the simulation period (15 day total). Storm properties are varied over a range of intensities (1–40 mm/hr) for three durations (1, 6, 12 hr) to obtain thirty (i, t_r) storm pairs. The rainfall and atmospheric forcing are typical for a Fall period in the Baron Fork.

Figure 6.5 presents the storm hydrograph at multiple basins in the Baron Fork. Two combinations of rain duration and intensity have been selected from the range of

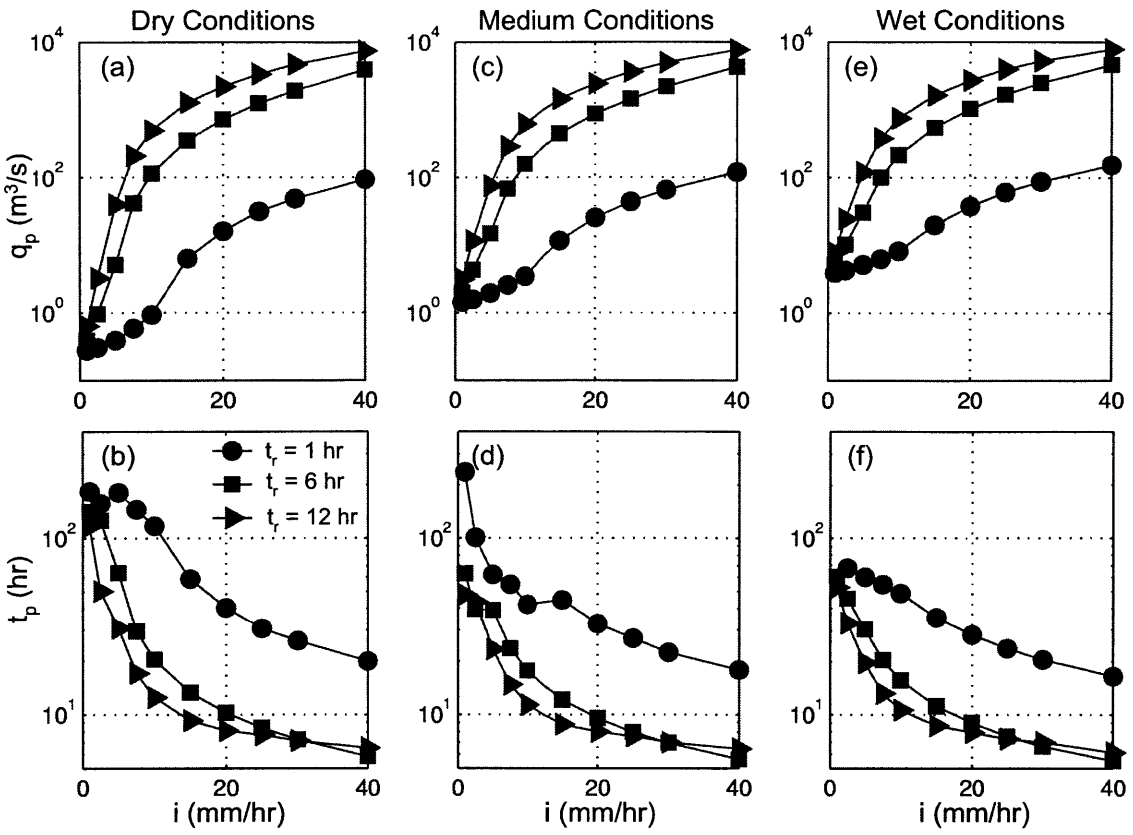

Figure 6.6. Hydrograph sensitivity to storm characteristics and antecedent conditions. Peak discharge (q_p) and time to peak (t_p) for single events of duration (t_r) and intensity (i) at the outlet of Baron Fork.

values. The first storm type (i = 1 mm/hr, t_r = 12 hr) corresponds to a long-duration, low-intensity drizzle, while the second storm (i = 40 mm/hr, t_r = 1 hr) is more reflective of a short-duration, high-intensity thunderstorm. Storm differences impact the hydrograph as the rainfall interacts in variable ways with the surface-subsurface system, for example in terms of peak magnitude and timing. In addition, the antecedent wetness has an important effect on the amount of discharge for a given rainfall quantity. Under dry conditions, basin storage capacity is sufficiently high to reduce the runoff potential. When the water table is closer to the surface, an increase in saturation promotes a quick and intense runoff

response. Figure 6.5 also show the runoff response variation with basin area. In particular, the peak discharge and time to peak increase as the catchment area increases.

The combined effect of storm properties and antecedent wetness can lead to a rich set of runoff responses at various basin scales. Figure 6.6 further explores the impact of i and t_r on the peak discharge (q_p) and time to peak (t_p), defined as the difference between the rain center of mass and the peak. Figure 6.6 reveals the nonlinearity in the peak and timing as a function of i and t_r. In relation to rain intensity, two regimes can be identified, corresponding to low and high i. The transition near i ~ 15-20 mm/hr is potentially due to values of K_{on}, the saturated hydraulic conductivity, specified as 0.5 (urban), 2.8 (crops) and 35 (forests) mm/hr (Table 2.2). K_{no} controls the amount of infiltration and determines the degree of quick surface response. The basin-averaged K_{on} for Baron Fork equals 19.7 mm/hr, within the regime transitions for t_p and q_p. For interior basins, this transition may occur at values close to the average K_{on} which vary with subbasin land-use (Figure 6.1b).

As observed for the two storm types in Figure 6.5, antecedent wetness conditions affect the hydrograph peak and timing. However, this effect is not identical across the rainfall intensity range. Note that the variation of q_p and t_p with wetness in Figure 6.6 is more pronounced for low rainfall intensities (drizzle). At high intensities (thunderstorm), the degree of basin saturation plays a smaller role in determining catchment response. For example, q_p is identical for i = 40 mm/hr and t_r = 1 to 12 hr across the range of water table positions. This is consistent with Figure 6.5 showing an 8-fold increase in q_p with wetness for the low intensity regime, while only a 50% increase is observed for the high intensity storm. Thus, the transition marked by the basin infiltration capacity (K_{on}) exerts a strong control on the catchment response to storms of varying duration and intensity.

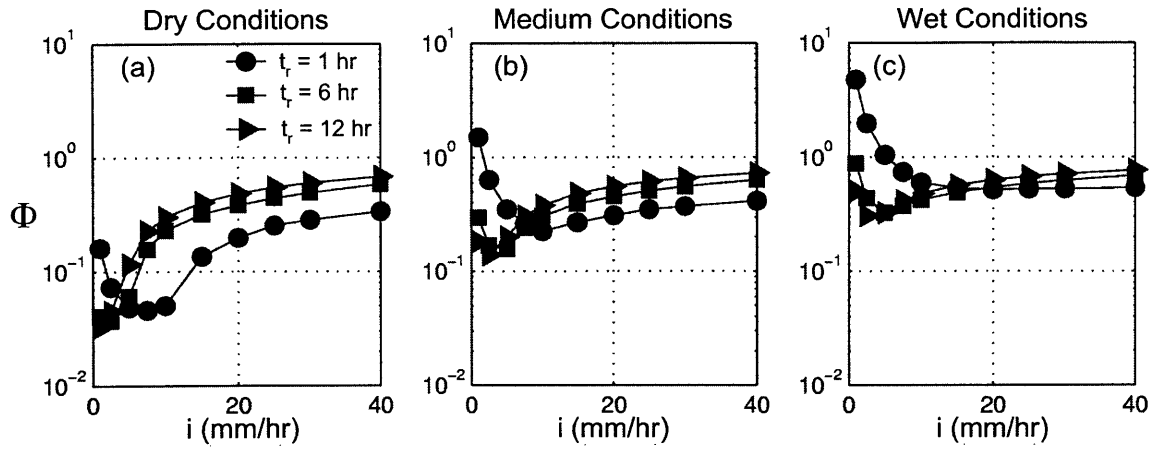

Figure 6.7. Nonlinearity in the catchment response illustrated by the runoff coefficient ($\Phi = R / P$) as function of rainfall intensity for the three antecedent conditions (wet, medium, dry) and storm durations (1, 6, and 12 hours).

The effect of surface-groundwater interactions on storm runoff response is further explored in Figure 6.7. Here, the nonlinearity in the catchment response is explicitly shown through the use of the catchment runoff ratio (Φ), defined as:

$$\Phi = \frac{R}{P}, \tag{6.2}$$

where R and P are the basin storm runoff and rainfall volumes. For a linear system, the partitioning coefficient is independent of rain amount (*e.g.*, Risbey and Entekhabi, 1996), *i.e.* Φ is constant. Depending on basin properties, a linear rainfall-runoff relation leads to constant values of Φ ranging from 1 (impervious) to 0 (fully pervious). It is apparent from Figure 6.7, that Baron Fork exhibits a wide variability of Φ that depend strongly on rain properties and antecedent wetness. It is interesting to note the three types of runoff nonlinearity: (1) asymptotically increasing $\Phi(i)$ (dry, t_r = 12 hr); (2) asymptotically decreasing $\Phi(i)$ (wet, t_r = 1 hr); and (3) a $\Phi(i)$ functionality exhibiting a minimum value. For each type, a transition is observed between the low and high intensity regimes.

In addition to storm properties, the nonlinearity in catchment response is linked to basin wetness. High nonlinearities are observed for dry conditions where the basin storage capacity limits runoff production. Increasing i leads to greater runoff from the basin and an asymptotic rise indicative of a linear response (Figure 6.7a). As wetness increases, Φ increases and differences between storm t_r and i are less apparent. For saturated conditions, the asymptotically decreasing $\Phi(i)$ indicate a baseflow effect at low intensities and a linear response for high intensities (Figure 6.7c). A wet basin responds linearly to rain as saturated areas act as impervious surfaces. The minima observed in the $\Phi(i)$ relation at various wetness levels corresponds to a transition from subsurface to surface regimes, as discussed in relation to the surface infiltration rate. A closer look at the various runoff mechanisms can reveal their control on basin nonlinearity.

6.3.3 Runoff generation and hydrologic regimes

Multiple runoff mechanisms arise from the interaction between infiltration fronts, the water table position and lateral moisture transport in conjunction with the surface moisture state and storm properties. The superposition of different mechanisms leads to the total storm hydrograph. For example, Figure 6.8 shows the separation of two storms into individual runoff mechanisms. In Figure 6.8a, the runoff response from a drizzle (i = 1 mm/hr, t_r = 12 hr, dry) is dominated by saturation-excess runoff during the storm and by groundwater throughout the period. Infiltration-excess runoff was not produced. In contrast, Figure 6.8b shows the thunderstorm runoff hydrographs (i = 40 mm/hr, t_r = 1 hr, dry). In this case, the storm response is composed of infiltration-excess with minor contributions from saturation-excess runoff. These examples show the process controls on basin response, including surface-subsurface influence on the storm peak and timing.

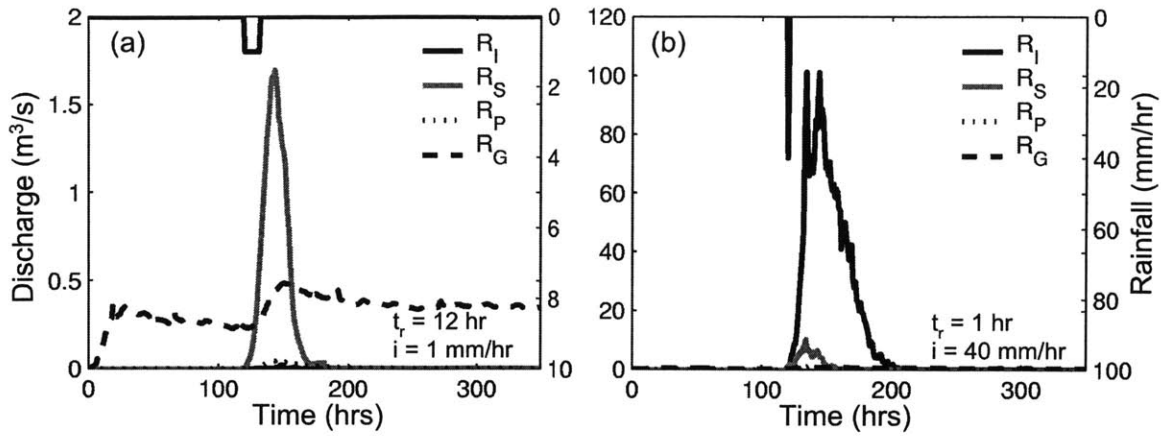

Figure 6.8. Hydrographs for runoff generation mechanisms: infiltration-excess (R_I), saturation-excess (R_S), perched return flow (R_P), groundwater (R_G) at Baron Fork outlet. (a) t_r = 12 hr, i = 1 mm, dry conditions. (b) t_r = 1 hr, i = 40 mm, dry conditions.

To explore the control of the surface and subsurface processes on basin runoff nonlinearity, Figure 6.9 presents a comparison of the runoff coefficient and the individual hydrograph component ratios. In Figure 6.9, Φ is normalized as:

$$\Phi^* = \frac{\Phi}{\Phi_{\max}}, \tag{6.3}$$

where $\Phi_{\max}$ is the maximum value of $\Phi(i)$, while the component ratios:

$$F_I = \frac{R_I}{R}, \quad F_S = \frac{R_S}{R}, \quad F_P = \frac{R_P}{R}, \quad F_G = \frac{R_G}{R}, \tag{6.4}$$

are shown as shaded areas corresponding to the fraction of runoff volume (R). Note that the surface component is $R_I + R_S$ while the subsurface component is $R_P + R_G$. Clearly, a strong relationship exists between the runoff nonlinearity and the surface-subsurface partitioning. Note the correspondence between the cases previously identified: increasing $\Phi^*(i)$, decreasing $\Phi^*(i)$, and $\Phi^*(i)$ with a minimum value, and the runoff fractions. For instance, Φ^* is observed to decrease with i when baseflow is the primary component. In contrast, rainfall and moisture conditions leading to infiltration-excess runoff exhibit a

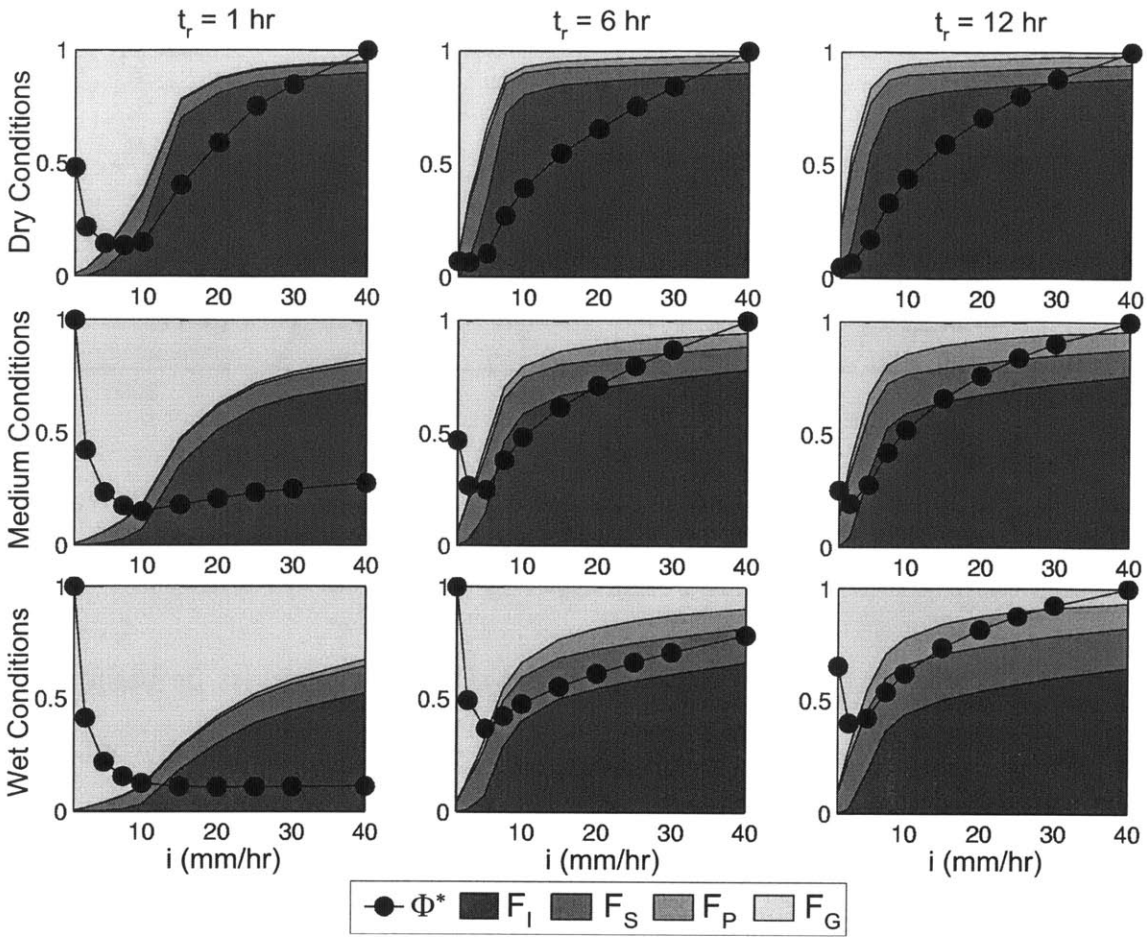

Figure 6.9. Relationship between nonlinear response and runoff mechanisms as function of t_r and i illustrated through the fraction of runoff ($F_i = R_i/R$) and the normalized runoff ratio (Φ^*) for different wetness conditions.

strong increase in $\Phi^*(i)$. The transition between subsurface ($\Phi^*(i)$ decreasing) and surface ($\Phi^*(i)$ increasing) regimes is gradual, showing a minima in $\Phi^*(i)$.

As shown in Figure 6.9, the interactions between surface and subsurface processes control the degree and functional form of the runoff nonlinearity. This corroborates studies that have shown the importance of process controls on the lumped basin response (*e.g.*, Sivapalan *et al.*, 1990, Robinson and Sivapalan, 1997). Much less is known about the runoff generation distribution within a basin. To explore the spatial runoff dynamics, Figure 6.10 presents the time-averaged runoff rate from each

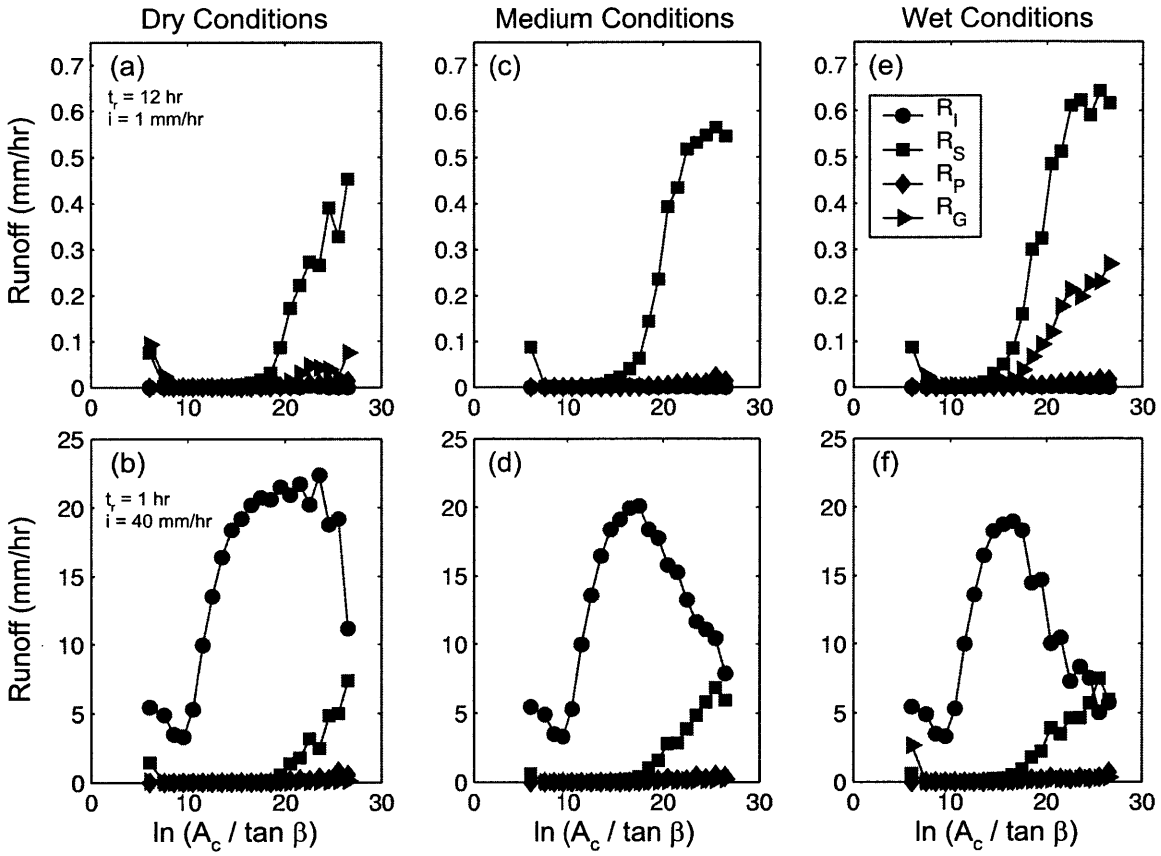

Figure 6.10. Spatial organization of runoff generation mechanisms as a function of water table position (wet, medium, dry) for two combinations of rain intensity and duration: t_r = 12 hr, i = 1 mm/hr (a, c, e) and t_r = 1 hr, i = 40 mm/hr (b, d, f). Average runoff production (mm/hr) is bin-averaged over distribution of ln (A_c / tan β). Note the different vertical scales in runoff rate for the different storm events.

component as a function of catchment location, captured by the topographic index (λ). The storm average runoff rate is very sensitive to the hydrograph peaks. As a function of λ, the runoff rate distributions highlight the locations that produce runoff peaks via a particular mechanism.

Figure 6.10 captures the distributions of R_I, R_S, R_P and R_G runoff from the drizzle and thunderstorm. Low-i, high-t_r storms are dominated by saturation-excess peaks. Locations producing this runoff type have high λ values, corresponding to flat areas with high drainage. When the water table position is closer to the surface, saturated regions

contributing to R_S expand towards lower λ values. In addition, a contribution at high λ is observed from subsurface flow (R_G) in the wet state. For high-i, low-t_r storms, R_I is the primary mechanism concentrated along intermediate λ (10 to 20). The distribution peak of R_I shifts to lower λ and decreases as wetness is increased. This suggests that interactions between topography and groundwater impact the generation of infiltration and saturation excess runoff in specific locations. For both events, upland areas (low λ) have low runoff rates, except for a small R_S and R_G observed in isolated, steep hillslopes.

Runoff mechanisms can vary in their spatial distribution as a function of rain properties and wetness state, as shown in Figures 6.9 and 6.10. Runoff types may occur simultaneous or preferentially within different topographic locations. As the water table position varies and interacts with basin topography, the hydrologic regimes can shift from surface to subsurface dominance. Thus, terrain complexity exerts a strong control over runoff processes. As topographic distributions change with scale, basin size and location should impact the mechanisms controlling storm response. In the following, we relate the process control on runoff nonlinearity to the scale dependencies observed in runoff.

6.3.4 Catchment scale and runoff generation

The variation of runoff with basin area encapsulates the complex interactions between storm properties and the internal hydrologic processes within each subbasin. Goodrich *et al.* (1997), for example, showed that a transition in runoff scale-dependence was due to channel losses and partial storm coverage in multiple basins. For the Baron Fork, the variation of terrain, land-use and soil properties, in addition to initial wetness, among the basins should also lead to scale-dependencies in the storm response. Based on the relation between runoff nonlinearity and the surface-subsurface mechanisms, we

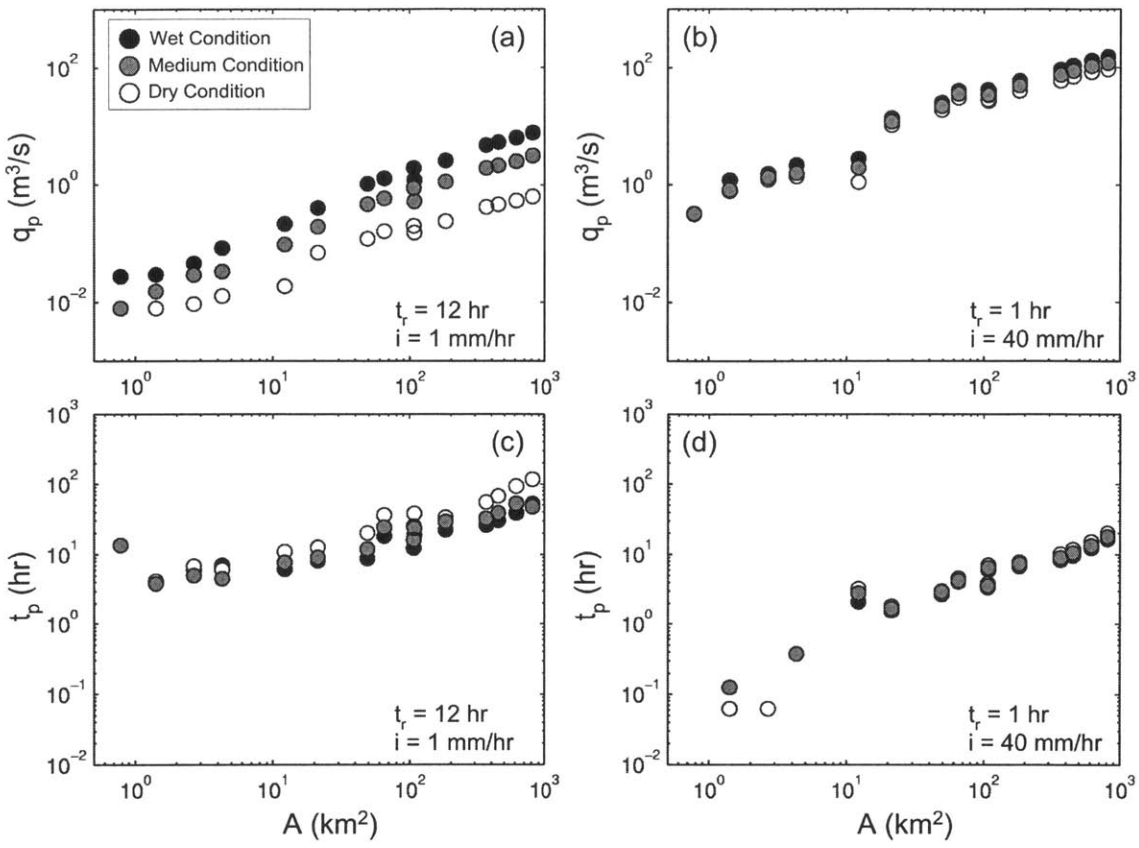

Figure 6.11. Scale-dependence of hydrograph peak (q_p) and time to peak (t_p) for the three antecedent wetness conditions. Two combinations of rainfall intensity and duration are shown: t_r = 12 hr, i = 1 mm/hr (a, c) and t_r = 1 hr, i = 40 mm/hr (b, d).

hypothesize that scale variations are tied to differences in subbasin runoff production.

Runoff properties, such as peak discharge of a specific return period and mean annual volume, have been shown to obey scaling laws with basin area (*e.g.*, Menabde *et al.*, 2001, Sivapalan *et al.*, 2002). The storm hydrographs shown for the multiple basins in Figure 6.5 suggest a possible scaling relation for q_p and t_p:

$$q_p = c_1 A^a, \tag{6.5}$$

$$t_p = c_2 A^b, \tag{6.6}$$

where c_1, c_2, a and b are parameters. Studies in various basins have found (6.5) to be a good predictor of q_p with $0.5 < a < 1$. In addition, Robinson and Sivapalan (1997) derived

a response time scaling similar to (6.6) with $b = 0.5$. Although typically applied to runoff statistics, these relations can be useful in assessing the scale-dependency of runoff.

Figure 6.11 shows the variation of the flood magnitude and timing with basin area for the Baron Fork catchments (0.78 to 808.39 km^2) for the two storm types (*e.g.*, drizzle, thunderstorm) and the three initial states. Note that a power law relation of the type expressed in (6.5) and (6.6) is apparent in both q_p and t_p over a range of basin areas (A) for these two storm types. The exponents (a, b) vary with wetness and storm properties in the ranges of $0.74 < a < 0.88$ and $0.34 < b < 0.86$. In general, an increase in wetness leads to an increase in a and decrease in b. In addition, the initial wetness impacts the coefficients (c_1, c_2) of the drizzle more than the thunderstorm. This is potentially due to variations in runoff production, as the peak for the low-i, high-t_r storm is composed of saturation-excess runoff while the high-i, low-t_r event is primarily infiltration-excess. As storm type is varied (i, t_r), the range of values for the power law relations (a, b, c_1, c_2) are expected to deviate from the results in Figure 6.11. Nevertheless, the variation of q_p and t_p with A is evidence for the existence of a scaling relation of the storm hydrograph.

To explore the impact of storm properties and initial wetness on runoff scale-dependence, Figure 6.12 (top) shows a comparison of q_p and t_p for the thirty (i, t_r,) storms in three basins (A = 0.78, 65.06, 808.39 km^2). The slope of the t_p-q_p relation is observed to vary with basin size as well as storm conditions. For large basins, the t_p-q_p relation is nearly constant over the entire q_p range. This is evident by the close to linear relation between log (t_p) and log (q_p) for the large (808 km^2) basin in Figure 6.12. However, as catchment area is decreased, t_p varies considerably with q_p. For small storms (low q_p), there is a wide variation in t_p. For larger storms (high q_p), t_p appears to reach a minimum

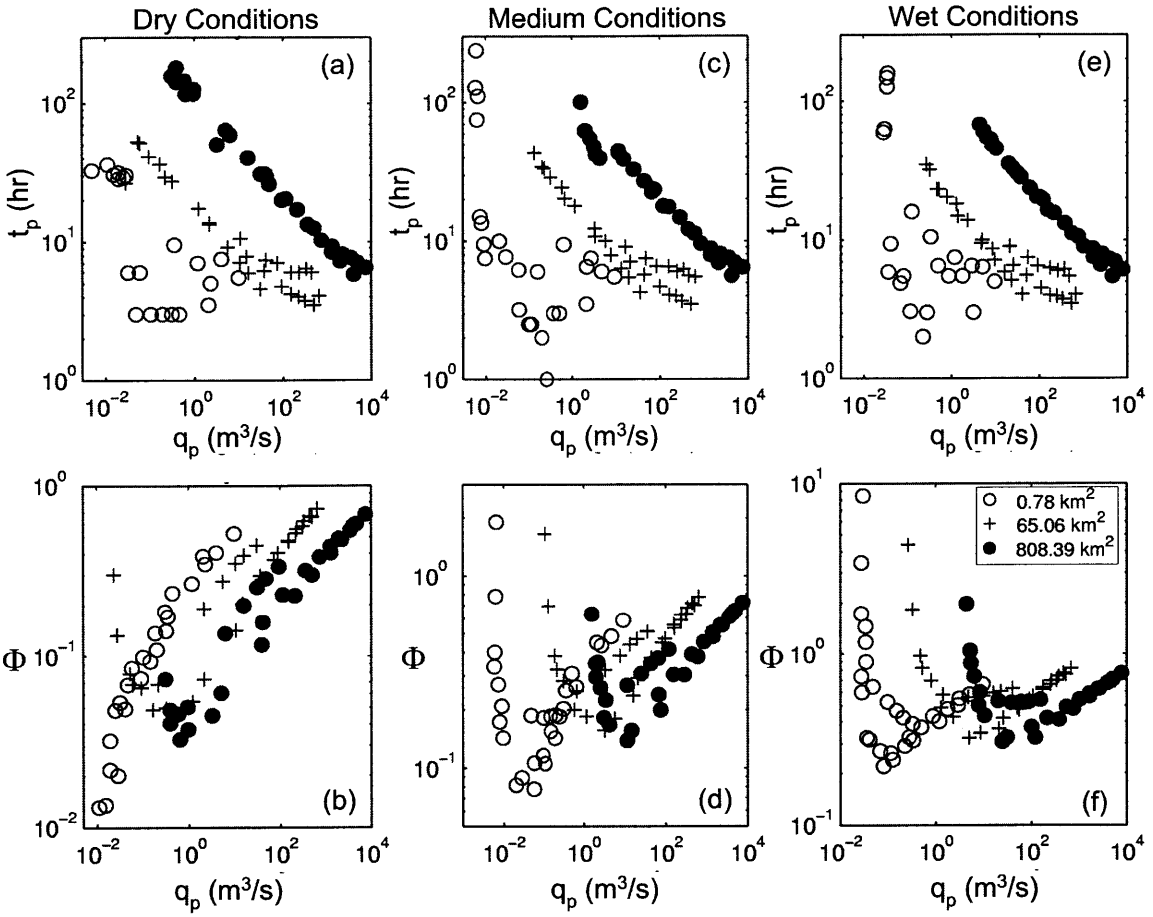

Figure 6.12. Relationships between hydrograph characteristics for different basin scales: A = 0.78 km^2 (open circles), 65.06 km^2 (crosses), 808.39 km^2 (closed circles). Time to peak discharge (t_p) versus peak discharge (q_p) for all t_r and i combinations as a function of wetness condition (a, c, e). Runoff ratio (Φ) versus peak discharge (q_p) (b, d, f).

value. Clearly, the response time of each basin is embedded in the t_p-q_p relation. For small basins, large storms permit contributions from each runoff component to reach steady-state since the basin residence time is low. As A increases, the higher residence time only allows partial contributions from each process even for large storms. Increasing q_p beyond the tested range should lead to a decline of t_p towards a basin-specific time constant for each catchment.

From the t_p-q_p relation, we observe that basin scale plays an important role in determining basin response. As a result, catchment size should be critical in the observed runoff nonlinearity within each subbasin. Figure 6.12 (bottom) presents the runoff ratio (Φ) as a function of q_p to illustrate the scale effect on runoff response. Note the existence of two regimes, Φ decreasing or increasing with q_p, for each basin wetness except for the small, dry catchment. A decreasing value of Φ for low q_p indicates that runoff decreases with respect to rainfall, as less contribution is expected from groundwater. An increasing value of Φ for high q_p reveals that runoff is increasing for a given discharge, as the basin wetness leads to a vigorous storm response. The minima in the Φ-q_p relation occurs at different values of peak discharge and runoff ratio for each basin area. The observed minima should be related to the runoff processes within each specific basin: subsurface response dominates for low q_p and surface response for high q_p. For the small, dry basin, the Φ-q_p relation suggests that subsurface runoff does not occur under these conditions.

Comparisons of the small and large basins suggest that scale does have an effect on the nonlinearity in basin response. As each basin is characterized by distinct land-surface properties, the partitioning of rain into surface and subsurface runoff can vary with basin size. To reveal this connection, Figure 6.13 shows the correspondence between the Φ-q_p relation and the runoff mechanisms within the three basins. Note that the Φ-q_p relation is reproduced directly from Figure 6.12 for the dry and wet condition. In order to capture the scale variation of runoff production, the spatial distributions of the storm-averaged runoff rate have been basin-averaged within each subcatchment. The result is a space-time average runoff rate for each mechanism, denoted by the shaded regions and symbols Ψ_I, Ψ_S, Ψ_P, Ψ_G in Figure 6.13. For example, in the small basin, the

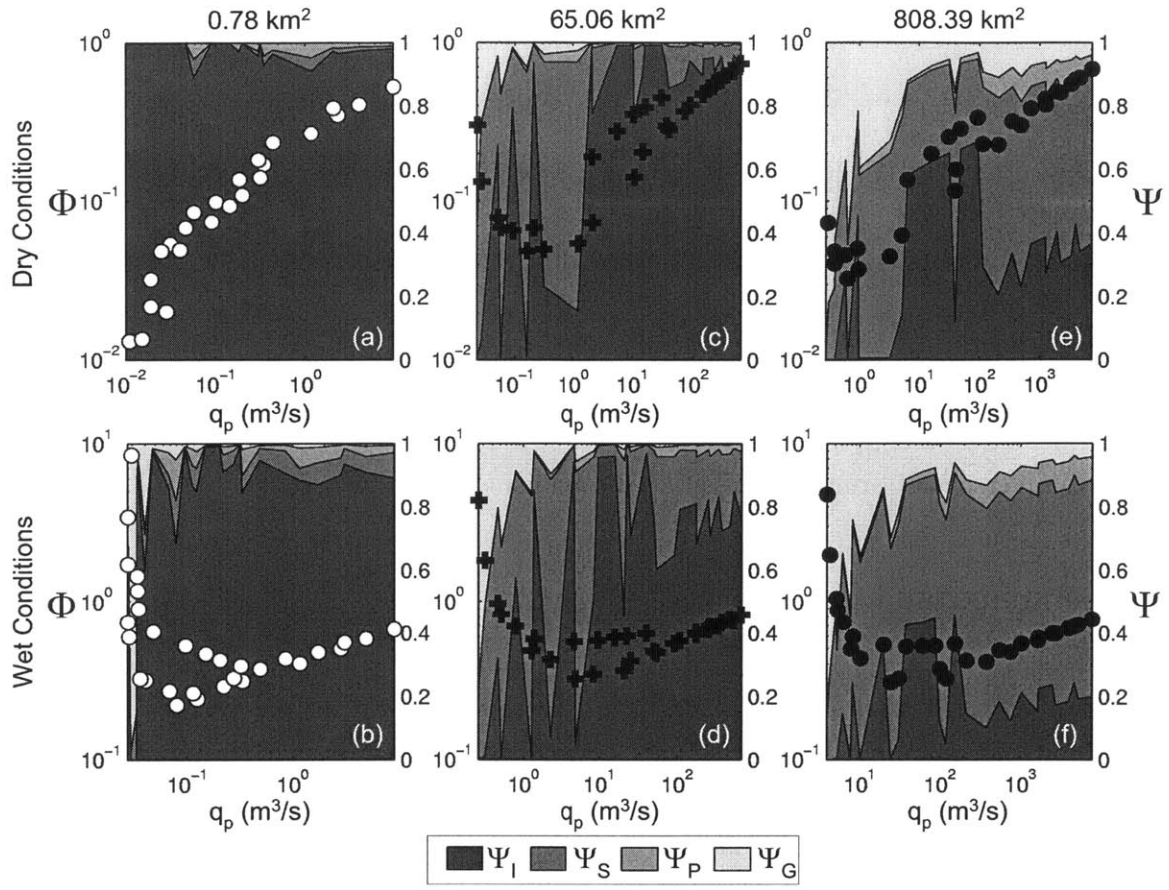

Figure 6.13. Scale-dependence of the catchment response nonlinearity and its relation to runoff production mechanisms. Three catchment scale, $A = 0.78$ km^2 (a, *b*), 65.06 km^2 (c, d), and 808.39 km^2 (d, e), are illustrated for the dry and wet antecedent states. Both the runoff ratio (Φ, symbols) and the space-time average runoff rate from each component (Ψ_I, Ψ_S, Ψ_P, Ψ_G, shading) are shown as a function of peak discharge (q_p).

infiltration-excess runoff rate (R_I) has been time-averaged over the storm period, spatially-averaged over the basin and expressed a fraction of the total runoff to form Ψ_I.

In Figure 6.13, the space-time average fractions (Ψ_I, Ψ_S, Ψ_P, Ψ_G) are shown for the thirty (i, t_r) storms as a function of q_p. The relation between the runoff ratio (Φ) and the runoff mechanisms in each basin explicitly reveals the process control on runoff nonlinearity and scale-dependence. The dominant component for the region of decreasing Φ is groundwater exfiltration (Ψ_G). For the region of increasing Φ, infiltration-excess

(Ψ_I) and saturation-excess (Ψ_S) runoff are the principle modes of runoff production. The minima observed in the Φ-q_p relation corresponds to the transition between subsurface ($\Psi_G + \Psi_P$) and surface ($\Psi_I + \Psi_S$) flows. The surface-subsurface transition is impacted by wetness conditions and basin scale. In particular, note that the small, dry basin has no contribution from subsurface flow due to a deep water table (Φ increasing with q_p). As basin area increases, more catchment locations interact with a shallow water table and lead to a diverse set of runoff production mechanisms.

6.4. Summary and Conclusions

The coupled surface-subsurface model utilized in this study has afforded the opportunity to examine the causal links between storm hydrograph variability and the underlying physical mechanisms leading to runoff production. In particular, the observed nonlinearity in the rainfall-runoff transformation has been tied directly to the partitioning of a storm event of particular intensity and duration into surface and subsurface flow. An analysis of runoff production over a series of subbasins further illustrated the scale-dependency of the underlying surface-subsurface mechanisms. In the coupled system, the interaction of the aquifer level with surface topography is a primary determinant of the storm runoff variability in terms of hydrograph magnitude, timing and volume.

The distributed hydrologic model permitted investigating the transient storm response over complex topography. It incorporated the interaction between surface and groundwater, the lateral redistribution of soil moisture, and the expansion and contraction of a variable source area. As a result, a full set of runoff mechanisms (infiltration-excess, saturation-excess, perched return flow and groundwater exfiltration) are produced from the unsaturated-saturated dynamics. The effect of the initial water table position on the

storm runoff response was analyzed by varying the groundwater head field as a function of observed baseflow. The distributed depth to water table provides a measure of the available basin storage capacity prior to a storm event (Troch *et al.*, 1993a).

Several important conclusions arise from the application of the distributed model to a series of storm events in the humid, complex basin. Given the rainfall and baseflow conditions, the flash flood events are representative for a typical Fall period when the interaction between surface and subsurface processes is pronounced.

(1) A strong relation was found between runoff nonlinearity and the partitioning of total storm flow into the four runoff mechanisms. The runoff component ratios were shown to correspond to the transition between different nonlinearity regimes across a wide range of storm properties and wetness conditions.

(2) The position of the water table relative to the surface topography dictates the temporal and spatial distribution of runoff generation in the catchment. Wetter conditions lead to more pronounced runoff demonstrating linearity with respect to rain. Nonlinear runoff response is greatest under dry catchment conditions.

(3) Catchment runoff mechanisms and groundwater dynamics preferentially occur in locations associated with a particular value of the topographic index. Storm properties and the water table influence the spatial dynamics of runoff production. In particular, saturated regions producing surface flow and groundwater expand with basin wetness.

(4) Storm hydrograph magnitude and timing were found to follow power law relations over a wide range of catchment areas for two selected storm types. Differences in basin initial wetness and rainfall properties lead to variability in power law parameters, in particular for events resulting in a groundwater response.

(5) Runoff nonlinearity was found to be basin scale-dependent and determined by the hydrologic processes operating within each catchment due to internal variability in topography, soils, vegetation and aquifer level. With increasing scale, a greater diversity in runoff mechanisms was observed due to increased basin complexity.

While the distributed hydrologic model has been an effective tool for exploring the nonlinearity and scale-dependence in catchment response, the conclusions obtained in this study are limited to spatially-uniform storm events with no account made for interstorm periods or within-storm rainfall variability. These assumptions can be readily relaxed in sequence by introducing either observed radar rainfall or a stochastic rainfall model based on regional observations. Nevertheless, the uniform conditions have allowed us to focus on examining the runoff mechanisms leading to multi-scale flood discharges in the basin. The distributed hydrologic model allows the decomposition in space and time of the surface-subsurface processes that control flood response. Insights from the model reveal that storm response magnitude, timing and volume are complex functions of basin properties (including scale), rainfall characteristics and the initial wetness state.

References

Berger, K. P., and D. Entekhabi. 2001. Basin hydrologic response relations to distributed physiographic descriptors and climate. *Journal of Hydrology*. 247(3-4), 169-182.

Betson, R. P. 1964. What is watershed runoff? *Journal of Geophysical Research*. 69(8), 1541-1552.

Beven, K.J., and M. J. Kirkby. 1979. A physically-based variable contributing area model of basin hydrology. *Hydrological Sciences Bulletin*. 24, 43-69.

Bradley, A. A., and J. A. Smith. 1994. The hydrometeorological environment of extreme rainstorms in the Southern Plains of the United States. *Journal of Applied Meteorology*. 33, 1418-1431.

Caroni, E., R. Rosso, and F. Siccardi. 1986. Nonlinearity and time-variance of the hydrologic response of a small mountain stream. In *Scale Problems in Hydrology*, V. K. Gupta et al., eds., D. Reidel Publishing, Dordrecth, 19-37.

Carpenter, T. M., K. P. Georgakakos, and J. A. Sperfslagea. 2001. On the parametric and NEXRAD-radar sensitivities of a distributed hydrologic model suitable for operational use. *Journal of Hydrology*. 253, 169-193.

Eltahir, E. A. B., and P. J.-F. Yeh. 1999. On the asymmetric response of aquifer level to floods and droughts in Illinois. *Water Resources Research*. 35(4), 1199-1217.

Freeze, R. A. 1974. Streamflow generation, *Reviews of Geophysics and Space Physics*. 12(4), 627-647.

Goodrich, D. C., L. J. Lane, R. M. Shillito, S. N. Miller, K. H. Syed, and D. A. Woolhiser. 1997. Linearity of basin response as a function of scale in a semiarid watershed, *Water Resources Research*, 33(7), 2951-2965.

Imes, J. L., and L. F. Emmett. 1994. Geohydrology of the Ozark Plateaus Aquifer System in parts of Missouri, Arkansas, Oklahoma, and Kansas. *USGS Prof. Pap.*, 1414-D.

Ivanov, V. Y., E. R. Vivoni, R. L. Bras, and D. Entekhabi. 2003a. Development of a TIN-based distributed hydrologic model for real-time, continuous forecasting. Submitted to *Water Resources Research.*

Ivanov, V. Y., E. R. Vivoni, R. L. Bras, and D. Entekhabi. 2003b. Preserving high-resolution surface and rainfall data in operational-scale basin hydrology: A fully-distributed, physically-based approach. Submitted to *Journal of Hydrology.*

Johnson, D., M. Smith, V. Koren, and B. Finnerty. 1997. Comparing mean areal precipitation estimates from NEXRAD and rain gauge networks, *Journal of Hydrologic Engineering*. 4, 117-124.

Larsen, J. E., M. Sivapalan, N. A. Coles, and P E. Linnet. 1994. Similarity analysis of runoff generation processes in real-world catchments. *Water Resources Research.* 30(6), 1641-1652.

Levine, J. B., and G. D. Salvucci. 1999. Equilibrium analysis of groundwater-vadose zone interactions and the resulting spatial distribution of hydrologic fluxes across a Canadian prairie. *Water Resources Research.* 35(5), 1369-1383.

Marani, M., E. Eltahir, and A. Rinaldo. 2001. Geomorphic controls on regional base flow. *Water Resources Research.* 37(10), 2619-2630.

Menabde, M., and M. Sivapalan. 2001. Linking space-time variability of river runoff and rainfall fields: a dynamic approach. *Advances in Water Resources*, 24, 1001-1014.

Michaud, J. D., K. K. Hirschboeck, and M. Winchell. 2001. Regional variations in small-basin floods in the United States. *Water Resources Research.* 37(5), 1405-1416.

Ogden, F. L., and P. Y. Julien. 1993. Runoff sensitivity to temporal and spatial rainfall variability at runoff plane and small basin scales. *Water Resources Research.* 29(8), 2589-2597.

O'Loughlin, E. M. 1986. Prediction of surface saturated zones in natural catchments by topographic analysis. *Water Resources Research.* 22(5), 794-804.

Paniconi, C., and E. F. Wood. 1993. A detailed model for simulation of catchment scale subsurface hydrologic processes. *Water Resources Research.* 29(6), 1601-1620.

Risbey, J. S., and D. Entekhabi. 1996. Observed Sacramento basin streamflow response to precipitation and temperature changes and its relevance to climate impact studies. *Journal of Hydrology*. 184, 209-223.

Robinson, J. S., M. Sivapalan, and J. D. Snell. 1995. On the relative roles of hillslope processes, channel routing, and network geomorphology in the hydrologic response of natural catchments. Water Resources Research. 31(2), 3089-3101.

Robinson, J. S., and M. Sivapalan. 1997. Temporal scales and hydrologic regimes: Implications for flood frequency scaling. *Water Resources Research.* 33(12), 2981-2999.

Saghafian, B., and P. Y. Julien. 1995. Time to equilibrium for spatially variable watersheds. *Journal of Hydrology.* 172, 231-245.

Salvucci, G. D., and D. Entekhabi. 1995. Hillslope and climatic controls of hydrological fluxes. *Water Resources Research.* 31, 1725-1739.

Sivapalan, M., K. Beven, and E. F. Wood. 1987. On hydrological similarity 2. A scaled model of storm runoff production. *Water Resources Research.* 23(12), 2266-2278.

Sivapalan, M., E. F. Wood, and K. J. Beven. 1990. On hydrological similarity 3. A dimensionless flood frequency model using a generalized geomorphologic unit hydrograph and partial area runoff generation. *Water Resources Research.* 26(1), 43-58.

Sivapalan, M., C. Jothityangkoon, and M. Menadbe. 2002. Linearity and nonlinearity of basin response as a function of scale: Discussion of alternative definitions. *Water Resources* Research. 38(2), 10.1029/2001WR000482.

Smith, M., Seo, D.-J., Koren, V., Reed, S., Zhang, Z., and F. Moreda. 2003. The Distributed Model Intercomparison Project (DMIP): An overview. Submitted to *Journal of Hydrology.*

Troch, P. A., F. P. de Troch, and W. Brutsaert. 1993a. Effective water table depth to describe initial conditions prior to storm rainfall in humid regions. *Water Resources Research.* 29(2), 427-434.

Troch, P. A., M. Mancini, C. Paniconi, and E. F. Wood. 1993b. Evaluation of a distributed catchment scale water balance model. *Water Resources Research.* 29(6), 1805-1817.

Tucker, G. E., S. T. Lancaster, N. M. Gasparini, R. L. Bras, and S. M. Rybarczyk. 2001a. An object-oriented framework for distributed hydrologic and geomorphologic modeling using triangulated irregular networks. *Computers and Geosciences.* 27(8), 959-973.

VanderKwaak, J. E., and Loague, K. 2001. Hydrologic-response simulations for the R-5 catchment with a comprehensive physics-based model. *Water Resources Research.* 37(4), 999-1013.

Vivoni, E. R., V. Y. Ivanov, R. L. Bras, and D. Entekhabi. 2002. Topography, triangular irregular networks and hydrological similarity. *Journal of Hydrologic Engineering.* (Accepted).

Walker, J. P., and G.R. Willgoose. 1999. On the effect of digital model accuracy on hydrology and geomorphology. *Water Resources Research.* 35(7), 2259-2268.

Wang, C. T., V. K. Gupta, and E. Waymire. 1981. A geomorphologic synthesis of nonlinearity in surface runoff. *Water Resources Research.* 17(3), 545-554.

Western, A., and R. Grayson. 2000. Soil moisture and runoff processes at Tarrawarra. In *Spatial Patterns in Catchment Hydrology: Observations and Modelling.* R. Grayson and G. Blöschl, ed., Cambridge University Press, Cambridge, UK, 209-246.

Winchell, M., H. V. Gupta, and S. Sorooshian. 1998. On the simulation of infiltration- and saturation-excess runoff using radar-based rainfall estimates: Effects of algorithm uncertainty and pixel aggregation. *Water Resources Research.* 34(10), 2655-2670.

Zecharias, Y. B., and W. Brutsaert. 1988. Recession characteristics of groundwater outflow from mountainous watersheds. *Water Resources Research.* 24(10), 1651-1658.

Conclusions and Future Directions

This thesis has presented the development and application of a new distributed hydrologic model based on a triangulated irregular network representation of catchment terrain. It has focused on the methods for constructing watershed topographic models, an evaluation of the rainfall-flood forecasting capabilities and understanding the variability of surface-subsurface response with respect to changes in forcing and initial conditions. The results confirm the capability of the model to account explicitly for spatial variations in watershed and hydrometeorological conditions. As a tool for hydrologic forecasting and experimentation, the physically-based distributed model provides new opportunities for studying the linkages between internal basin processes and the observed hydrograph.

The formulation and application of triangulated irregular network models of basin response has not received widespread attention in the hydrologic community. As a result, much research is required to develop appropriate methods for implementing, verifying and testing the sensitivity of these models. This has led much of the research conducted in this thesis to be directed towards developing methods for terrain representation and testing its impact on hydrologic predictions. In this respect, this thesis makes several important contributions to the state-of-the-art, including:

(a) Formalizing methods for integrating topographic, hydrographic and landscape descriptors into a computational TIN representation of a watershed.

(b) Developing a new approach for generating multiple resolution meshes that utilize *a priori* process knowledge to constrain the triangulation procedure.

(c) Testing the variability of hydrologic response with respect to variations in terrain resolution in the context of triangulated irregular network models.

The distributed hydrologic model is an exceptional virtual tool for hydrologic experimentation and inquiry with broad applicability to operational and theoretical problems in hydrologic science and engineering. From theoretical studies exploring the connection between the storm hydrograph and catchment size to the practical problem of improving flood forecast lead time, the hydrologic model is both a medium for testing hypothesis and an embodiment of hydrologic knowledge. This thesis has explored two such aspects through application studies designed to address scientific inquiries in watershed hydrometeorology. In so doing, several significant contributions to hydrologic science are presented in this thesis, including:

(a) Identifying the flood forecast enhancements due to radar rainfall nowcasting as a function of lead time, catchment scale and spatial rainfall variability.

(b) Relating the variability in the catchment hydrograph to underlying surface and subsurface mechanisms to identify sources of runoff nonlinearity and scale-dependency.

These topics are the heart of catchment hydrology, addressing the understanding of a watershed as an interconnected system of coupled processes and the limits of predictability that currently exist in our capacity to forecast hydrologic events. Much work has been done in the past in the hydrologic community with regard to these science questions, and undoubtedly, much research is still ahead. Nevertheless, this work shows that physically-based, distributed modeling can be used for addressing these topics.

Several areas for further investigation with the distributed hydrologic model have been identified throughout the course of this research. In general, there are research opportunities related to extending the space-time application of the model, in verifying the spatial-temporal dynamics produced by the model, in expanding the hydrologic

processes simulated over complex terrain, and in coupling the model to remote sensing and field observations. In addition, a significant amount of effort should be dedicated to further understanding the model dynamics and the relation between hydrologic states and fluxes and the variability in catchment characteristics. The following is a brief list of potential opportunities and questions that should be addressed in the future.

(1) *How can the hydrological similarity method be used to construct macroscale hydrologic models that capture spatial variability in land-surface properties? What level of coupling can be achieved with atmospheric models?*

The method for constructing TINs using the wetness index was shown to be a valuable representation of the Mississippi River basin with a reasonable number of computational nodes. A macroscale application of the tRIBS model would provide an alternative land-surface scheme that explicitly contains a groundwater component and the lateral redistribution of moisture due to topography. This, in turn, can provide a more realistic surface hydrologic boundary condition for various atmospheric models used for weather forecasting and climate studies.

(2) *How can the distributed hydrologic model be used to understand the impact of long-term changes in climate, land-use and disturbances on a basin storm response?*

The model captures the short-term response to rainfall in the form of storm hydrographs and spatial variability in hydrologic processes under a specific set of climate and land-use conditions. Long-term simulations using the tRIBS model with historical observations or stochastically-generated climate scenarios can allow for understanding the propagation of atmospheric to hydrologic state anomalies, say in the groundwater system. Long-term simulations with a variable vegetation or land-use cover, say from the

effects of urbanization or agricultural practices, can lead to predictions of the impacts on the hydrologic response in the basin. Similarly, the effects of disturbances such as fire, landsliding or drought can be assessed in a spatially-distributed framework.

(3) *How does the model perform with respect to field observations of spatially-distributed hydrologic state? Can the spatial patterns in hydrology be used during model calibration and verification?*

The model has been shown to accurately capture the storm and interstorm basin discharge response at multiple gauging stations. Nevertheless, few observations of the internal hydrologic fluxes and states are currently available for calibrating and verifying many of the hydrologic processes including in the model. A model application to a well-instrumented research watershed would improve our capability to test process dynamics and explore the modeled versus observed relations between catchment characteristics and hydrologic response. The selected watershed should have long-term point measurements of rainfall, runoff, groundwater table position, surface soil moisture and meteorological conditions, and possibly remote sensing data from satellites or field campaigns.

(4) *How can the performance of the distributed hydrologic model be improved via the use of field and remote sensing observations? Can a data assimilation scheme be used to update distributed model states based on these observations?*

The physically-based distributed model has been used a deterministic tool for studying basin response without accounting for the uncertainties inherent in the model and in the observations of the basin hydrograph. More robust data assimilations methods currently exist that allow for the ingestion of punctual or spatially-variable observations from in-situ or remote sensing instruments into models. For example, a data assimilation

scheme can couple the distributed predictions of soil moisture obtained through the physical model with the observations from a satellite sensor. This would allow for more realistic model output constrained by the observations as well as the dynamic propagation of remote sensing data to other parts of the basin hydrologic system.

(5) *How does the model perform under different climatic settings where the hydrologic processes of interest may vary? Can we further generalize the model structure to include additional processes?*

The model has been applied to humid watersheds where the surface and groundwater coupling has a predominant control on hydrologic response. In order to apply the model to other climate regions (*e.g.*, semi-arid or mountainous), further developments are required to capture the important effects of snow, channel transmission losses, re-infiltration, vegetation dynamics, lake and reservoirs storage, among others. Appropriate couplings to the existing saturate-unsaturated dynamics and surface energy and water balances will be required. Nevertheless, the inclusion of additional hydrologic processes will extend the usefulness of the distributed model and add to the potential list of observed quantities used for model calibration, verification and data assimilation.

The prospects for continuing the investigation of basin hydrologic response with the distributed model as a tool for scientific inquiry are abundant. Increasing the linkages between field observations and model predictions is essential to refine current methods, explore new scientific questions and advance the capabilities of the forecasting tool. In time, numerical models that accurately represent our current understanding of hydrologic processes will allow greater predictive power and better insight into the complex relation between variable rainfall fields and catchment response.